Multiresolution Coarse–Grained Modeling of the Microstructure and Mechanical Properties of Polyurea Elastomer

by

Minghao Liu

A Dissertation Presented in Partial Fulfillment
of the Requirements for the Degree
Doctor of Philosophy

Approved October 2020 by the
Graduate Supervisory Committee:

Jay Oswald, Chair
Christopher Muhich
Hanqing Jiang
Pedro Peralta
Yang Jiao

ARIZONA STATE UNIVERSITY

December 2020

ABSTRACT

Polyurea is a highly versatile material used in coatings and armor systems to protect against extreme conditions such as ballistic impact, cavitation erosion, and blast loading. However, the relationships between microstructurally–dependent deformation mechanisms and the mechanical properties of polyurea are not yet fully understood, especially under extreme conditions. In this work, multi–scale coarse–grained models are developed to probe molecular dynamics across the wide range of time and length scales that these fundamental deformation mechanisms operate. In the first of these models, a high–resolution coarse–grained model of polyurea is developed, where similar to united–atom models, hydrogen atoms are modeled implicitly. This model was trained using a modified iterative Boltzmann inversion method that dramatically reduces the number of iterations required. Coarse–grained simulations using this model demonstrate that multiblock systems evolve to form a more interconnected hard phase, compared to the more interrupted hard phase composed of distinct ribbon–shaped domains found in diblock systems. Next, a reactive coarse–grained model is developed to simulate the influence of the difference in time scales for step–growth polymerization and phase segregation in polyurea. Analysis of the simulated cured polyurea systems reveals that more rapid reaction rates produce a smaller diameter ligaments in the gyroidal hard phase as well as increased covalent bonding connecting the hard domain ligaments as evidenced by a larger fraction of bridging segments and larger mean radius of gyration of the copolymer chains. The effect that these processing–induced structural variations have on the mechanical properties of the polymer was tested by simulating uniaxial compression, which revealed that the higher degree of hard domain connectivity leads to a 20% increase in the flow stress. A hierarchical multiresolution framework is proposed to fully link coarse–grained molecular simulations across a

broader range of time scales, in which a family of coarse–grained models are developed. The models are connected using an incremental reverse–mapping scheme allowing for long time scale dynamics simulated at a highly coarsened resolution to be passed all the way to an atomistic representation.

ACKNOWLEDGMENTS

Firstly, I would like to appreciate the help that my advisor, Dr. Jay Oswald, provided to me during my Ph.D. study. His patience and hard–working encouraged me to pursue my doctorate study over the last four years. Whenever I felt lost and confused, the guidance from him always leads me to the details of programming, experimental design, etc. It is my honor to be his student and I believe his critical thinking and enthusiasm in research will definitely benefit the future of my career.

Then, I would like to express my appreciation to my dissertation committee members, Dr. Christopher Muhich, Dr. Hanqing Jiang, Dr. Pedro Peralta, and Dr. Yang Jiao, for attending my dissertation defense, providing advice for my work from various background and discussing the future direction of this field. Also, many thanks to my colleagues in Dr. Oswald's lab, Dr. Yiyang Li, Jianlan Ye, Jing Hu, Pawan Veeresh, and Omid Eghlidos, for their help and discussion.

Finally, thanks to my family. Your love, support, and encouragement are the strength making me where I am right now. Thank you for always being there.

TABLE OF CONTENTS

LIST OF TABLES

Table Page

LIST OF FIGURES

Figure Page

Chapter 1

INTRODUCTION

1.1 Introduction to Polyurea

Polymers are macromolecules comprised of repeating units (or monomers) which are connected in linearly, branched, or networked configurations during polymerization [1]. The macroscopic properties of polymers arise from the complex and collective many–body dynamics governed by inter– and intra–chain interactions. The mechanical behavior of polymers can vary from a hard glass to a soft elastomeric rubber to a viscous liquid, depending on the temperature and deformation mode [2]. The critical temperatures at which the mechanical behaviors of polymer exhibit these transitions are referred as the glass transition temperature (T_g) and the melting temperature (T_m). Glass transition is a reversible process in which an amorphous material transitions from a hard and glassy state to a viscous rubber [3]. Polymers that contain only a single type of repeat unit are known as homopolymers, while polymers containing two or more types of repeat units are known as copolymers [4].

Polyurea is a block copolymer produced from the stepwise polymerization of an isocyanate component and a diamine resin to form long molecular chains composed of alternating segments joined by urea linkages. The different interactions among these alternating segments and linkages, e.g., hydrogen bonding between urea groups, lead to microphase separation in microstructure forming a binary nanostructure with two distinct phases. A hard, glassy domain consists of molecular segments containing aromatic and urea groups, hereafter referred to as hard segments, and is characterized

by higher modulus and glass transition temperature. The glassy phase is embedded within a soft, rubbery phase comprised of disordered aliphatic segments, hereafter referred to as soft segments, that exhibits low stiffness and a lower T_g. The hard domains act as physical cross links to the molecular network, engendering polyurea with excellent mechanical properties, such as excellent strength, toughness, and highly dissipative and resilient large strain behavior [5–7], making it attractive for a wide range of applications, such as as protective coatings [8], foam padding [9], and as a component in composite armor systems [10].

The microstructure as well as mechanical properties of polyurea are highly dependent on many factors such as the molecular weight of the oligomeric diamines used in synthesis [11], thermal history [12], composition of soft and hard segments [13, 14] and the chemistry of reactant in material synthesis [15]. According to atomic force microscopy (AFM) as shown by Castagna et al. [11], the hard domains in polyurea network synthesized from Versalink® P–1000 oligomeric diamines, i.e., PTMO with molecular weight 1000 g/mol, (PU1000) form a continuous hard structure. This percolated miscrostructure forms long–range connectivity among hard segments [16]. However, in the polyurea reacted with PTMO molecular weight of 650 g/mol (PU650), the continuity of hard domain structure is disrupted, while the phase–segregated morphology with ribbon–like hard domains was still remained. Additionally, the degree of microphase separation between hard and soft segments decreases with shorter soft–segment length, until in PU250 that no detectable microphase separation was observed in AFM images. To further study the phase segregation in polyurea, Castagna et al. [11] employed small–angle X–ray scattering (SAXS) to study the degree of segmental segregation in terms of molecular weight of PTMO. This method is based on comparison of the quantitative experimental scattering variance with the hypo-

thetical electron density variance of completely demixed hard and soft segments with sharp interfaces [17, 18]. The mean inter–domain spacing is about 7 nm for PU1000 and PU650 calculated from the SAXS absolute intensity versus scattering vector (q). However, the microstructural features of polyurea are temperature–dependent [12]. According to a series of temperature–dependent experiments, even though the phase–segregated morphology was preserved after annealing at elevated temperatures, the inter–domain spacing showed a significant change at high temperature suggesting a temperature–dependent microstructural reorganization. It can be observed that the inter–domain spacing decreases with higher annealing temperature which can be observed in the SAXS intensity for polyurea after different annealing temperatures. And this is consistent with the AFM tapping mode phase image shown in [12] which demonstrated that the hard domains are coarsened after annealing from high temperature. The effect of geometry within isocyanates on the morphology of polyurea was investigated by polyurea synthesized by 2,6–TDI, 2,4–TDI and MDI isocyanates and P1000 amines [15, 19]. All of the polyureas represent segregated hard domains with mean thickness of approximately 10 nm, while symmetric isocyanates 2,6–TDI strengthen the microphase separation by bidentate hydrogen bonding leading to apparent long–range connectivity in hard domains due to more efficient packing between hard segments [20].

The mechanical behaviors, especially viscoelasticity and strength, of segmented block copolymer such as polyurea and polyurethane in terms of deformation are also temperature–, pressure– and rate–(or frequency–)dependent [21–25]. Since the application of polyurea is usually under extreme conditions with high pressure and strain rate, wave–based methods are typical experimental measurement to investigate the stress behaviors under these situations. Yi et al. [23] demonstrated that the

mechanical response of polyurea transforms from rubbery–regime behavior at low strain rate (10^{-3}–10^{0} s^{-1}) to either leathery or glassy–regime at high strain rate ($\sim 10^{3}$ s^{-1}) by uniaxial compression testing and split Hopkinson pressure bar (SHPB). And they extended the SHPB testing to strain rate up to $\sim 10^{4}$ s^{-1} and reported the strain–stress relationship under uniaxial compression, the glass transition from which agrees well with Dynamic Mechanical Analysis (DMA) result [22]. Roland et al. [21] carried out an improved drop weight test instrument to test the strain–stress behavior under intermediate strain rate to fill the gap between quasi–static test and SHPB experiment. After that, they measured the local segmental relaxation times of polyurea in terms of temperature and pressure by dielectric spectroscopy, the result from which suggests that the relaxation times of soft segments can be represented by temperature times the power of specific volume [24]. Pathak et al. carried out strain–stress measurements accompanied with SAXS on polyurea samples stretched over strain rates from 0.15 to 830 s^{-1} to study the structural evolution of polyurea during deformation. According to the SAXS measurements after large deformation, slow–rate deformation breaks the morphology and causes permanent residual strain, whereas the miscrostructure completely recovers high strain rate [26]. By performing tensile deformation with strain rate of 0.005 s^{-1}, Rinaldi et al. also observed the breakdown of microphase structure [27] when strain is larger than 0.4, while reversible structural change appears with smaller strain. Impact–based method is also a typical way to investigate the strength of polyurea under high pressure and strain rate [7, 28–33]. The shear stress of polyurea is highly sensitive to pressure as shown by pressure–shear plate experiment [31, 32]. Pressure–shear plate impact (PSPI) is a typical experimental technique to study shear resistance of material under high pressure. Jiao and Clifton enhanced PSPI with symmetric configuration and

directly measured the shear resistance of 500 MPa under pressure of 9 GPa [31]. After that, they extended the configuration to pressure of 18 GPa obtaining 1 GPa shear strength and developed a quasilinear viscoelastic constitutive model for polyurea calibrated by experimental results [32].

1.2 Systematic Coarse–Grained Model

It is a significant challenge to characterize the properties of elastomers under the extreme conditions, e.g., high pressure and fast deformation, characteristic of these aforementioned applications. Furthermore, to develop optimized materials for specific operating conditions, e.g., protective coatings are typically subjected to repeated loads, whereas armor is typically subjected to a single extreme loading event, it is especially important to develop an understanding of how chemical composition and processing affects the microstructure, and ultimately, the properties of elastomers. In extreme conditions, particularly under high strain rate loading, molecular dynamics (MD) simulations can provide direct insight to how deformation mechanisms are influenced by the material composition and structure, e.g., molecular weight (M_w), degree of hydrogen bonding, and microphase separation, and ultimately, how these factors influence the overall material response. However, MD simulations are restricted by their high computational cost to relatively short time and small length scales, which severely limits their applicability in modeling how the molecular structure evolves during slow processes, such as material processing and curing. The time scales accessible in atomistic modeling is typically limited to a few hundred nanoseconds, whereas curing processes occur over hours or even days. To model curing and other slow rate processes, coarse-graining approaches are required [34, 35], in which groups of

atoms are lumped together into super–atoms, allowing molecular simulations to probe much longer time scales while still retaining key molecular details and mechanisms.

Over the past decade, several researchers have investigated relationships linking microstructure and mechanical properties in polyurea and similar elastomers using coarse–grained simulations. Using a simple bead–spring model, Arman et al. [36] demonstrated that in polyurea–like elastomers, energy dissipation under shock loading increases with the degree of hard domain connectivity. Cui et al. [37, 38] revealed the importance of intermolecular attraction between hard segments to microphase separation through manipulating LJ energy parameters. Agrawal et al. [39, 40] utilized systematic coarse–graining to predict the stress–relaxation in polyurea as a function of the molecular weight. Liu and Oswald [41] studied the soft and hard domain structure of polyurea using a systematically coarse–grained united–atom model, including quantifying the extent of hydrogen bonding and the topology of the soft segment connectivity. These chain conformations have been shown to significantly affect the deformation and plasticity of phase–segregated copolymer [42]. For example, the relative fraction of soft segment loops and bridges, i.e., aliphatic segments that are covalently bonded to the same or different hard domains, respectively, was demonstrated by Zhu et al. [43] to play an important role in strain hardening during deformation of thermoplastic polyurethanes. However, due the relatively small size of molecular systems and simplification of hard domains into stacking lamella, the effect of molecular conformation was hardly considered. Polymer coils with larger spatial dimension linking across more than two hard domains are supposed to have different bridge entanglements with the one of several single soft segments. Therefore, a more powerful coarse–grained model is needed to incorporate the complicated hard–domain structures and molecular spatial effect on mechanical properties on polyurea.

Coarse–grained models at different resolutions are needed to resolve the vastly different length and time scales associated with elastomeric copolymer phase segregation [36, 37, 39, 40], macroscopic properties [44, 45], deformation modes [43], and failure mechanisms [6]. Since atomistic simulations are too computationally costly to probe the long timescales associated with polymer relaxation phenomena [46, 47], molecular simulations exploring microphase morphology and mechanical properties in polyurea have mostly utilized coarse–grained models in which much of the atomistic detail is absent, e.g., within the glassy hard segments of polyurea, one or more aromatic rings are replaced by a single super–atom that interacts with other super–atoms through spherically symmetric potentials [36, 37, 39, 40]. At this coarse level of detail, the local structure within the segregated domains is crudely represented. In polyurea, attractions between chemical groups, e.g., hydrogen bonding and possibly π–π stacking of aromatic rings, leads to a phase segregation into a high–T_g, hard domain dispersed within a low–T_g, soft domain. Recent work by Li et al. [48] has demonstrated that long range connectivity of the hard domains and the degree to which the network of hydrogen bonds within the hard domains is tightly ordered [49] are correlated to stiffness, strength, and high energy dissipation during large deformation. Wu et al. [50] systematically investigated how interconnected hydrogen bond networks can slow dynamics at the molecular level to enhance dynamic stiffening, and thus energy dissipation, in polyurethanes under extreme strain rates caused by micro-ballistic impacts. Simulations of polyurethanes reported by Zhu et al. [43] have revealed how molecular level mechanisms are dependent on the topology of chains at the interface between soft and hard domains and are responsible for yield, toughening, and the Mullins effect. However, the polyurethanes considered in his work have crystalline hard domains, allowing for realistic atomistic configurations to be created by the interphase Monte

Carlo method. Therefore, in order to consider the effects of molecular structure on material properties more generally, e.g., for elastomers with a non–crystalline glassy phase, there is a need for coarse–grained models that can accelerate modeling of phase morphology and represent key interactions, such as hydrogen bonding, with sufficient fidelity.

The iterative Boltzmann inversion (IBI) method is a structure–matching approach that develops coarse–grained potentials between super–atoms to reproduce target structural distribution functions sampled from atomistic simulations [51, 52]. In recent years, considerable progress has been made in developing IBI approaches for modeling polymeric materials at different levels of resolution. For phase–segregating polymers, e.g., block copolymers and immiscible polymer blends, the coarse–grained potentials are strongly interdependent [53]. Sun and Faller [54] have shown that interactions of CG sites show different sensitivities in terms of interactive distances and types within phase–segregated systems, which means the iterative method is more difficult to get global optimal solutions compared to the iteration in homopolymeric systems. Errors in sampling the structural distributions can introduce noise in the potential training, leading to spurious oscillations in the resulting coarse–grained potentials. Sampling noise can be mitigated by fitting the optimized potentials to functional forms [55, 56], however, as the number of different coarse–grained sites and number of types of interactions increases, identifying the different functional forms can become a significant challenge. Furthermore, for copolymers such as polyurea, sampling errors may arise due to differences in how the target or coarse–grained systems segregate into different phases. In particular, due to the slow dynamics of the fully atomistic target systems, the structural distributions are likely to be sampled from metastable, non-equilibrium states.

Chapter 2

COARSE–GRAINED MOLECULAR MODELING OF THE MICROPHASE STRUCTURE OF POLYUREA ELASTOMER

2.1 Introduction

Elastomers, such as polyureas and polyurethanes, are a highly versatile class of copolymers used in coatings, armors, and composites for their high toughness, low density, and capability to absorb and dissipate energy from ballistic impacts and blast loading [5, 10]. The versatility of these elastomers arises from the ability to alter their microstructure by modifying the chemical structure [19, 20, 57], concentration [13], and molecular weight [11] of their constituent units, and by changing processing conditions [12, 14, 58]. With this enormous design space from which elastomers can be tailored for improved performance, computational tools, such as molecular dynamics simulations, are attractive in accelerating the materials design process. However, the wide range of length and time scales over which the molecular mechanisms that govern material structure and properties operate poses a formidable challenge for molecular-scale simulation [34]. As a result, there has been a significant effort to develop coarse–grained (CG) models, in which groups of atoms are lumped into single interaction sites, which are less computationally demanding due to the reduced number of degrees of freedom, simplified interaction potentials, and increased stable simulation time step [34, 35].

In this section, we present a coarse–grained model of polyurea at a resolution similar to united atom models, where the detailed structure of the hard phase can be resolved

and thus the influence of fine scale features, e.g., hydrogen bonds networks and ring stacking configurations, on mechanical properties can be investigated. To address the previously described challenges, we introduce new techniques extending the robustness and applicability of the IBI method for complex polymer systems, i.e., systems featuring phase segregation as well as requiring a large number of chemically distinct, coarse–grained sites. In particular, we propose a new adaptive scaling technique that accounts for distance–dependent sensitivity of the radial density functions (RDFs) to the pairwise potential functions and compare the performance of the traditional IBI method in optimizing coarse–grained potentials with our new approach. With our resulting calibrated model, we performed equilibrium molecular dynamics simulations on two large–scale polyurea systems featuring diblock and multi-block molecular chains and describe the resulting phase segregated morphologies, hard domain structure, and connectivity of soft chain segments across hard domains. Ultimately, by combining coarse–grained models at multiple resolutions, we envision that simulations can span the wide range of relevant time and spatial scales needed to resolve key molecular mechanisms and thus reveal the complex relationships between elastomer chemistry, processing, and mechanical behavior.

2.2 Methodology

2.2.1 Model Polyurea System

The coarse–grained model was developed to match local structural distributions sampled from atomistic simulations of short, oligomeric polyurea chains. This model polyurea system is an idealization of a common commercial variant of polyurea that is

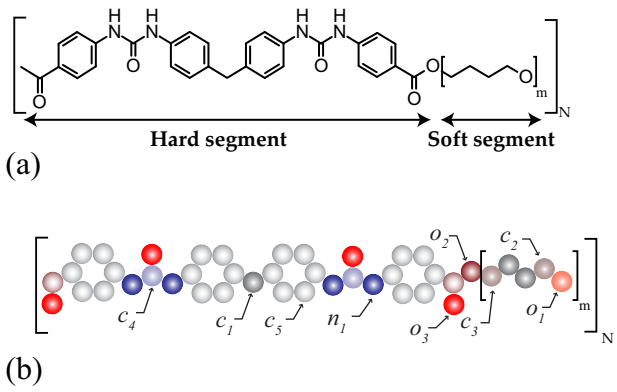

Figure 2.1: Molecular models of polyurea: (a) structural formula, (b) coarse–grained model.

synthesized from reaction of diphenylmethane diisocyanate and a poly(tetramethylene oxide) diaminobenzoate. The resulting chemical structure, shown in Figure 2.1a, is a copolymer made up of alternating hard segments, each containing four aromatic moieties and two urea linkages, and soft segments composed of poly(tetramethylene oxide). The chemical structure of the polyurea chains is expressed as $(\mathrm{HS}_m)_N$, where H is a hard segment, S_m represents m repeated tetramethylene oxide units making up a soft segment, and N denotes the number of times the HS_m block is repeated. In this work, $m = 14$ is chosen to be consistent with polyureas synthesized with Versalink® P–1000 oligomeric diamine.

To sample the target local structural distributions, eighteen atomistic systems, each containing twenty short oligomeric polyurea chains ($\mathrm{S}_7\mathrm{HS}_7$), were generated by a random–walk process within a periodic simulation domain. Here, the hard segment is placed in the center of the oligomeric chains to avoid unwanted end effects. Using the procedure developed by Agrawal et al. [39], the atomistic systems were first annealed above the melting temperature of the hard domains [26] in the isothermal–isobaric (NPT) ensemble over a duration of 8 ns with $T = 500$ K and $p = 1$ atm. Following annealing, the temperature was ramped down to $T = 300$ K over a duration of

	pair	angle	bond	dihedral	improper
range	$1 - 10$ Å	$0 - 180°$	$0 - 3$ Å	$-180° - 180°$	$-90° - 90°$
bin size	0.05 Å	$1°$	0.01 Å	$1°$	$1°$
count	45	17	12	19	5

Table 2.1: Implementation details of sampling structural distributions, where bin size is the interval of the sampling histogram, range is the min–max value of sampling, and count is the total number of corresponding interaction types in the coarse–grained model.

8 ns, and then the systems were further equilibrated for 16 ns at $T = 300$ K and $p = 1$ atm, at which point the average density of the eighteen configurations was 1.073 g/cm^3, with a standard deviation of 0.003 g/cm^3. Following equilibration, a 1 ns duration canonical (NVT) ensemble simulation was performed to sample the atomistic trajectories. The atomistic coordinates are mapped to coarse–grained sites, from which radial density, bond length, bond angle, dihedral angle, and improper angle distributions are computed. In the RDFs, the first– and second–bonded neighbors of each super–atom are excluded. More details of how the various structural distributions were computed are given in Table 2.1.

All molecular dynamics simulations were carried out using the large–scale atomic/molecular massively parallel simulator (LAMMPS) package [59]. In the atomistic simulations, bonded and non–bonded interactions are modeled using the COMPASS (Condensed–phase Optimized Molecular Potentials for Atomistic Simulation Studies) force field [60, 61], which has been used to model the microstructure and mechanical properties of polyurea [62]. Long–range Coulombic interactions are computed using the particle–particle/particle–mesh (PPPM) method in the LAMMPS

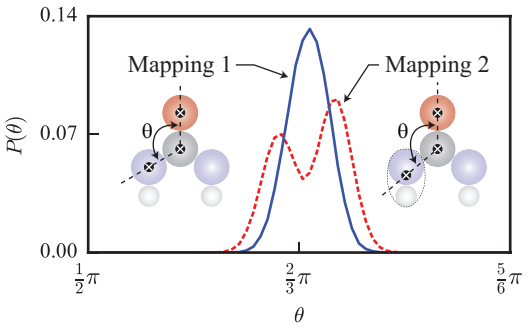

Figure 2.2: Angle distribution of the $n_1 - c_4 - o_3$ angle type computed from different mapping schemes.

kspace package. The cutoff distance for short range Coulombic and pairwise interactions was set at 9.5 Å and the time step for integrating the atomistic trajectories was 1 fs.

Similar to the conventional united–atom model, we employ a coarse–grained mapping scheme, in which all heavy atoms, i.e., excluding hydrogen atoms, are represented by interaction sites from which the total potential energy of the system is defined. We considered two mapping schemes: one in which each interaction site is coincident with a heavy atom (mapping scheme 1) and one where the interaction sites are located at the center of mass of the heavy atoms and their bonded hydrogen atoms (mapping scheme 2). To inform our selection between the two mapping schemes, we compared the distributions of bond angles computed from both schemes. As shown in Figure 2.2, using the center of mass definition results in doubly peaked bond angle distributions, which is usually accompanied by correlations between the bond length and bond angle distributions. It is necessary that the distributions of bond lengths and bond angles are independent so that the potential can be decomposed into a sum

of bond and angle energies [56, 63], and so we selected mapping scheme 1, using the locations of only the heavy atoms to sample the coordinates of the super–atoms.

Although our idealized polyurea model is composed of only four different elements, it is modeled using eleven distinct atom types. The different atom types reflect the chemical functional groups to which atoms belong, e.g., oxygen atoms within ester, ether, and carbonyl groups are assigned as three different types. Figure 2.3 shows the RDFs computed from all combinations of various oxygen atom types indicating that the distributions are generally quite different from each other, and thus in the CG model, we assign distinct CG super–atom types based on the corresponding atom type in the atomistic model. Furthermore, the Coulombic interactions arising from partial charges are absent in the coarse–grained model, but instead are represented implicitly as part of the coarse–grained pair potentials. Thus, distinct CG super–atom types are also needed to represent the variation of partial charges across different chemical groups. As a result, the CG model of polyurea utilizes nine separate super–atom types, each described in Table 3.1. The mapping of the CG types within the polyurea chain is given in Figure 2.1b.

Coarse–grained systems were constructed to sample the structural distributions by coarse–graining the eighteen atomistic systems so that the super–atom coordinates of the CG systems initially coincide with their corresponding atoms in the atomistic systems. The systems were then equilibrated over a span of 3 ps at constant temperature, $T = 300$ K, in the NVT ensemble, after which point the distribution functions no longer significantly evolve in time. Following equilibration, the NVT simulations are continued for 20 ps to sample the radial, bond length, bond angle, and torsion angle distributions. Without the lighter hydrogen atoms, the simulation time step for

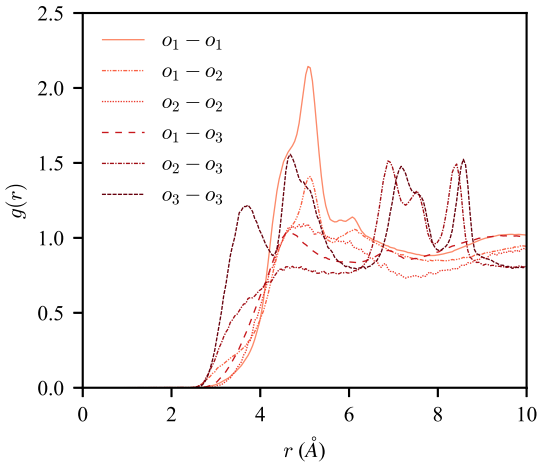

Figure 2.3: Target RDFs of the various oxygen atom types sampled from atomistic simulations of the model polyurea system.

Super–atom type	**Description**	**Equiv. COMPASS type**
c_1	carbon, sp3, generic	c4
c_2	carbon, sp3, bond to oxygen	c4o
c_3	carbon, sp2, carbonyl, one polar subst	c3'
c_4	carbon, sp2, carbonyl, two polar subst	c3"
c_5	carbon, sp2, aromatic	c3a
o_1	oxygen, sp3, in ethers	o2e
o_2	oxygen, sp3, in esters	o2s
o_3	oxygen, sp2, in carbonyl	o1=
n_1	nitrogen, sp3, in amides with H	n3mh

Table 2.2: Definition of super-atom types and corresponding descriptions in terms of COMPASS force field.

the CG systems can be increased to 2 fs with negligible effect on stability and energy drift.

2.2.2 Iterative Boltzmann Inversion Procedure

To start the IBI optimization of the CG potentials, initial estimates of the potential energy functions for the nonbonded pair distances r bond lengths l, bond angles θ, dihedral angles ϕ, and improper angles χ are based on the potentials of mean force, which is computed from the Boltzmann inversions of the corresponding distribution functions:

$$V_0(l) = -k_B T \ln\left(\frac{P^*(l)}{l^2}\right) \tag{2.1}$$

$$V_0(\theta) = -k_B T \ln\left(\frac{P^*(\theta)}{\sin(\theta)}\right) \tag{2.2}$$

$$V_0(\phi) = -k_B T \ln\left(P^*(\phi)\right) \tag{2.3}$$

$$V_0(\chi) = -k_B T \ln\left(P^*(\chi)\right) \tag{2.4}$$

$$V_0(r) = -k_B T \ln\left(g^*(r)\right), \tag{2.5}$$

where k_B is the Boltzmann constant, T is the simulation temperature, $P^*(\square)$ is the target probability distribution functions of coarse–grained variables $\square \in \{l, \theta, r, \phi, \chi\}$, and $g^*(r)$ are the target RDFs. The bond length and bond angle distributions are normalized by the Jacobian of the transformation between spherical and Cartesian coordinates. The number of different potentials for our polyurea model is quite large, from the 9 different atom types, we compute 45 different pair potentials, 12 bond potentials, 17 angle potentials, 19 dihedral potentials, and 5 improper potentials.

Using initial potentials defined above, structural distributions are sampled from coarse–simulations from a subset of the available pool of coarse–grained systems. In

this work, three of the eighteen available systems were sampled in the initial iteration. The effective potentials are then corrected to better match the target distributions in an iterative fashion using the iterative Boltzmann inversion update:

$$V_{i+1}(\square) = V_i(\square) + \alpha k_B T \ln\left(\frac{P_i(\square)}{P^*(\square)}\right), \tag{2.6}$$

where $P_i(\square)$ are the distributions, including RDFs, sampled from coarse–grained MD simulations using potentials $V_i(\square)$ at iteration i. Since the resulting distribution functions can be highly sensitive to small changes in the potentials, the update is typically scaled by a factor $\alpha < 1$ used to dampen and stabilize the iterative procedure. As the sampled coarse–grained distributions approach the target distributions, the second term on the right hand side of Eq. (4.1) vanishes, resulting in a stationary point in the iteration. More details of the IBI procedure can be found in Algorithm S1.

The target bond length, bond angle, and improper angle distributions are well–represented as normal distributions, and thus their interaction energies can be modeled as quadratic potentials:

$$V(l) = K_b(l - l_0)^2, \tag{2.7}$$

$$V(\theta) = K_a(\theta - \theta_0)^2, \tag{2.8}$$

$$V(\chi) = K_i(\chi - \chi_0)^2, \tag{2.9}$$

where l_0, θ_0, and χ_0 are the equilibrium bond length, bond angle, and improper angle, respectively, and K_b, K_a, and K_i are the corresponding stiffness coefficients. We note that the typical factor of 1/2 is omitted from the potential forms following the convention of the corresponding bond, angle, and dihedral styles in LAMMPS. The optimized potentials computed by Eq. (4.1) are fitted to Eqs. (3.2-2.9) to obtain the equilibrium locations and stiffness coefficients of each harmonic potential. Further details on the

Algorithm S1 Iterative Boltzmann inversion

procedure IBI($V_0(\square)$, $P_0(\square)$, $P^*(\square)$)
  $i = 0$
  while $e_i >$ critical value **do**
    Update harmonic potential:

$$V_{i+1}(l) \leftarrow V_i(l) + \Delta V(l)$$

    Update harmonic potential:

$$V_{i+1}(\theta) \leftarrow V_i(\theta) + \Delta V(\theta)$$

    Update tabulated potential:

$$V_{i+1}(r) \leftarrow V_i(r) + \Delta V(r)$$

    Update tabulated potential:

$$V_{i+1}(\phi) \leftarrow V_i(\phi) + \Delta V(\phi)$$

    Update harmonic potential:

$$V_{i+1}(\chi) \leftarrow V_i(\chi) + \Delta V(\chi)$$

    Pressure correction $V_{i+1}(r) = +\Delta V_{pc}$
    Run LAMMPS with $V_{i+1}(\square)$
    Compute $P_{i+1}(\square)$
    Compute $e_{i+1} = ||P_{i+1}(\square) - P^*(\square)||_2$
    $i \leftarrow i + 1$
  end while
end procedure

Algorithm S2 Update harmonic potential

1: **procedure** HARMONIC(V^i, P^*, P^i)
2: Compute $\Delta V_k = k_B T \ln\left(\frac{P_k^i}{P_k^*}\right)$
3: $V_k^{i+1} \leftarrow V_k^i + \Delta V_k$
4: x_0, $K \leftarrow \min_{x_0,K} \sum_k \left[V_k^{i+1} - K(x_k - x_0)^2\right]^2 dx$
5: **return** x_0 and K
6: **end procedure**

procedures to update the harmonic potentials (bond, angle, and improper) are given in Algorithm S2.

Tabulated functions are used to represent the more general forms of the pair distance and dihedral potential energy functions. In the CG simulations, pairwise interactions are truncated at a cutoff distance of 10 Å and shifted so that the pairwise energy is zero at the cutoff distance. Since the pairwise and dihedral energies are computed in a tabulated form, smoothing is needed to minimize noise arising from sampling errors. To avoid introducing errors when smoothing high curvature regions in the potentials, we first decompose the potential correction into functional and tabulated components:

$$\Delta V(r) = \Delta\widehat{V} + \Delta\widetilde{V} \tag{2.10}$$

where $\Delta\widehat{V}$ is obtained by fitting the potential correction with a functional form of the potentials and $\Delta\widetilde{V}$ is the residual. For pairwise interactions a 9–6 Lennard–Jones potential is chosen as the functional form, whereas the dihedral term of the Class II force field [61] is chosen for the torsion interactions. The residual term $\Delta\widetilde{V}$ is then smoothed using a Savitzky–Golay filter using a window length of 9 and polynomial order of 2. The procedure to update pair and dihedral potentials is summarized in Algorithm S3.

At each iteration in the IBI process, a linear correction term is added to the pairwise

Algorithm S3 Update tabulated potential

procedure TABULAR(V_i, P^*, P^i)
  Compute scaling factor $\alpha(r)$
  Compute ΔV
  if update $V(r)$ **then**

$$[\sigma, \epsilon] = \arg\min_{\sigma,\epsilon} \left(\Delta V(r) - \epsilon \left[2 \left(\frac{\sigma}{r} \right)^9 - 3 \left(\frac{\sigma}{r} \right)^6 \right] \right)^2$$

  else if update $V(\phi)$ **then**

$$[K_n, \phi_n] = \arg\min_{K_n,\phi_n} \left(\Delta V(\phi) - \sum_{n=1}^{3} K_n[1 - \cos(n\phi - \phi_n)] \right)^2$$

  end if
  $\Delta\widetilde{V} = \Delta V - \Delta\widehat{V}$
  $\Delta\widetilde{V} \leftarrow$ savgol_filter($\Delta\widetilde{V}$)
  $V_{i+1} \leftarrow V_i + \Delta\widehat{V} + \Delta\widetilde{V}$
  Compute force $f_{i+1} = -\frac{dV_{i+1}}{dr}$
  return tabulated V_{i+1} and f_{i+1}
end procedure

potentials to ensure that the resulting pressure in the CG simulations matches the pressure ($p = 1$ atm) in the target atomistic simulations:

$$\Delta V_{pc}(r) = A k_B T \left(1 - \frac{r}{r_c} \right), \tag{2.11}$$

where r_c is the pairwise cut–off distance. Following Wang et al [64], the coefficient A can be calculated from the equation:

$$- \left[\frac{2\pi N \rho}{3 r_c} \int_0^{r_c} r^3 g(r) dr \right] A \approx \Delta P V, \tag{2.12}$$

where ΔP is the difference between the coarse–grained and atomistic pressures, N the number of super–atoms, and V the volume of system.

Proper selection of the scaling factor α in Eq. (4.1) is critical for the robustness and convergence of the IBI method, particularly in a complicated system like polyurea where the relationship between the potentials and distributions of different super–atom

types can be strongly interdependent. Traditionally, α is selected in a trial–and–error process to maximize the rate at which the IBI method converges. However, the optimal scaling factor α is not consistent across all different potentials, and with 98 different potential functions in this CG model of polyurea, a trial–and–error approach is not feasible. Furthermore, we hypothesize that the sensitivity of the RDFs to changes in the corresponding pair potentials is distance dependent. Therefore we developed an adaptive approach that heuristically determines an optimal, distance–dependent scaling factor for the pairwise potential updates. The adaptive scaling functions are updated by the ratio of the target change in the RDFs to the actual change in the RDFs from the previous step:

$$\alpha_i(r) = \alpha_{i-1}(r)\frac{g^*(r) - g_{i-1}(r)}{g_i(r) - g_{i-1}(r)} \tag{2.13}$$

The scaling factor is updated pointwise for each tabulated distance value. The update is applied conditionally to ensure that the scaling function remains bounded, e.g., very small target changes in the RDF are screened out as these are highly susceptible to sampling noise. The adaptive scaling function is applied for the pairwise potential updates only. For all other potentials, we use a constant scaling factor $\alpha = 0.2$.

In summary, the initial estimates for the coarse–grained potentials V_0 were obtained by Boltzmann inversion of the target structural distributions. Initial distributions P_0 of the coarse–grained systems were sampled from the model running with the initial potentials V_0. The iterative Boltzmann inversion algorithm starts with above initial values (V_0, P_0 and P^*), as shown in Algorithm S1. The potentials were then iteratively updated in steps 4 through 8 in Algorithm S1. In potential optimization, pair potentials and dihedral angle potentials are updated by tabulated potential algorithm as shown in Algorithm S3, while harmonic potentials like bond potentials, angle potentials and improper angle potentials are updated via Algorithm S2. Updating potentials is

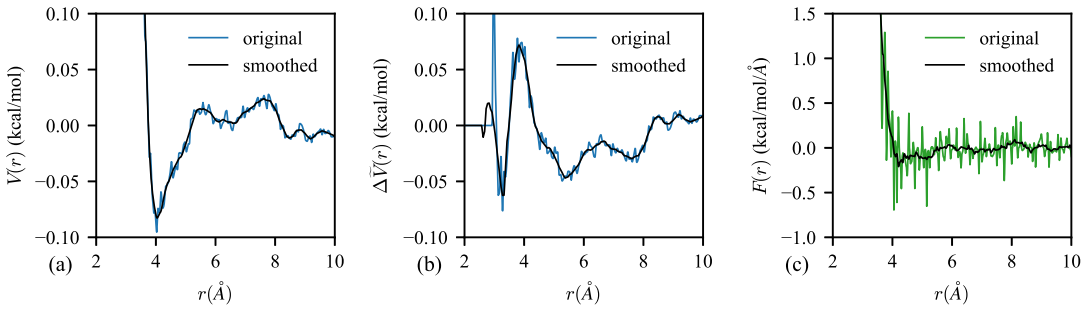

Figure 2.4: Smoothing and updating pair potential of c_2-c_4 from IBI step 0 to 1.

followed by pressure correction to match the coarse–grained pressure to the target atomistic model (1 atm). Next, the coarse–grained distributions are resampled. If the representation error, calculated from the coarse–grained distributions at the current iteration, does not satisfy the convergence criterion, the procedure repeats at step 4 for a new iteration. More specifically, with the input target distribution P^*, the coarse–grained distribution at step i, and the corresponding potential at step i, the distance–based scaling factor α is computed and used to correct the coarse–grained potentials (ΔV) using the ratio of the target and current coarse–grained distributions. The potential correction is then split into analytical ($\Delta\widehat{V}$) and perturbation ($\Delta\widetilde{V}$) parts. The coefficients of the analytical part of the correction are obtained through least squares fitting as shown in Algorithm S3. The perturbation part of the correction is smoothed out by the low–pass filter. Figure 2.4 shows a typical interaction with and without smoothing process from iterative step 0 to step 1. Finally, the summation of the two parts of the potential correction is added to the original potential. Updating harmonic potentials follows a similar procedure, except there is no need to compute adaptive scaling factor and smooth out noise. The coefficients from curve fitting are directly used in the LAMMPS simulations.

2.2.3 Convergence and Error Estimation

To establish the convergence criterion used to terminate the IBI process, we consider two types of error based on the sampled RDFs. The *representation error* is a measure of the difference between the RDFs sampled from the current iteration of the coarse–grained potentials and those sampled from the atomistic simulations. The representation error of an RDF at iteration i is defined as:

$$\epsilon_r^{(i)} = \frac{\|g_i(r) - g^*(r)\|_2}{\|g^*(r)\|_2}, \tag{2.14}$$

where $\|g(r)\|_2 = \left(\int g(r)^2 dr\right)^{\frac{1}{2}}$ denotes the L_2 norm of $g(r)$. The *sampling error* accounts for the uncertainty of the distributions incurred by sampling from a finite number of systems and combines the uncertainty in sampling both the coarse–grained and target distributions. The sampling error is defined as:

$$\epsilon_s^{(i)} = \frac{\sqrt{\left(\|w_i(r)\|_2\right)^2 + \left(\|w^*(r)\|_2\right)^2}}{\|g^*(r)\|_2}, \tag{2.15}$$

where $w^{(i)}(r)$ and $w^*(r)$ are the widths of the pointwise confidence bands of the coarse-grained distribution functions at iteration i and the target all-atom distribution functions, respectively, computed as:

$$w(r) = t^* \frac{\sigma(r)}{\sqrt{n}}, \tag{2.16}$$

where t^* is the critical value for the t-distribution corresponding to a 90% confidence interval, $\sigma(r)$ are the pointwise standard deviations of the distribution functions, and n is the number of systems from which the distributions were sampled and averaged. The target pair distributions with the largest, median, and smallest sampling errors are $o_2 - o_2$, $o_1 - o_3$, and $c_1 - c_1$, respectively, which are shown in Figure 2.5. The

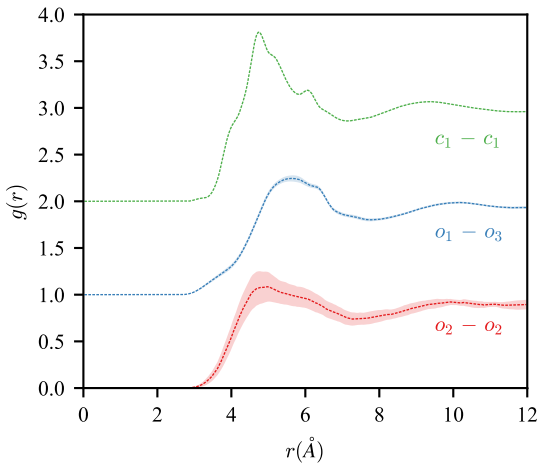

Figure 2.5: Computed RDFs (shifted along y-axis for clarity) of $o_2 - o_2$, $o_1 - o_3$, and $c_1 - c_1$ pair types with shaded regions indicating the 90% confidence intervals.

uncertainty in the $o_2 - o_2$ pair distribution is large due to the relative scarcity of o_2 super–atoms in the polyurea chain.

The key premise in the optimization procedure is that is not meaningful to reduce the representation error beyond the level of sampling error. Therefore, for the initial iterations, only a few coarse–grained systems, e.g., $n = 3$, are needed to sample the structural distribution functions. At each iteration, after sampling the coarse–grained distributions, the mean representation errors of the distributions are compared with the corresponding mean sampling errors. If the representation errors are larger than the sampling errors, the potentials are corrected according to Eq. (4.1), and smoothed using the previously described methods. If at the end of an iteration, the sampling errors become comparable to or larger than the representation errors, then the number of coarse–grained systems is increased to reduce the sampling error in the subsequent iterations. Once the number of coarse–grained systems matches the number of atomistic systems sampled to determined the target distribution functions,

increasing the number of coarse–grained systems becomes less effective at reducing the sampling errors, since at this point, the sampling error is dominated by the number of atomistic systems. Therefore, once the representation error is reduced to less than the sampling error of the atomistic systems, the iteration stops. To further reduce the representation error, more atomistic systems would be required to first reduce the sampling error. However, as the sampling error decreases by the square root of the number of systems, it becomes increasingly computationally prohibitive to further reduce the sampling error. In this work, only the errors of the RDFs were used to control the IBI optimization algorithm as the other distribution functions converge rapidly to their target distributions and thus the accuracy of the RDFs was the limiting factor.

2.2.4 Construction of Model Systems and Computational Performance

To study the morphology of polyurea, we constructed two large model polyurea systems, one composed of 960 $(S_7HS_7)_8$ chains (multiblock system), and the other containing 7,680 S_7HS_7 chains (diblock system) [36]. The number of super–atoms in these CG systems is approximately 831k, corresponding to 1.87M atoms. The model systems were constructed in a randomly mixed configuration at $1/64^{\text{th}}$ scale, replicated 4x along the three spatial dimensions, and then equilibrated to obtain representative microstructures. First, a 20 ns NVT simulation was performed at $T = 800$ K to break the periodic symmetry and reduce the effect of the initial configuration. After that, the temperature was decreased to $T = 500$ K over a span of 10 ns, and run at constant temperature for a further 10 ns. Lastly, the systems the temperature was ramped to $T = 300$ K over 5 ns followed by a final 5 ns equilibration at 300 K.

To examine the efficiency of the coarse–grained model, smaller atomistic and CG polyurea systems with 15 multiblock chains of $(S_7HS_7)_8$ were constructed. The number of atoms or super–atoms in the atomistic and coarse-grained systems were 29,160 and 12,990, respectively. We performed benchmark simulations using these systems that consisted of a 1 ps NVE run on a single processor using both the atomistic and coarse–grained model at their maximum stable time steps. The maximum stable time step is defined as the largest time step in which the drift in total energy is bounded such that $\Delta e/ke < 1\%$, where Δe is total energy drift and ke is average kinetic energy over the simulation run. Due to the elimination of hydrogen atoms and their accompanying high frequency vibrational modes, the maximum stable time step of the model can be increased to 3 fs over the 1 fs of the atomistic simulations. The atomistic simulation runs at a rate of 0.32 ns/day, whereas the coarse–grained model can simulate 5.2 ns/day, giving an effective speedup factor of nearly 16x.

2.3 Results and Discussion

2.3.1 IBI Optimization

We first compare the rate at which the root mean square (RMS) of the representation errors of the CG model is minimized using various fixed scaling factors and by using the adaptive scaling function described in the previous section. The representation errors for the different scaling approaches are plotted at each IBI step in Figure 2.6. When using a fixed scaling factor of $\alpha = 0.05$ or $\alpha = 0.2$, the representation error is reduced to below the sampling error in 18 iterations, however, if the scaling factor is further increased to $\alpha = 0.5$, the corrections to the potential become too

large and the errors begin to oscillate at a level above the sampling error. In contrast, by using adaptively-determined scaling functions, initialized at $\alpha(r) = 0.05$, the errors are rapidly minimized and reach the sampling error threshold in 4 iterations. If the IBI process is rerun, with the adaptive scaling functions initialized to those from the final iteration of the prior optimization, the representation error is reduced to below the sampling error threshold in only 3 iterations, suggesting that the optimal scaling functions are stable over the iterations. Table 2.3 compares the RMS, minimum, and maximum representation errors across all of RDF types at the final iteration for different constant scaling factors and adaptive scaling functions. We note that despite satisfying the RMS error threshold, the maximum errors in the RDFs are substantially larger than those produced using the adaptive or optimized scaling functions.

By using the RMS to combine the individual RDF errors into a threshold criterion, we do not account for the numbers of super–atoms involved in each interaction type, e.g., $o_2 - o_2$ interactions are far more scarce than $c_1 - c_1$ interactions, but their errors are counted equally. However, some relatively rare interactions are important, e.g., $n_1 - o_3$ interactions reflect hydrogen bonding, and so weighting the errors proportional to the number of super–atoms that correspond to the RDF pair types may miss important contributions. Future work is thus needed to establish relative importance factors for each interaction type that can be used to compute more pertinent error metrics.

Next, we focus on the performance of the IBI method using the adaptively-determined scaling functions. The mean representation and sampling errors of the RDFs at each IBI iteration are shown in Figure 2.7, where step 0 indicates the sampling and representation errors arising from coarse–grained simulations using the

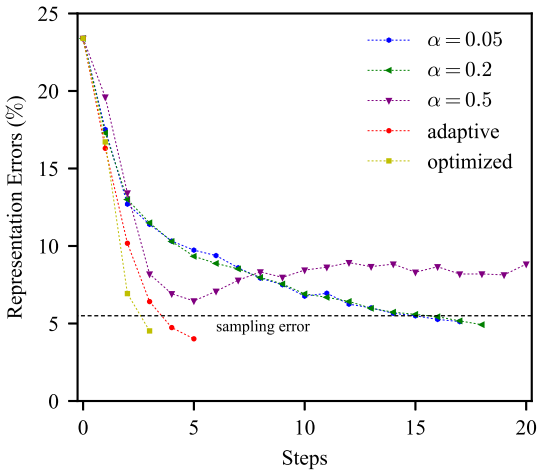

Figure 2.6: History of representation errors of RDF during IBI with different scaling factors.

	adaptive	optimized	$\alpha = 0.05$	$\alpha = 0.2$	$\alpha = 0.5$
RMS	4.0%	4.5%	5.1%	4.9%	8.8%
min	0.95%	2.0%	1.1%	0.74%	0.45%
max	9.6%	9.6%	24%	23%	32%

Table 2.3: Mean, maximum, and minimum representation errors among all RDF types using different scaling factors at final iteration.

initial estimates of the potentials. At iterations 2 and 4, the RMS representation error dropped below the sampling error and so the number of coarse–grained systems sampled was increased. At iteration 5, the RMS representation error was less than the sampling error computed using all 18 systems and thus the iteration was halted. To further reduce the representation error beyond this point would require sampling a greater number of atomistic systems. At the final iteration, the RMS sampling errors of the RDFs of the atomistic and coarse–grained systems were similar with $\bar{s}_e^* = 4.5\%$ and $\bar{s}_e^{(i)} = 4.1\%$, respectively. Like the representation errors, the individual sampling

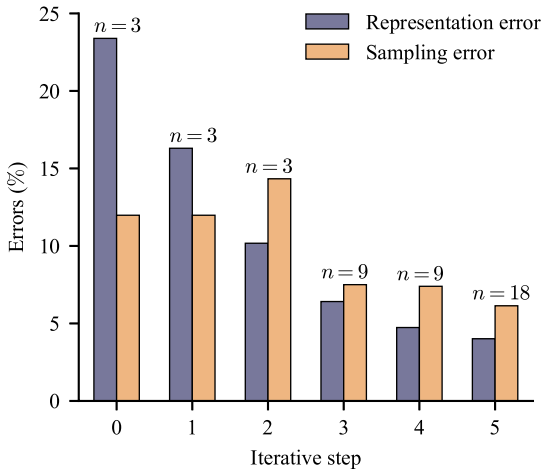

Figure 2.7: History of representation and sampling error of RDF in IBI optimization.

errors are normalized by the L_2 norm of the corresponding RDFs. The representation and sampling errors at the final iteration of the pair, bond, angle, dihedral, and improper distributions are summarized in Table 2.5. The larger representation errors in the angle and bond distributions are a result of limiting the functional forms to quadratic potentials. The resulting optimized potential parameters for the harmonic bonds, bond angles, and improper angles are presented in Table 4.3. LAMMPS input scripts and the full tabulated potentials are available on GitHub [65].

In Figure 2.8 and 2.10, a few representative RDFs ($c_1 - c_1$ and $n_1 - o_3$) and dihedral angle distributions ($c_1 - c_2 - o_1 - c_2$ and $c_5 - n_1 - c_4 - n_1$) are shown to illustrate the accuracy at which the IBI–based training algorithm reproduces the target distribution functions using tabulated potentials. Here, the $c_1 - c_1$ pairwise interaction and $c_1 - c_2 - o_1 - c_2$ dihedral torsion are highlighted as they are among the most common, whereas the $n_1 - o_3$ interaction is shown as it is of key importance to represent hydrogen bonding between sp2-hybridized oxygen atoms and nitrogen

bond type	l_0 **(Å)**	K **(kcal/mol/Å^2)**
$c_1 - c_1$	1.5387	303.55
$c_1 - c_2$	1.5343	306.56
$c_2 - o_1$	1.4254	384.81
$c_2 - o_2$	1.4309	389.64
$o_2 - c_3$	1.3667	347.75
$c_3 - o_3$	1.2153	822.65
$c_3 - c_5$	1.4850	331.52
$c_5 - c_5$	1.4047	479.98
$c_5 - n_1$	1.3976	323.95
$c_4 - n_1$	1.3718	446.38
$c_4 - o_3$	1.2190	834.66
$c_1 - c_5$	1.5106	323.04
improper type	χ_0 **(deg)**	K **(kcal/mol/rad^2)**
$o_2 - c_3 - c_5 - o_3$	180.00	35.445
$c_3 - c_5 - c_5 - c_5$	180.00	17.779
$c_5 - c_5 - c_5 - n_1$	180.00	17.853
$n_1 - c_4 - n_1 - o_3$	180.00	51.380
$c_1 - c_5 - c_5 - c_5$	180.00	9.6385
angle type	θ_0 **(deg)**	K **(kcal/mol/rad^2)**
$c_1 - c_1 - c_1$	113.47	52.038
$c_1 - c_1 - c_2$	114.03	50.225
$c_1 - c_2 - o_1$	109.56	50.088
$c_2 - o_1 - c_2$	111.70	45.427
$c_1 - c_2 - o_2$	109.90	54.008
$c_2 - o_2 - c_3$	113.28	51.453
$c_5 - c_3 - o_3$	126.15	72.288
$o_2 - c_3 - o_3$	118.10	95.793
$o_2 - c_3 - c_5$	108.97	81.421
$c_5 - c_5 - c_5$	118.34	57.995
$c_3 - c_5 - c_5$	118.11	78.247
$c_5 - c_5 - n_1$	122.22	74.247
$c_5 - n_1 - c_4$	121.18	46.886
$n_1 - c_4 - n_1$	125.60	98.174
$n_1 - c_4 - o_3$	121.14	93.161
$c_1 - c_5 - c_5$	121.86	51.177
$c_5 - c_1 - c_5$	110.75	51.432

Table 2.4: Harmonic bond, angle and improper coefficients for the CG model of polyurea in the format consistent with the harmonic bond and angle styles in LAMMPS.

	RDF	bond	angle	dihedral	improper
$\bar{\epsilon}_s$	6.1%	2.3%	1.9%	5.8%	1.3%
$\bar{\epsilon}_r$	4.0%	7.5%	7.6%	6.3%	1.5%

Table 2.5: Final representation and sampling errors ($n = 18$) of RDF, bond, angle, dihedral and improper distributions.

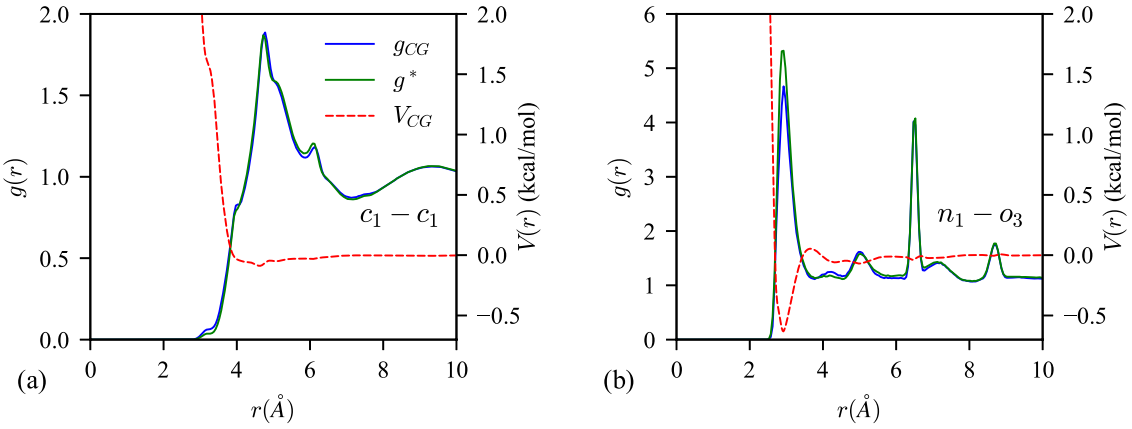

Figure 2.8: Radial distribution functions and potentials for (a) pair types $c_1 - c_1$ and (b) $n_1 - o_3$.

bound hydrogen atoms within the urea groups. The depth of potential well in the $n_1 - o_3$ pair potential (Figure 2.8b) describes the strength of hydrogen bonding in the coarse–grained model. The bond stretch, bond angle and improper angle distributions follow a nearly Gaussian shape and thus are well represented by harmonic potentials. They are omitted here for brevity, but representative distributions and the resulting potentials are presented in Figure 2.9.

Another key benefit of the adaptively determined scaling functions is that the resulting coarse–grained potentials are able to more accurately represent strong interactions. In particular, the sharp peak in the $o_3 - n_1$ RDF is better represented by the coarse–grained potentials trained with adaptive scaling functions than from those

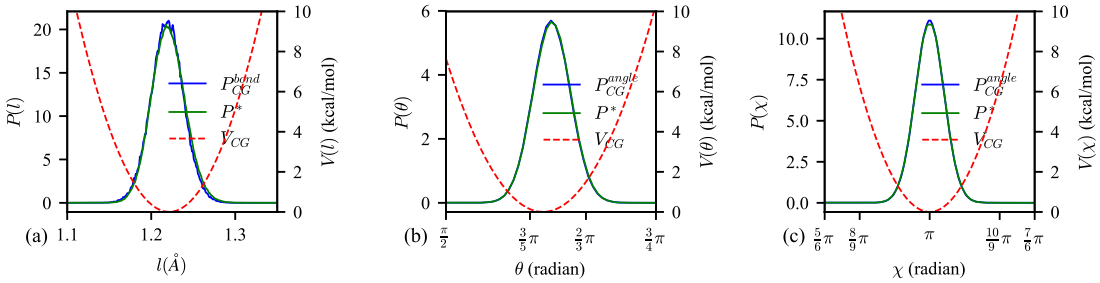

Figure 2.9: Bond stretch, bond angle and improper angle distributions and corresponding potentials of typical interactions. (a) Bond type $c_4 - o_3$. (b) Angle type $c_5 - c_1 - c_5$. (c) Improper angle type $n_1 - c_4 - n_1 - o_3$.

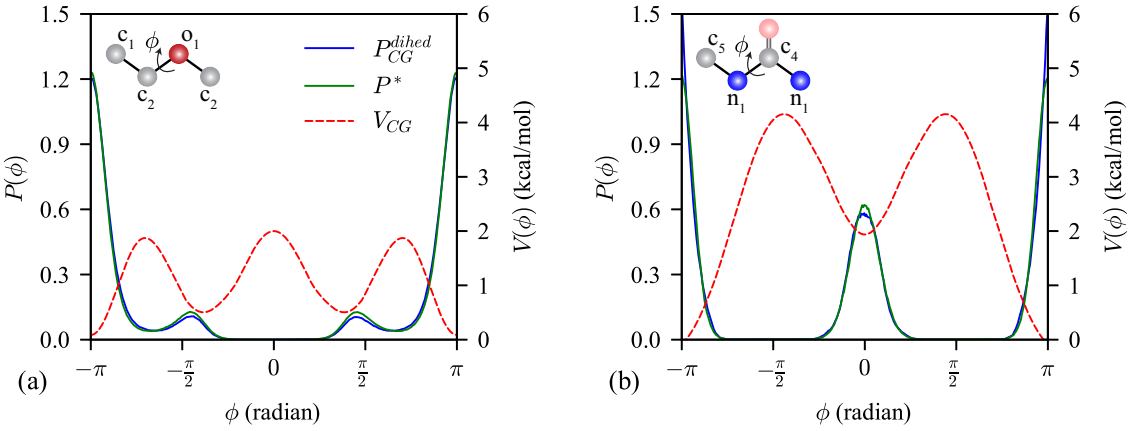

Figure 2.10: Dihedral angle distributions and corresponding potentials for (a) dihedral angle types $c_1 - c_2 - o_1 - c_2$ and (b) $c_5 - n_1 - c_4 - n_1$.

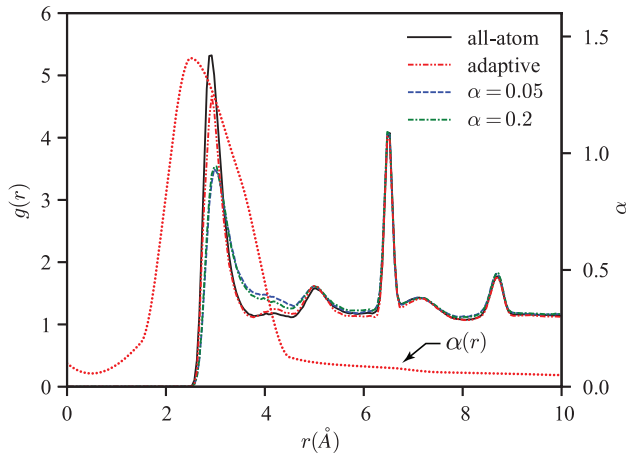

Figure 2.11: RDFs of $n_1 - o_3$ pair type sampled from all–atom model and CG models developed using various fixed scaling factors and adaptive scaling function.

developed using constant scaling factors as can be seen in Figure 2.11. The adaptively determined scaling function for the $o_3 - n_1$ pair type shows that the distributions are less sensitive to the corresponding $o_3 - n_1$ pair potential than expected from a Boltzmann distribution, as indicated by values of $\alpha(r) > 1$ in the neighborhood of the peak. As discussed previously, the $o_3 - n_1$ pair interactions are particularly important as they implicitly account for hydrogen bonding, and thus the ability to account for distance-dependent variations in sensitivity of the RDFs to the pair potentials is a potentially substantial improvement to the IBI method.

2.3.2 Microstructure of Polyurea

The morphologies of the equilibrated diblock and multiblock systems are shown in Figure 2.12. In both systems, the hard segments self-organize from an initially randomly mixed state into ribbon–shaped hard domains surrounded by a matrix composed of soft segments. To quantify the microphase structure, we calculated the

RDFs of the super–atoms in the hard domains, shown in Figure 2.13. Similar to a two point correlation function, the RDFs of the hard segment super–atoms provide a reasonable estimate of the characteristic microstructural length scales of the hard domains [66]. The local minimum within the RDF of the hard segment super–atoms corresponds to the characteristic thickness of the ribbon–shaped hard domains, and is located at $r = 2.85$ nm and $r = 2.95$ nm in the multiblock and diblock systems, respectively. The local maximum of the RDFs identifies the mean–interdomain spacing of the hard domains [67], which is located at $r = 5.05$ nm and $r = 5.25$ nm in the multiblock and diblock systems, respectively. The computed interdomain spacings are slightly smaller than the reported 7 nm interdomain spacing measured by x-ray scattering in polyurea [11, 12, 27].

In general, force fields derived by structure matching methods such as IBI are state–dependent [68]. Since the dynamics of the atomistic system are much far too slow for the simulations to produce a phase–segregated morphology on time scales accessible to MD simulations, the target distributions were sampled in a mixed, nonequilibrium state. Therefore, it is reasonable to question whether or not the force fields are representative of the atomistic system in the phase–segregated state. To assess how well the force fields are transferable to the phase–segregated state, we performed a reverse mapping, i.e., by adding the hydrogen atoms back to the phase–segregated multiblock system, and briefly relaxed the system using a 1 ns NVT simulation at 300 K. Following this, the atomic trajectories were sampled, from which RDFs were calculated and compared to RDFs calculated from the coarse–grained system, shown in Figure 2.14 and 2.15. The difference between reverse-mapped and coarse-grained RDFs was then calculated using Eq. (3.8). Red, yellow, and green plot backgrounds represent hard–hard, hard–soft and soft–soft pair types, respectively.

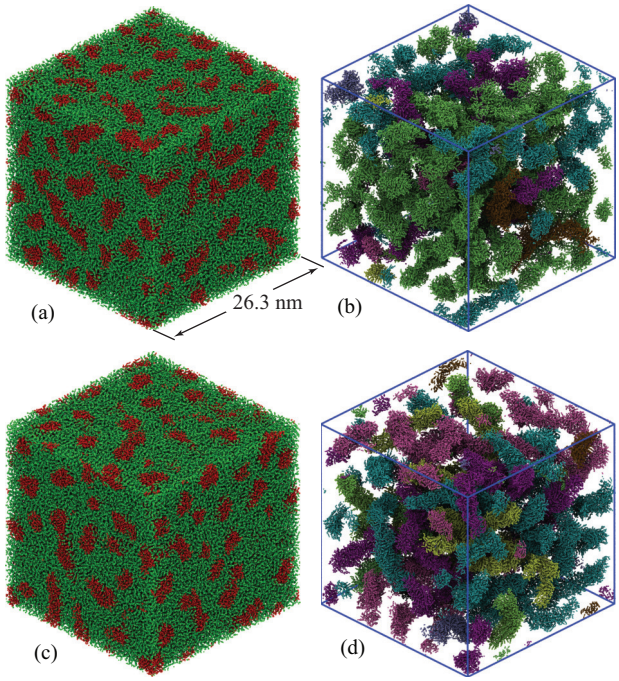

Figure 2.12: Morphologies of CG systems. (a) Multiblock system after equilibration. (b) Hard domains in equilibrated multiblock system. (c) Diblock system after equilibration. (d) Hard domains in equilibrated diblock system. For visualization purpose, super–atoms in hard segment are represented by red spheres and super–atoms in soft segment are green spheres in (a) and (c). Different colors are assigned for different hard domains in (b) and (d).

The representation errors of the coarse–grained models are given as ϵ_r in each plot. The structure of the soft domains was well reproduced with a mean error of 5.4%, whereas there was significantly more error in the hard domains with a mean error of 26%. The RDFs between atoms in the soft and hard domains had a mean error of 12%. Generally, the errors in the hard domain RDFs were caused by a nearly uniform shift in the CG distributions, suggesting that the density of the hard phase in the CG models is somewhat overpredicted.

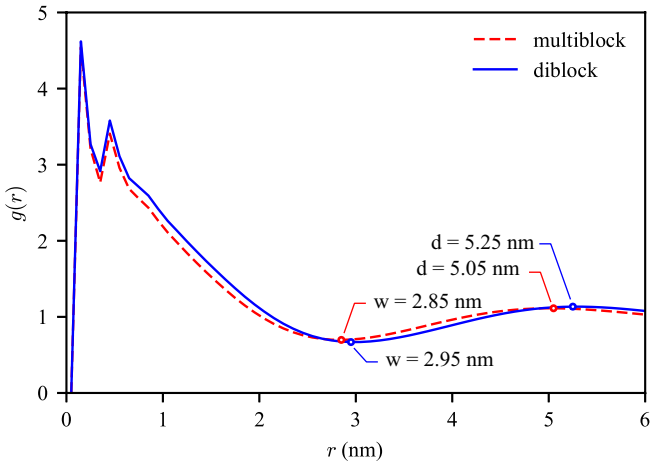

Figure 2.13: Pair correlation function of super-atoms in hard domains.

As the long range connectivity of the hard phase has been associated with large energy dissipation under large deformation, we analyzed the hard domain connectivity by segmenting the hard segments into domains by a distance–dependent criterion, in which two hard segments are considered to be within the same hard domain if their centers of mass are separated by less than 4.5 Å. This distance was chosen to be slightly more than the location of the peak in the $n_1 - o_3$ RDF, which represents hydrogen bonding in the CG model. The resulting segmented hard domains of the multiblock and diblock systems are shown in Figure 2.12b and 2.12d, respectively. Ignoring the small percentage ($< 0.5\%$) of isolated hard segments dissolved within the soft domains, there are 34 unique hard domains within the multiblock system and 28 hard domains within the diblock system. Despite having a greater number of hard domains than the diblock system, more than half of the hard segments in the multiblock system are contained within a single hard domain. In contrast, the connectivity of the hard phase in the diblock system is more interrupted, with the largest hard domain containing less than 23% of the hard segments. The interconnected or percolated [69] structure of

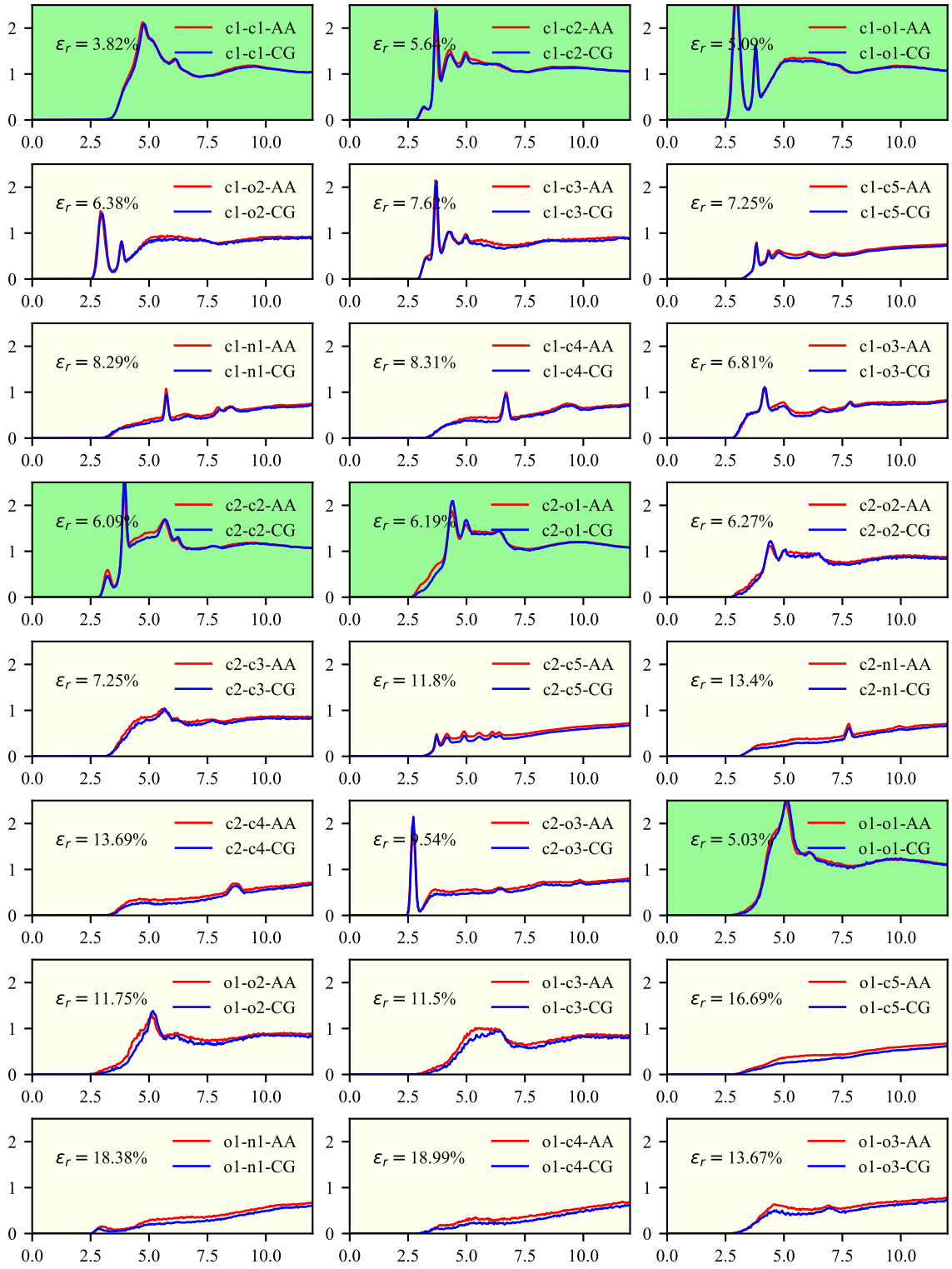

Figure 2.14: Comparison of soft–soft and hard–soft RDFs sampled from the coarse-grained and atomistic phase segregated systems.

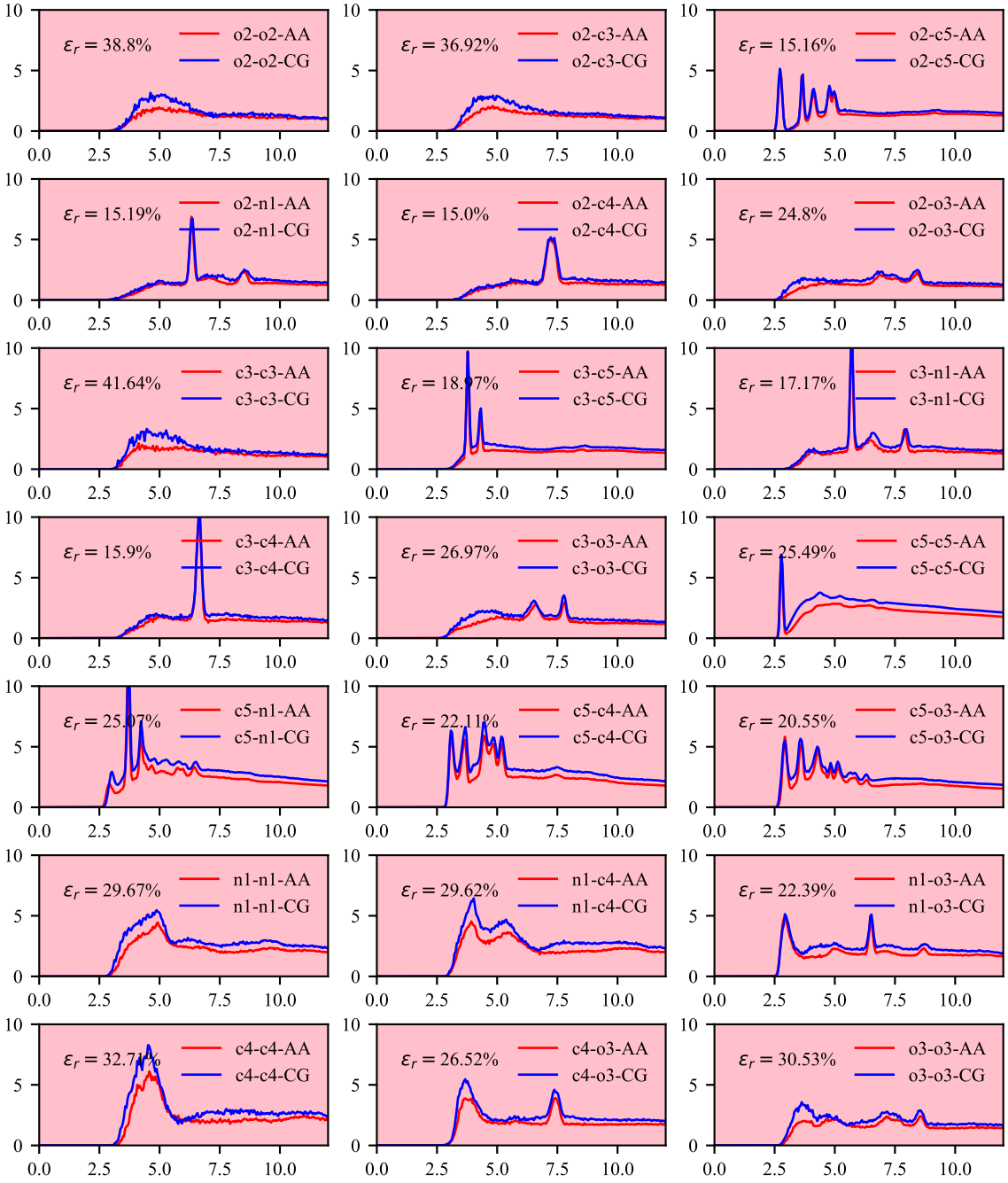

Figure 2.15: Comparison of hard–hard RDFs sampled from the coarse-grained and atomistic phase segregated systems.

the hard domain, particularly within the multiblock system has also been observed in AFM measurements of polyurea [20, 70] and analyzed in computational studies [49].

In the multiblock system, the hard domains are interconnected by the covalently bonded soft segments. The nature of the topology of the soft segments varies between a loop connecting two soft segments within the same hard domain and a bridge connecting soft segments within different hard domains. The degree of this connectivity in polyurea was studied previously by Arman et al. [36], using a simple bead–spring model of polyurea that produced rod–shaped domains. However, given the high degree of long range hard segment connectivity the distinction between bridge and loop soft segments is blurred. However, we observe that distribution of soft segment end–to–end distances, shown in Figure 2.16, closely follows the sum of two normal distributions: the first centered at $r = 0.99$ nm and the second centered at $r = 2.96$ nm. This observation suggests that there are two populations of soft segments, of which we hypothesize the former is composed of loop-like segments and the latter is composed of bridge-like segments. Integration of the normal distributions implies that 18% of the soft segments form loops, whereas 82% form bridges. Although this differs significantly from the composition of loop and bridge segments predicted in the polyurethane systems studied by Zhu et al. [43], we note that the interdomain spacing of their model polyurethane was significantly larger and thus with the much closer hard domain spacing considered here, a higher percentage of bridging segments is expected.

We also investigated whether there is $\pi - \pi$ stacking or any other discernible structure of the aromatic rings within the hard domain. The local p_2 order parameter [71] was computed for each ring using the equation

$$p_2(i) = \left\langle \frac{3\cos^2\theta_{ij} - 1}{2} \right\rangle_j , \tag{2.17}$$

where θ_{ij} is the angle between the normal directions of rings i and j, and the average is

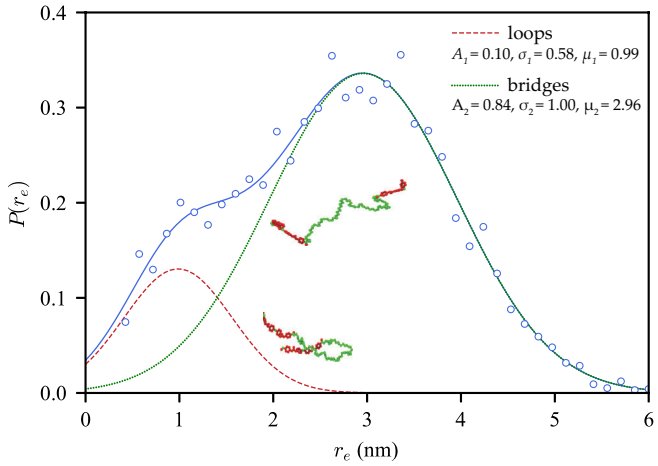

Figure 2.16: Distribution of end–to–end distances of soft segments connected to hard domains in the multiblock system. The raw histogram data (blue circles) is fit to $P(r_e) = A_1 e^{(r_e-\mu_1)/(2\sigma_1^2)} + A_2 e^{(r_e-\mu_2)/(2\sigma_2^2)}$ (solid blue line), where the first and second terms give the distributions of loop–like (dashed red line) and bridge–like (dotted green line) segments, respectively.

taken over all rings j such that the distance between the centers of mass of rings i and j is less than 3 nm. The resulting distributions of the ring p_2 order parameters for the diblock and multiblock systems were identical and closely follow a normal distribution with a zero mean and a standard deviation of $\sigma_{p_2} = 0.04$. This indicates that the aromatic rings are completely unstructured within the amorphous hard domains, which is consistent with the lack of any observable crystalline peaks in the wide angle x-ray scattering measurements of polyurea [48].

As described previously, hydrogen bonding in our coarse–grained model is represented through the $n_1 - o_3$ super–atom interactions. We characterized the hydrogen bond network in the multiblock system by computing the average number of hydrogen bond interactions on each hard segment. In the analysis, hydrogen bonds were detected between n_1 and o_3 super–atoms when their separation distance was within 3.8 Å, which

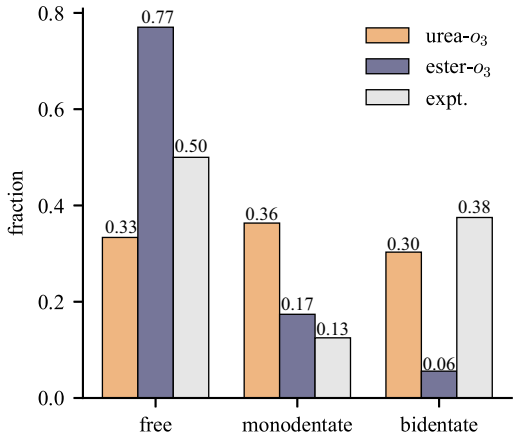

Figure 2.17: Fraction of o_3 super–atoms in urea and ester groups with free, monodentate, or bidentate hydrogen bonding compared with experimental data.

is just beyond the first peak in the $n_1 - o_3$ RDF. The average number of hydrogen bonds per hard segment is 5.4. Most hydrogen bonds are formed from the carbonyl o_3 super–atoms in the urea group, compared to a smaller set of hydrogen bonds formed from the carbonyl o_3 super–atoms in the ester group. Figure 2.17 shows the degree to which the o_3 super–atoms participate in hydrogen bonding, where free, monodentate, and bidentate indicate zero, one or two hydrogen bonds per o_3 super–atom. More than 65% of urea o_3 super–atoms have at least one hydrogen bond, compared to 25% of ester o_3 atoms. The overall percentage of hydrogen bonded carbonyl atoms predicted by the model is 45%, which is within the range of values (45-50%) reported by Li et al. [48] from Fourier transform infrared spectroscopy (FTIR) measurements. However, the model predicts a smaller ratio of bidentate to monodentate o_3 super–atoms than reported by Li et al.

2.4 Summary

In this study, we have developed a systematically coarse–grained model of polyurea at the same resolution of united atom models. To address the high complexity of the model (98 different potential functions were trained simultaneously) we developed a technique to heuristically determine optimal scaling factors for each of the pairwise interactions as a function of the pair distance. This approach greatly improves not only the rate at which the algorithm converges, but also the resulting accuracy by which the model reproduces the target distribution functions.

Beyond reproducing the target structural distributions, further work is needed to fully understand the limits to which the current model is applicable. First, while the dynamics of the resulting coarse–grained model are clearly accelerated compared with the underlying atomistic model from which they were derived, work is ongoing to carefully verify that the relaxation time constants of the model are accelerated consistently [72]. However, this a significant challenge, as there is a wide range of timescales associated with the multiple relaxation mechanisms in polyurea. Secondly, the morphology predicted from the CG model developed in this work shows far more long range connectivity than from prior CG models developed for polyurea [36, 37, 39]. However, none of these prior models have the resolution needed to resolve structure within the hard domains, e.g., hydrogen bonding or ring structures. One possible future direction is to examine how the degree of coarse–graining affects the resulting coarse–grained morphology. Thirdly, we observe some degree of transferability error when applying coarse–grained potentials derived at a mixed state to a phase segregated state. Another future direction would be to resample target distributions in the phase segregated state from which the CG model could be retrained.

Despite these outstanding issues, the model develop here gives new insight to the morphology of polyurea, including evidence of long range connectivity of the hard domains, and predicted length scales that are surprisingly consistent with those determined by x-ray scattering experiments despite extremely short time scales accessible to MD simulations. Analysis of the end–to–end lengths of the soft segments suggests that soft segments belong to two different populations: most soft segments bridging across different branches of the hard phase, whereas a smaller percentage of soft segments form loop structures. Consistent with x-ray scattering measurements, the model predicts an amorphous hard phase with no apparent ordering of ring structures. Lastly, the model provides insight to the nature of the interconnected network of hydrogen bonds within the hard phase. In conclusion, this study lays the groundwork to combine molecular modeling at multiple scales, i.e., fully atomistic and several different degrees of coarse–graining, to explore the relationships between polymer structure, molecular relaxation mechanisms, and macroscopic behavior.

Chapter 3

COARSE–GRAINED MOLECULAR SIMULATION OF THE ROLE OF CURING RATES ON THE STRUCTURE AND STRENGTH OF POLYUREA

3.1 Introduction

Thus far, research work reported using molecular dynamics simulations of polyurea has not considered how the step–growth polymerization process affects molecular structure, but instead have focused on modeling post polymerized molecules to study the role of hard segment composition [73], molecular weight of the soft segment [37, 38] and overall molecular weight [36, 39] on structure and bulk properties. However, the step–growth polymerization process generates a polydisperse molecular weight distribution, which has been shown to strongly influence the microphase structure of block copolymers [74–76]. Furthermore, as the polyurea molecules grow during polymerization, their dynamics should rapidly decrease due to increased entanglements. Thus in this work, we aim to simulate step–growth polymerization in conjuction with phase segregation to develop new insight as to how processing parameters can affect the structure and properties of polyurea.

To generate molecular systems close to real polymer network, researchers started modeling the curing process of polymers via reactive molecular dynamics and coarse–graining [77–80], which is traditionally constructed with a mixture of prepolymers randomly placed in a simulation cell and allowance of covalent bond formation when reactive monomers satisfy a bonding criterion. Such curing modeling simultaneously allows molecular relaxation and bonding formation, which takes the effect of molec-

ular diffusion into topological construction. Many algorithms have been published in literature for generation of polymeric materials. Abbott et al. [81] proposed a polymerization algorithm with distance–based bonding criteria and a 21–step high pressure/temperature relaxation process to accelerate relaxation in glassy polymers. Gissinger et al. [82] proposed an algorithm capable of modeling multi–step reactions for more complicated polymerization scenarios which was implemented and distributed within the USER–REACTION package as part of the open–source LAMMPS molecular dynamics code [59, 83]. Therefore, by mimicking the process of polymerization and controlling the polymerizing conditions, studies have been established to investigate the effect of conversion rate [84], crosslinking density [85], and prepolymer length [86] on the resulting structure and mechanical properties in various polymeric materials.

In this section, we describe a systematic coarse–grained model developed for simulating the effect of curing process on high strain rate mechanical properties of polyurea. The step–growth polymerization of polyurea was simulated via a distance–based bonding criterion with differing reaction speeds. After characterizing the morphological and topological behaviors of the polymerized model systems, we performed simulations in which the simulation cells were compressed under uniaxial stress and analyzed the structural evolution and stress response of the systems in order to infer relationships linking processing conditions, molecular structure, and mechanical properties.

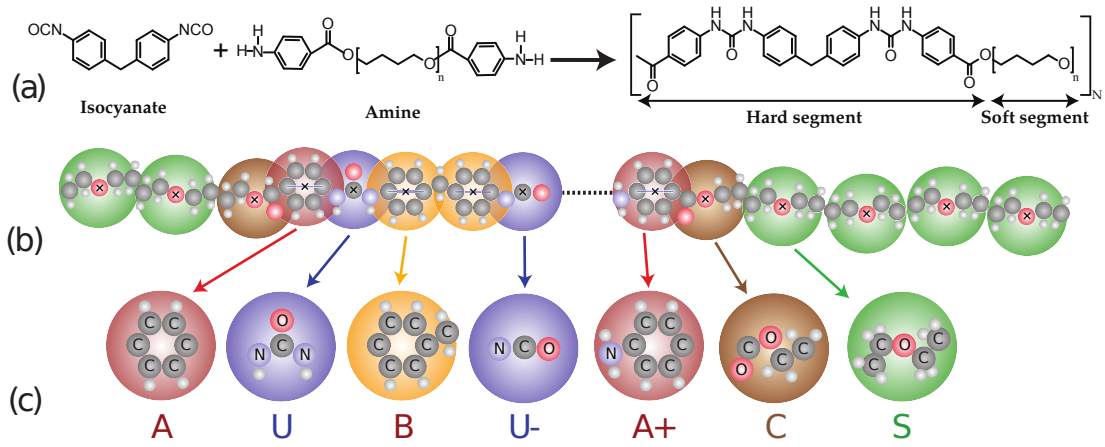

Figure 3.1: Chemical formulation and coarse–grained mapping scheme.

3.2 Methodology

3.2.1 Coarse–Grained Model

A coarse–grained model for simulating step–growth polymerization in polyurea was developed using the iterative Boltzmann inversion method (IBI) [52]. Our methodology is based upon previous works by Agrawal et al. [40] and Liu et al. [79], and thus we briefly summarize the procedure and key differences here. Our polyurea model is based on the pre–reaction compositions for polyurea synthesis, which are idealizations of Isonate 143L modified MDI (polycarbodiimide-modified diphenylmethone isocynate) and Versalink® P–1000 oligomeric diamine. The reaction formulation, chemical structures, and coarse–grained mappings of the chemical units of the prepolymers and polyurea are shown in Figure 3.1. The coarse–grained polyurea chain is defined by 5 unique types of super–atoms, wherein the soft segment is represented by a series of S super–atoms, and the hard segment is made up of A, B, C, and U super–atom types, in which the A and B super–atoms represent ring structures, the U super–atom

represents the urea linkages, and the C super–atom type represents the ester linkage that connects to the soft segment. Two new super–atom types, U^- and A^+, are introduced to represent the prepolymers' isocyanate and phenyl amine end groups, respectively. The resulting model therefore has 7 unique types of super–atoms of which 2 are reactive. After that, We are choosing the mapping scheme of coarse–grained model attempting to reduce the correlation of bond and angle interactions and also trying to satisfy the momentum consistency in phase space [87], but these two conditions are difficult to be satified at the same time. Therefore, the mass–center is defined as the geometrical center of each super–atom to reduce the bond–angle correlation and the masses of most of the super-atoms are equal to the summation of their constituent atomic masses, whereas the masses of–CH_2– group in super–atom B and the –NH_2 group in super–atom A^+ are excluded. The mass and coarse–graining weight of each super–atom type is summerized in Table 3.1 and Figure . Note that the mapping scheme and super–atom masses of coarse–grained model are chosen with high priority of preserving the time step of coarse–grained simulation and reducing the correlation between bond and angle interactions, which may not completely satisfy the momentum consistency condition. With this mapping definition, the coarse–grained isonate, diamine, and polyurea molecules are represented as U^-BBU^-, $A^+CS_nCA^+$ and $A^+CS_n(BUACS_nCAUB)_NBU^-$ in which n denotes the number of repeated tetramethylene oxide of soft segments and N represents the number of times the $BUACS_nCAUB$ blocks are repeated in a chain.

Super–atom type	Molecular Weight (g/mol)
A	76
B	83
C	72
S	72
U	58
A^+	92
U^-	42

Table 3.1: Definition of super-atom types and corresponding super–atom masses.

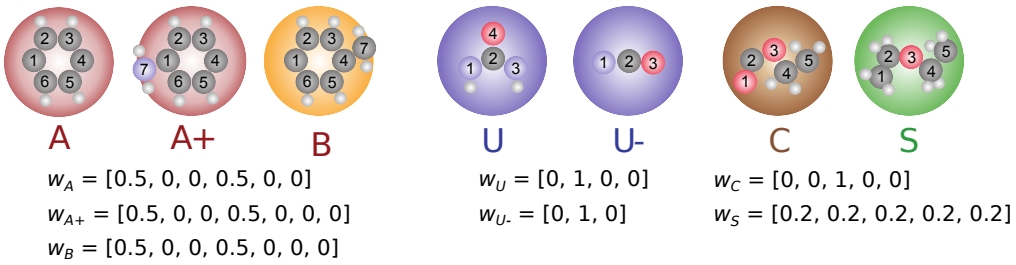

Figure 3.2: Atomic weights used to calculate CG_2 bead coordinates.

The target structural information from which the coarse–grained model is calibrated includes the bond length, bond angle, and radial distribution (RDF) functions calculated by mapping all–atom simulation trajectories to coarse–grained coordinates. The atomistic simulations are performed using the Condensed–phase Optimized Molecular Potentials for Atomistic Simulations Studies (COMPASS) force fields [60, 61], where long–range Coulombic interactions are calculated using the particle–particle/particle–mesh (PPPM) method in the LAMMPS kspace package [83]. Both the cut–off distances of Lennard–Jones interactions and short–range Coulombic term are set to be 9.5 Å. The atomistic systems are constructed by randomly placing twenty oligomeric polyurea chains within a periodic simulation box. The chemical structure of the oligomeric

chains is shown in Figure 3.3 and reflects the composition of the reaction between a pair of diamine and diisocyanate prepolymer molecules. To both quantify and minimize sampling errors, ten atomistic systems were constructed over which the target distributions are averaged. Each system contains 20 short polyurea chains and these chains are randomly distributed in a 36.3×36.3×36.3 Å cubic box. The equilibrium procedure of atomistic systems started with an elevated temperature $T = 500$ K, above the melting temperature of the hard domains, and $p = 1$ atm within 8 ns isothermal–isobaric ensemble (NPT). After that, the temperature was ramped down to $T = 300$ K over a duration of 8 ns and the equilibration was further performed for 16 ns. The atomic trajectories were then sampled in 1 ns canonical ensemble (NVT) for computing target local structures. The first–bonded neighbors are excluded in the calculation of RDFs.

The coarse–grained force fields are determined using the IBI method, in which the bond stretching energy $V_{str}(l)$, angle bending energy $V_{bend}(\theta)$ and non–bonded pair energy $V_{nonb}(r)$ potentials are optimized so that the bond length, bond angle, and pair distribution functions of the coarse–grained model match those of the target distributions.

$$V_{tot} = V_{str}\,(l) + V_{bend}\,(\theta) + V_{nonb}\,(r)\,, \tag{3.1}$$

where l is bond length, θ is bending angle and r is the distance between non–bonded super–atoms. The interaction energies of the bond stretching are approximately as quadratic functions:

$$V_{str}(l) = K_b(l - l_0)^2, \tag{3.2}$$

where l_0 is the equilibrium bond length, and K_b is the corresponding stiffness coefficients. The equilibrium bond lengths and stiffness coefficients are different for each unique combination of bond interaction types and calibrated by IBI algorithms

described in following paragraphs. The angle bending and non–bonded pair potentials do not lend themselves to simple functions and thus are implemented by linear interpolation of tabulated energy and force values at specific interaction angles/distances.

The aforementioned tabular and parametric effective potentials are updated through IBI algorithm as:

$$V_{i+1} = V_i + \alpha k_B T \ln\left(\frac{P_i}{P^*}\right), \tag{3.3}$$

where P_i are the distributions, including RDFs, bond and angle distributions, sampled from coarse–grained MD simulations using potentials V_i at iteration i, P^* are the corresponding target structural distributions computed from atomistic systems, k_B and T are Boltzmann coefficient and temperature. Constant parameter $\alpha = 0.2$ is a scaling factor to dampen the potential update and improve the stability of optimization. The initial estimates of effective potentials to start IBI procedure are computed from Boltzmann inversion:

$$V^0_{str}(l) = -k_B T \ln\left(\frac{P^*(l)}{l^2}\right), \tag{3.4}$$

$$V^0_{bend}(\theta) = -k_B T \ln\left(\frac{P^*(\theta)}{\sin(\theta)}\right), \tag{3.5}$$

$$V^0_{nonb}(r) = -k_B T \ln\left(g^*(r)\right), \tag{3.6}$$

where $P^*(l)$, $P^*(\theta)$ and $g^*(r)$ are the target bond, angle and RDF distributions sampled from atomistic simulations. As the coarse–grained distributions approaching target values, the potential corrections become closer to zero values, which leads to a group of effective potentials that is able to make coarse–grained model represent target structural information in atomistic scale. During the optimizing process, since angle bending and pairwise potentials are computed in a tabulated form, a Savitzky–Golay filter using a window length of 5 and polynomial order of 1 was adopted to smooth out

the noise in energy from sampling structural distributions. The harmonic potentials for bond stretching interactions are estimated as quadratic functions, of which the parameters including equilibrium bond length and stiffness are calibrated by curve fitting. The potential values are traversed as numerical data in IBI process and therefore the updated parameters are the best ones that most effectively minimize the difference between parameterized functions and updated data from IBI in each step. The optimized harmonic parameters for running coarse–grained simulations are attached in 4.3. Additionally, a linear correction term is added to the pairwise potentials at each iteration to ensure that the coarse–grained distributions are sampled under the same pressure ($p = 1$ atm) in the target atomistic simulations:

$$\Delta V_{pc}(r) = Ak_BT\left(1 - \frac{r}{r_c}\right), \tag{3.7}$$

where r_c is the pairwise cut–off distance. The coefficient A can be calculated based on thermodynamic consistency, as shown by Wang et al [64]. Finally, a statistical convergence criterion was adopted to terminate the IBI optimization by introducing two types of error: *representation error* and *sampling error* [41]. The representation error measuring the difference between the coarse–grained RDFs sampled from current IBI iteration and target RDFs sampled from atomistic simulations represents the effectiveness of IBI optimization. The total representation error at iterative step i is calculated as normalized root mean–square error of RDFs:

$$\epsilon_r^i = \frac{\|g^i(r) - g^*(r)\|_2}{\|g^*(r)\|_2}, \tag{3.8}$$

where $g^i(r)$ represents the coarse–grained RDFs at iterative step i, $\|\cdot\|_2$ denotes the L_2 norm and $g^*(r)$ is the target RDFs sampled from atomistic simulations. The sampling error accounting for the uncertainty of sampling structural distributions from a finite

number of coarse–grained and atomistic systems is defined as:

$$\epsilon_s^i = \frac{\sqrt{\left(\|w_i(r)\|_2\right)^2 + \left(\|w^*(r)\|_2\right)^2}}{\|g^*(r)\|_2}, \tag{3.9}$$

where $w_i(r)$ and $w^*(r)$ are the widths of the pointwise 90% confidence bands of the coarse-grained distribution functions and the target all-atom distribution functions, respectively, which are computed as:

$$w(r) = t^* \frac{\sigma(r)}{\sqrt{n}}, \tag{3.10}$$

where t^* is the critical value for the 90% confidence interval of t–distribution, $\sigma(r)$ is the pointwise standard deviation of RDFs, n is the total number of sampling systems. The convergence criterion stops the iteration once the representation error is less than sampling error meaning that at this point the IBI training is overfitting and the IBI optimizer is learning the sampling noise.

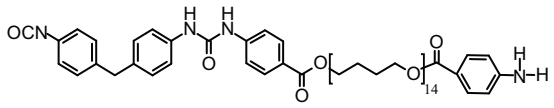

Figure 3.3: Chemical formulation of atomistic systems for sampling target structural distributions.

Eighteen coarse–grained systems for sampling structural distributions were constructed with twenty single–block polyurea chains randomly placed in an unit cell. The super–atoms in initial systems were firstly moved to reasonable positions by performing NVE/limit over a span of 25 ps at $T = 500$ K. Then, the equilibration were started with 25 ps NVT ensemble at $T = 500$ K followed by ramping down the temperature to 300 K over the same time duration. After that, the equilibrium was finalized with running 25 ps NVT simulation at $T = 300$ K. Following the equilibration,

the NVT simulations are continued for 50 ps to sample the radial, bond length and bond angle distributions for IBI optimization. At this coarse–graining degree, the time step of running coarse–grained simulations for equilibrium and sampling local structures is 10 fs.

3.2.2 Simulation of Processing–Induced Microstructure

To model the curing process of polyurea, five initial prepolymer systems were generated by randomly placing a mixture of coarse–grained diamine and diisonate molecules ($A^+CS_{13}CA^+$ and U^-BBU^-, respectively) into periodic simulation cells. The simulation cells were cubic with an edge length of 20.4 nm, corresponding to a density of 1.083 g/cm^3. Each of these initial prepolymer system contains 3800 diamine and 4000 isonate molecules, which reflects the stoichiometry generally used for processing our target variant of polyurea. The systems were briefly equilibrated over a period of 10 ps at 300 K, in which the first 5 ps is performed using a displacement–limiting integrator combined with a Berendsen thermostat and the last 5 ps is performed in the NVT ensemble.

Following equilibration, step-growth polymerization was simulated over a period of 200 ns using the *fix bond/react* command in LAMMPS. At selected time steps during the bonding simulations, pairs of A^+ and U^- super–atoms that are within a distance of 5.5 Å can form a new covalent bond with a probability of 0.5. The super–atom types of newly bonded pairs of A^+ and U^- beads are then transformed to A and U, respectively. In addition to a creation of a new bond, new angle interactions are generated along the sequence of C–A–U and A–U–B beads along the chain. These changes to the bond topology are specified using pre–reacted and post–reacted molecular templates

which are provided as following. A thermostat was performed on the locally dynamic group to relax high–energy interactions after attempts of topology change. And the whole process of chemical reaction was undergoing in canonical ensemble (NVT) at $T = 300$ K and initialized with randomly mixed configurations. All the simulations were performed with a time step of 10 fs and the cut–off distance of non–bonded pairwise interactions was 15 Å. The bonding simulations were performed at four different bonding rates to determine the effectiveness that the reaction rate has on the resulting molecular structure of polyurea. The reaction rate was controlled by varying the time interval for attempting reactions, which ranged from 1 to 1000 ps, resulting in the generation of four sets of cured systems: S_1, S_2, S_3 and S_4. Although these time intervals lead to artificially rapid curing rates, the variation over four decades provides insight as to how the relative timescales of the reaction and molecular diffusion during phase segregation can lead to different molecular structure in the cured state.

Followings are the map templates, including a map file, a pre–reacted template and a post–reacted template, for performing the chemical reaction using our coarse–grained model. The map file contains a bonding atom ID pair and a surrounding atom ID pair in pre–reacted template and the one–to–one atom pairs in pre–reacted and post–reacted templates. The pre–reacted and post–reacted templates show a unit molecular segment that is representative of bonding topology change. In summary, the templates describe that the atom ID 1 (type 4) and atom ID 5 (type 5) in pre–reacted template are the bonding candidates for topology change. And after reaction, the atom ID 1 and atom ID 5 transform from type 4 and type 5 to type 1 and type 7, respectively, and these two atoms are covalently bonded by this operation.

map.txt

```
# this is a map file
2 edgeIDs
7 equivalences
```

```
BondingIDs
1
5
EdgeIDs
4
7
Equivalences
      1      1
      2      2
      3      3
      4      4
      5      5
      6      6
      7      7
```

mol_mixture.txt

```
# Mixture molecule file for reaction simulation of CG2 polyurea
      7 atoms
      5 bonds
      3 angles
Coords
      1      2.359 7.663 5.392
      2      4.841 10.098 3.414
      3      5.453 10.129 -1.452
      4      3.460 10.163 -5.993
      5      1.330 4.322 3.041
      6      3.812 6.757 1.063
      7      6.543 10.586 -0.289
Types
      1      4
      2      3
      3      6
      4      6
      5      5
      6      2
      7      2
Bonds
     1   1      1      2
     2   2      2      3
     3   3      3      4
     4   8      5      6
     5   7      6      7
Angles
     1   1      1      2      3
     2   2      2      3      4
     3   8      5      6      7
```

mol_pu1000.txt

```
# Polyurea molecule file for reaction simulation of CG2 polyurea
     7 atoms
     6 bonds
     5 angles
Coords
      1      2.497 8.111 5.707
      2      4.979 10.546 3.729
      3      5.591 10.577 -1.137
      4      3.598 10.612 -5.678
      5      20.078 25.803 -9.224
      6      16.326 25.282 -9.645
      7      11.905 23.315 -8.906
Types
      1      1
      2      3
      3      6
      4      6
      5      7
      6      2
      7      2
Bonds
     1   4      1      2
     2   2      2      3
     3   3      3      4
     4   5      1      5
     5   6      5      6
     6   7      6      7
Angles
     1   4      1      2      3
     2   2      2      3      4
     3   5      2      1      5
     4   6      1      5      6
     5   7      5      6      7
```

To separate the effects of polymerization rate, polydispersity and molecular weight on the resulting polymer structure and properties, we constructed polyurea systems with equivalent molecular weight distributions of the polymerized systems by sampling the molecular–length distributions with the fastest (S_1) and slowest (S_4) curing rates. Each reconstructed system contains $A^+CS_{13}(BUACS_{13}CAUB)_NBU^-$ molecules in

which the parameter N of each molecule is sampled from the chain length distributions of the corresponding cured systems. The super–atoms in these sampled systems are randomly placed in a simulation box and then equilibrium simulations were performed in the NPT ensemble at $p = 1$ atm and $T = 300$ K for 200 ns during which time, a phase segregated morphology develops. The resulting box lengths of sampled model systems are less than 5% different with the sizes of corresponding cured systems. We found that the radii of gyration in the equilibrated systems were highly correlated with their initial configurations, i.e., after 200 ns of equilibrium, the average radius of gyration changes by less than 10% from the initial configuration. In addition, the bead–spring generator for generating model systems creates an atomic coordinate based on its neighbors, e.g., the random positional vector from super–atom j to super–atom k, $\boldsymbol{r}_{jk}$, is based on the location of atom i, in which i, j and k are three covalently bonded super–atoms and the position of super–atom k is under determined. The length of r_{jk} is the initial equilibrium bond length of bond type between super–atoms j and k. The direction of $\boldsymbol{r}_{jk}$ is determined by a constraint that angle θ_{ijk} is bounded by $\hat{\theta}_{ijk} \pm \epsilon$, where $\hat{\theta}_{ijk}$ is the initial equilibrium angle of the angle type comprised of super–atoms i, j and k and ϵ is tolerance. We found that the initial conformation of generated chains can be qualitatively controlled by the magnitude of angle tolerance by the means that larger tolerance generates model systems with smaller mean gyration radii. Therefore, we adjusted the hyperparameters ϵ of the bead–spring generator to make the radius of gyration placed in a specific range as a second group of sampled systems. For each sampled configuration, three different model systems were generated by randomly sampling from the chain–length distribution of the corresponding cured systems. In total, we have generated four more sets of model systems with progressively increasing radius of gyration but similar molecular weight distribution compared with S_1 and S_4.

The sampled systems with intermediate radii of gyration are named as S_{1A} and S_{4A}, and high radii of gyration are named as S_{1B} and S_{4B}. Table 3.2 summarizes the eight sets of systems generated by different methods.

To assess whether any processing–induced microstructural differences affect the mechanical response of the model polyurea systems, simulations were performed in which the systems were compressed at a constant engineering strain rate under uniaxial stress conditions. Prior to deformation, the systems were equilibrated in the isothermal–isobaric (NPT) ensemble at a constant pressure of 1 atm and temperature $T = 300$ K. Following this equilibration, the systems were compressed to 40% of their original length along the x–axis at a constant engineering strain rate of 6×10^8 s^{-1}. During the deformation, the lateral normal stresses was maintained as $\sigma_{yy} = \sigma_{zz} = 1$ atm by coupling the lateral lengths of the simulation box to a Nosé–Hoover barostat. The time constants of the thermostat and barostat were both set to 0.5 ps. Stress histories were computed using the time and ensemble averged virial stresses [88], where a 10 ps window was used for temporal averaging.

It is worth noting that we are deforming the polyurea box in a really high strain rate without considering the speed up of coarse–graining. However, the dynamic properties of polymers in coarse–grained simulation evolve faster in a wide range of time scales which depends on the degree of coarse–graining. The dynamic scaling function determined by the ratio of mean square displacements from coarse–grained to atomistic simulations reveals the coarse–grained dynamics at this coarse–grained degree is $10^2 \sim 10^3$ times faster than atomistic scale [40]. In addition, we are taking consideration of the effect of curing conditions on the microstructure of polyurea network that may contribute to stress response under deformation. The effect of stress

set	S_1	S_{1A}	S_{1B}	S_2	S_3	S_4	S_{4A}	S_{4B}
method	curing	sampling	sampling	curing	curing	curing	sampling	sampling
frequency (ns^{-1})	1000	–	–	100	10	1	–	–
number	5	3	3	5	5	5	3	3

Table 3.2: Description of model polyurea systems constructed by different methods. Frequency represents the attempted bonding frequency to artificially control the chemical reaction speed.

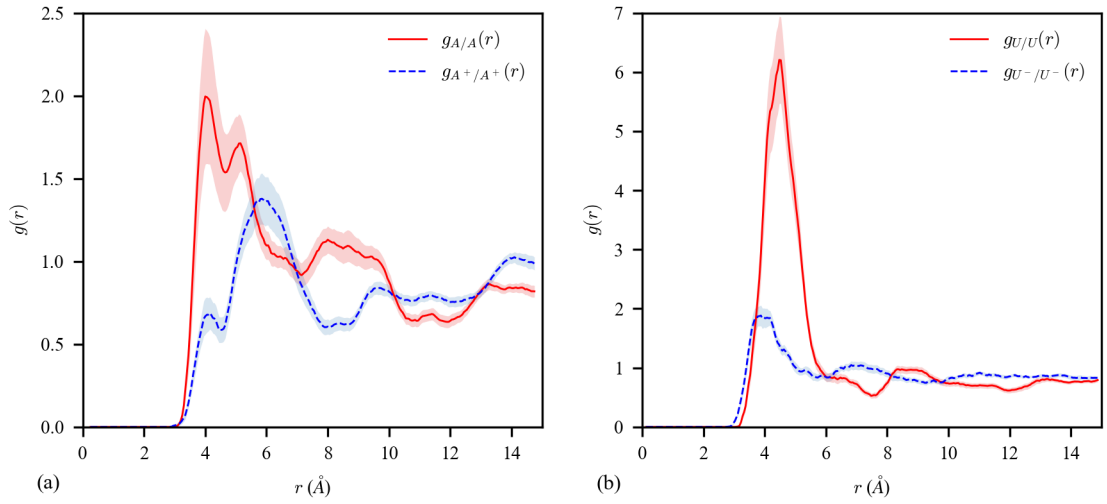

Figure 3.4: The RDFs of pairwise interactions between (a) A–A and A^+–A^+ (b) U–U and U^-–U^- at the final iteration of IBI optimization. The shaded transparent regions indicate 90% confidence intervals of the distributions.

response is supposed to be reflected even though the deformation rate can only be satisfied in a time scale of molecular dynamics.

3.3 Results and Discussion

3.3.1 Calibration of Force Fields

The calibration of coarse–grained force fields were performed by above mentioned IBI algorithm. The optimizing process was terminated after 33 iterations, by which point, the coarse–grained RDFs reproduced the sampled target distributions with a representation error of 4.6%. All the target and resulted distribution functions including RDFs, bond length and bond angle distributions are shown in Figures 3.5, 3.6 and 3.7 and the trained coarse–grained harmonic bond coefficients are shown in

Talbe 4.3. Figure 3.4 displays the resulted RDFs of A–A, A^+–A^+, U–U and U^-–U^- pairs which function as the key interactions of bonding simulations. It can be seen that the RDFs of the A–A and U–U pairs substantially differ from the RDFs of their corresponding reactive super-atoms, i.e., A^+–A^+ and U^-–U^-. More specifically, the larger peaks in the RDFs of the A–A and U–U pairs suggest stronger attractions between A–A and U–U pairs than A^+–A^+ or U^-–U^- pairs, especially among the U–U super–atom pairs. This reflects the stronger underlying interactions among urea functional groups compared to among cyanate functional groups. The RDF of U–U pairs has a large peak located at $r = 4.55$ Å representing the interactions of bidentate hydrogen bonding between urea groups within the hard segments. The predicted urea–urea distance from coarse–grained model is consistent with wide angle x–ray diffraction measurements of polyurea [89] that show a 4.57 Å spacing between urea groups.

3.3.2 Influence of Bonding Rate on Microstructural Evolution

The coarse–grained bonding simulations were performed by the resulting trained force fields for a duration of 200 ns, by which time, the chemical conversion of reactive sites in all bonding cases was higher than 99% and the chemical conversion rates are close to zero. The chemical conversion is defined as the fraction of A^+ super–atoms converted to type A super–atoms. Chemical conversion histories of the reactive coarse–grained systems running with various bonding rates are shown in Figure 3.8.

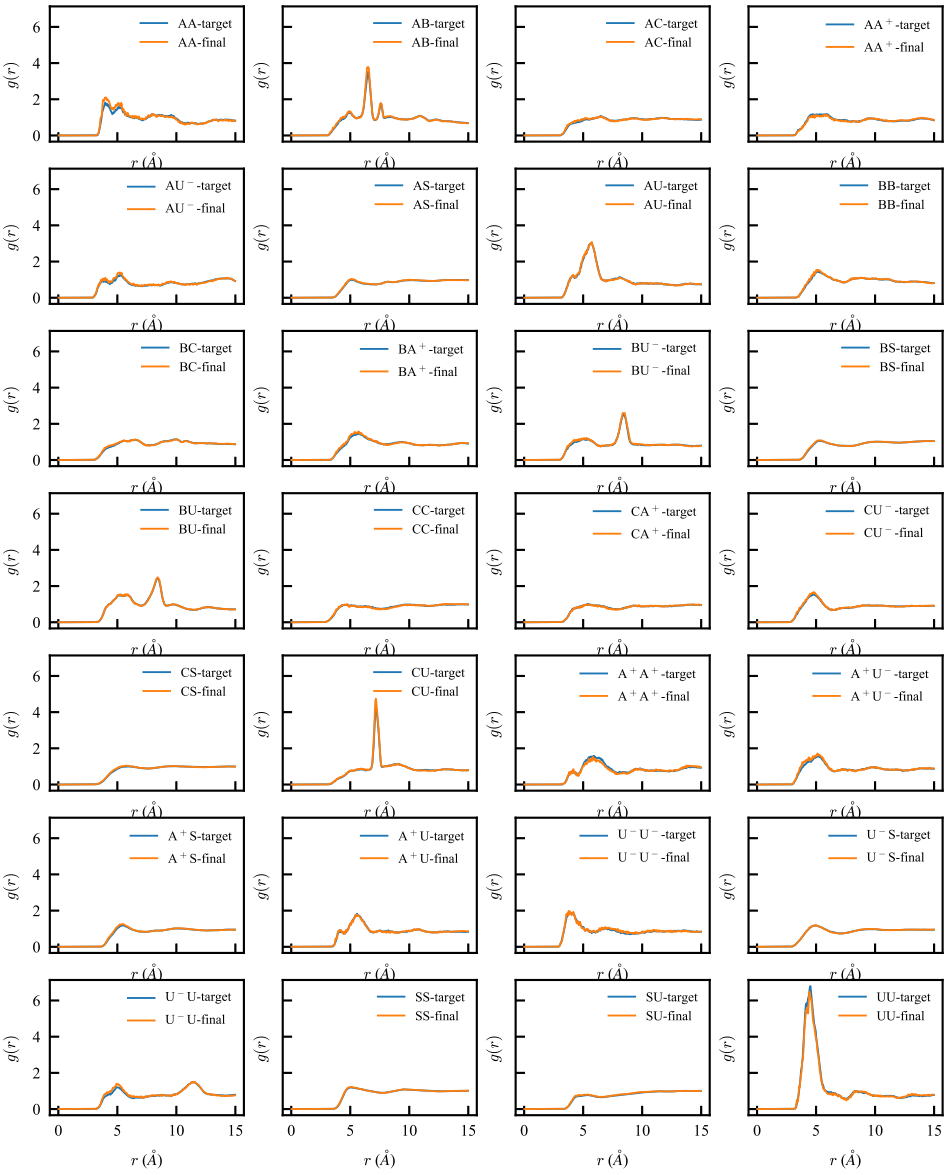

Figure 3.5: The target and CG RDFs of all pairwise interactions at the final iteration of IBI optimization.

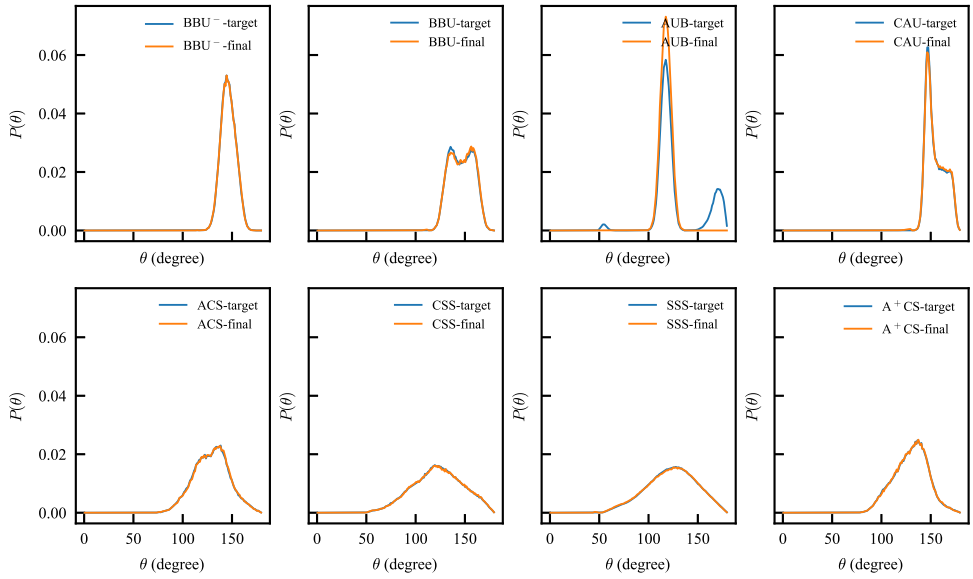

Figure 3.6: The target and CG ADFs of all bond angle interactions at the final iteration of IBI optimization.

bond type	l_0 **(Å)**	K **(kcal/mol/Å^2)**
$S-S$	3.6363	83.29
$C-S$	4.8124	1.126
$A-C$	4.8223	1.535
$A-U$	3.6335	84.47
$B-U$	3.7828	58.23
$B-B$	3.7999	65.91
$C-A^+$	4.8640	13.91
$B-U^-$	3.8954	108.7

Table 3.3: Harmonic bond coefficients for the CG model of polyurea in the format consistent with the harmonic bond and angle styles in LAMMPS.

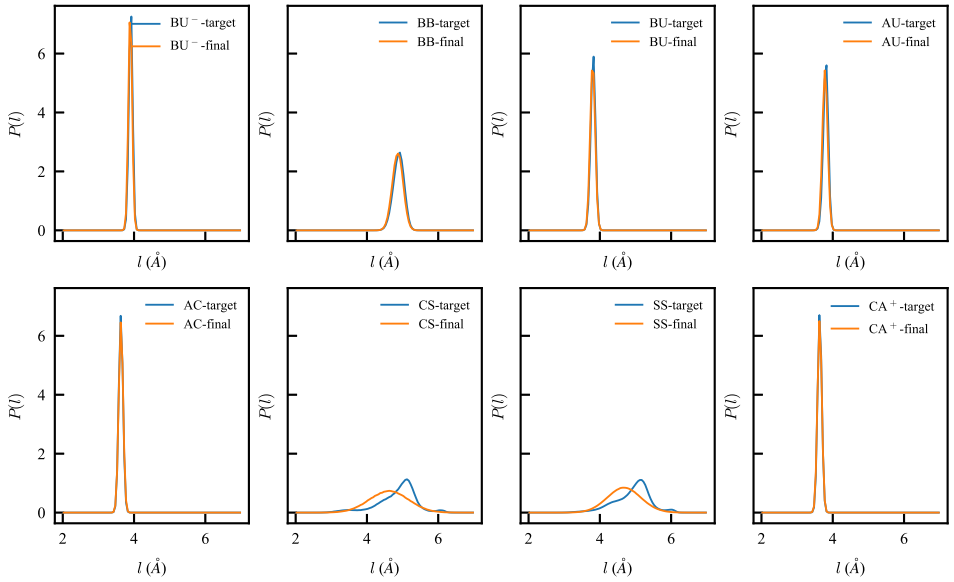

Figure 3.7: The target and CG BDFs of all bond length interactions at the final iteration of IBI optimization.

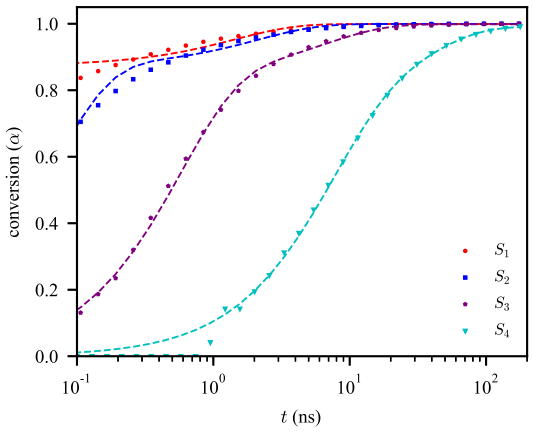

Figure 3.8: History of chemical conversion of bonding simulations within S_1 to S_4. Data points are ensemble averaged over each bonding case. Fits to the data are shown with dashed lines.

Set	f (ns^{-1})	τ_1 (ns)	A_1	τ_2 (ns)	A_1
S_1	1000	1.442	0.126	0.011	0.874
S_2	100	2.135	0.128	0.064	0.871
S_3	10	6.583	0.162	0.561	0.837
S_4	1	32.64	0.275	6.924	0.717

Table 3.4: Fitting parameters of the chemical conversion history for each set of curing simulations.

The conversion time histories are well represented by a biexponential function as

$$\alpha(t) = A_1 \exp(t/\tau_1) + A_2 \exp(t/\tau_2) \tag{3.11}$$

suggesting that the curing process has two characteristic time scales. The fitting coefficients of the biexponential functions are listed in Table 3.4. The shorter of the two time scales τ_2 is inversely proportional to bonding frequency and accounts for 70–90% of the reaction. The longer of the two time scales τ_1 is near inversely proportional to the square root of bonding frequency within the ranges of time scales that are modeled, but the relationship appears to asymptotically reach a constant value at faster reaction rates. This is physically justified, as it should take a finite amount of time for reactive sites to diffuse close enough to react with each other.

To investigate the phase segregation behavior and polymerization degree during polymerization, we report the mean hard–domain thickness (w), inter–domain spacing (d) and weight–average molecular weight (M_w) in terms of simulation time within different bonding frequencies, which are shown in Figure 3.9. The hard–domain thickness and inter–domain spacing are characterized as the locations of the first local minimum and subsequent maximum in the RDF of the hard super–atom types [66], i.e., excluding super–atom type S in the coarse–grained model. As illustrated in

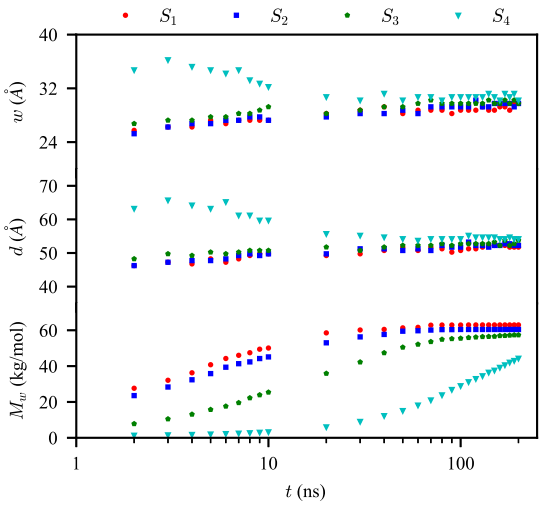

Figure 3.9: Hard–domain thickness (w), inter–domain spacing (d) and weight–average molecular weight (M_w) versus time during polymerization.

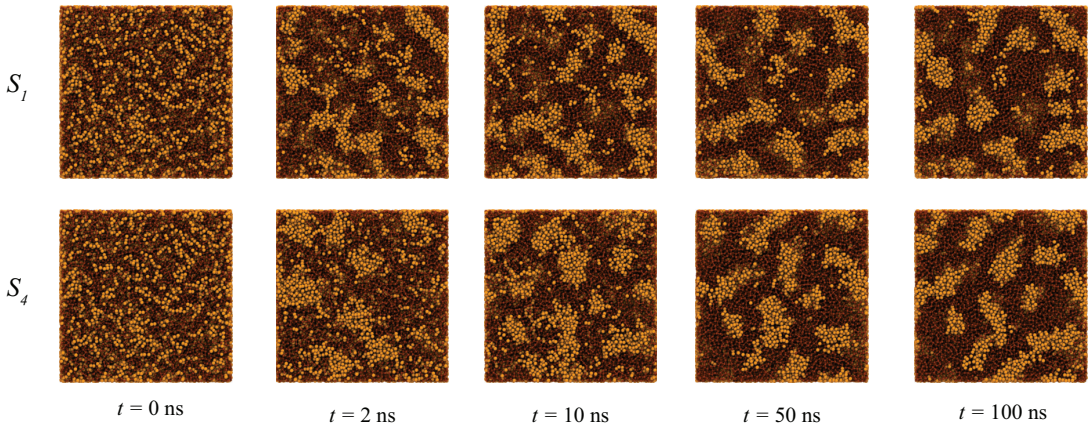

Figure 3.10: Snapshot of S_4 during polymerization at selected timestamps. light brown and dark brown beads represent super–atoms in hard and soft segments, respectively.

Figure 3.10, hard segments rapidly segregate into clusters within the first 2 ns of the simulations. For systems with faster curing rates, i.e., sets S_1, S_2 and S_3, the hard–domain thicknesses steadily increase to a value of approximately 3 nm, which corresponds to the length of the hard segments. The mean inter–domain spacing shows a similar behavior with the hard domain spacing steadily increasing to approximately 5 nm, with the final spacing slightly increasing with slower bonding frequencies. However, the behavior observed for the slowest bonding frequency configuration S_4 was markedly different, with the nearly instantaneous appearance of larger hard domain widths and spacings that steadily decreased over the curing simulations. The weight–average molecular weight of the systems in S_4 remained less than 1.43 kg/mol during the first 2 ns of the curing simulations compared to 7.83 kg/mol for the systems in S_3. At this molecular weight, most of the polyurea chains are diblocks, which were shown to form a coarser phase segregated structure by Arman et al. [36]. To further characterize the phase–segregated morphology, we calculated the RDFs of super–atoms within hard segments at the final state of the simulations, which is shown in Figure 3.11c. The hard–phase RDFs slightly differ within different bonding conditions revealed by locations of valley and peak values at approximately 3 nm and 5 nm, respectively. Therefore, the thickness of ribbon–shape hard domains and inter–domain spacing are extracted from hard super–atom RDFs which are shown in Table 3.5. Accordingly, the hard domain thickness decreases as increased reaction speed, and the inter–domain spacing decreases in the same fashion, suggesting that faster curing speed leads to relatively tighter hard phase.

At the end of the bonding simulations, the hard segments are clustered together to form interconnected ribbon–shaped hard domains surrounded by a soft matrix. Figure 3.11a shows the final morphologies of the different systems, clearly showing

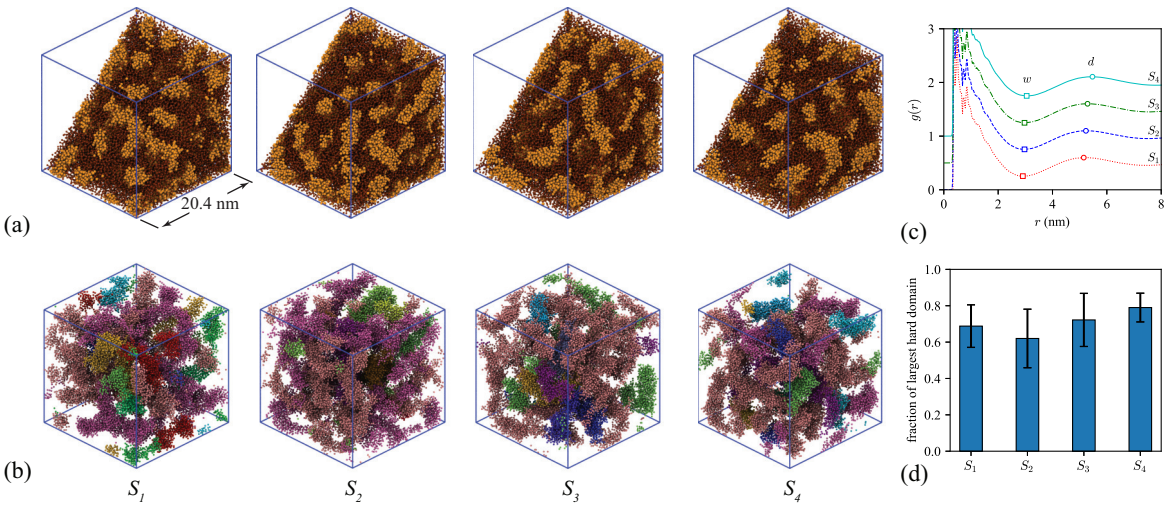

Figure 3.11: (a) Microphase separation in polymerized polyurea systems: green and red beads represent super–atoms in soft and hard domains, respectively. (b) Interconnected structures in hard domains: each hard domain is assigned a unique color. (c) RDFs of super–atoms in hard segments. (d) Mass fractions of the largest hard domain over total hard segments in different bonding frequencies.

that the initially mixed hard/soft super–atoms transform into a phase–segregated morphology for all of the bonding rates considered. We clustered the hard segments into separate hard domains by defining hard segments belonging to the same hard domain if the minimum U–U pair distance between any two hard segments is less than 4.55 Å which corresponds to the location of the first peak in the RDF of U–U pairs which accounts for the hydrogen–bonding interaction. The resulting hard domains, shown in Figure 3.11b, are inter–connected and form a long–range connectivity, consist with experimental observations [11, 14]. Consistently across all modeled bonding frequencies, the largest identified hard domain contained the majority of the hard segments, i.e., more than 60% as shown in Figure 3.11d, indicating that the cured systems tend to form continuous hard domain structure.

set	S_1	S_{1A}	S_{1B}	S_2	S_3	S_4	S_{4A}	S_{4B}
frequency (ns^{-1})	1000	–	–	100	10	1	–	–
w (nm)	2.91 ± 0.05	2.90 ± 0.02	2.85 ± 0.03	2.98 ± 0.04	2.97 ± 0.06	3.05 ± 0.06	2.88 ± 0.02	2.92 ± 0.03
d (nm)	5.16 ± 0.04	5.19 ± 0.06	5.20 ± 0.04	5.23 ± 0.06	5.30 ± 0.06	5.47 ± 0.09	5.24 ± 0.10	5.16 ± 0.11
M_w (kg/mol)	63.0 ± 5	57.6 ± 3.6	59.0 ± 5.2	60.5 ± 5	57.4 ± 2	44.4 ± 1.8	45.0 ± 1.3	45.4 ± 1.8
PDI	2.18 ± 0.19	2.10 ± 0.08	2.12 ± 0.09	2.11 ± 0.16	2.01 ± 0.09	1.90 ± 0.10	1.82 ± 0.05	1.87 ± 0.03
$\langle R_g \rangle$ (nm)	6.44 ± 0.09	7.12 ± 0.15	7.83 ± 0.21	6.34 ± 0.12	5.95 ± 0.15	5.47 ± 0.07	7.04 ± 0.36	7.52 ± 0.17
bridge (%)	77.49	82.59	84.52	75.62	66.15	65.33	80.77	84.75

Table 3.5: Characterization of polyurea systems constructed by curing simulations and sampling molecular weight distributions of curing simulations: (1) Hard domain thickness (w) and inter–domain spacing (d) extracted from RDFs. (2) Weight–average molecular weight (M_w), polydispersity index (PDI) and number–average radius of gyration ($\langle R_g \rangle$). (3) Fraction of bridges in each configuration presented as percentage. The fraction of loops is 100%−bridge%. Uncertainties represent the standard deviations over all systems of each curing case.

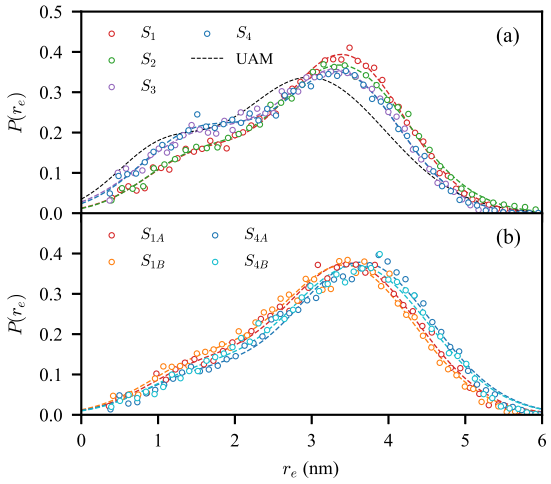

Figure 3.12: Distributions of soft segment end–to–end distance: (a) bonding configurations and (b) sampled configurations. Fits to the data are represented as dashed lines.

The mass–average molecular weight, polydispersity index and radius of gyration of cured polyurea systems are shown in Table 3.5. The polydispersity index is calculated as ratio of mass–average to number–average molecular weight. Higher curing frequencies lead to both increased mass–average molecular weight and increased polydispersity. The number–average radius of gyration is an evidence of larger dimension occupied by molecules from faster cured polyurea systems. The relatively longer chains occupying larger spatial dimension are making up many more hard domains and under higher constraints from hard segments trapped in hard domains in polyurea network, which is able to improve the strength of polymeric materials. The difference in radius of gyration among different bonding rates is correlated with the diffusion effect of prepolymers. As the bonding speed increases, the chain conformation is closer to the one of post-bonded polyurea chains polymerized without

any prepolymer diffusion, where the isonate and diamine molecules are randomly distributed in unit cells. However, as the bonding speed slows down, prepolymer molecules diffuse into fuzzy hard clusters which means the bonding sites essentially interact with local neighbors and, therefore, chains hardly propagate to long–range distance.

Soft segments connect hard domains via different topologies: loop or bridge, which has been shown to affect inelastic deformation mechanisms in polyurea and segmented polyurethanes [36, 43]. However, the fraction of bridge–type or loop–type soft segments in our model systems is difficult to distinguish due to the nearly continuous structure of the hard domains. Therefore, we calculated the distribution of soft segment end–to–end distances (r_e) which is then fitted to a mixture of two normal distributions which describes the populations of loop and bridge soft segments [41]. The distributions of the soft segment end–to–end distances are shown in Figure 3.12a. The mean end–to–end distance of the loop–type soft segments is approximately 1.5 nm and the mean end–to–end distance is about 3.4 nm within bridge–type segments. The fraction of bridge/loop–type soft segments are estimated as the areas under the two respective normal distributions and the corresponding fractions are shown in Table 3.5. At higher curing frequencies, the fraction of bridging soft segments increase. By contrast, the distribution of hard–segment end–to–end distance shows a left skewed bell shape with a single peak located at approximately 2.2 nm for all bonding rates, suggesting that hard–segment conformation is rarely affected by bonding rate. The distributions of end–to–end distance within hard segments are shown in Figure 3.13.

The characterization of microphase separation and molecular conformation of resampled systems mimicking the chain–length distributions within S_1 and S_4 bonding configurations are represented via the same way of commonly cured systems as a

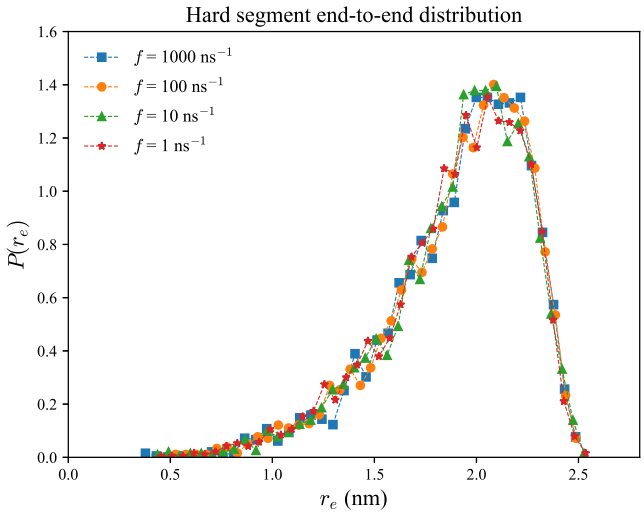

Figure 3.13: End–to–end distance distribution of hard segments within all bonding configurations.

	$f = 1$ ns^{-1}	$f = 10$ ns^{-1}	$f = 100$ ns^{-1}	$f = 1000$ ns^{-1}
A_1	0.357	0.355	0.252	0.231
std_1	0.691	0.773	0.702	0.689
μ_1	1.50	1.50	1.50	1.50
A_2	0.663	0.675	0.768	0.786
std_2	0.769	0.779	0.806	0.802
μ_2	3.38	3.36	3.39	3.41

Table 3.6: Fitting parameters of end–to–end distributions.

comparison. Resulting molecular characterization and phase–related measurement are shown in Table 3.5 under system label S_{1A}, S_{1B}, S_{4A} and S_{4B}. The mass–average molecular weights of sampled systems reveal the correctness of reconstruction process, by which the sampled polyurea systems successfully reproduce the average molecular weight as well as the polydispersity indexes of corresponding polymerized polyurea systems, i.e., S_1 and S_4. However, it is worth noting that the radius of gyration is much higher than the one of corresponding cured systems, which is correlated with the initial coordinates of super–atoms. The phase–segregation morphology is also analyzed by RDFs of hard–segment super–atoms, shown in Figure **??**. Even though the average molecular weights of sampled systems are really close to the situation in corresponding curing case, the difference in M_w between S_{*A} and S_{*B} does not differ the morphology from each other. The mean hard–domain thickness and inter–domain spacing of sampling configurations are all approximately 2.9 nm and 5.2 nm, respectively. As shown by end–to–end distribution of soft segments in Figure 3.12b and fraction of bridges in Table 3.5, the soft–segment conformation is mostly made up of bridge–type connection. The segmental conformation is highly correlated with chain conformation measured as radius of gyration: as the molecules spread within large spatial dimension rather than curl up in a finite entity, it is more possible for the chains to link various hard domains rather than repeatly connect one or two hard domains. Both radius of gyration and soft–segment behavior are revealing that the hard domains in reconstructed polyurea network are highly inter–connected by soft segments.

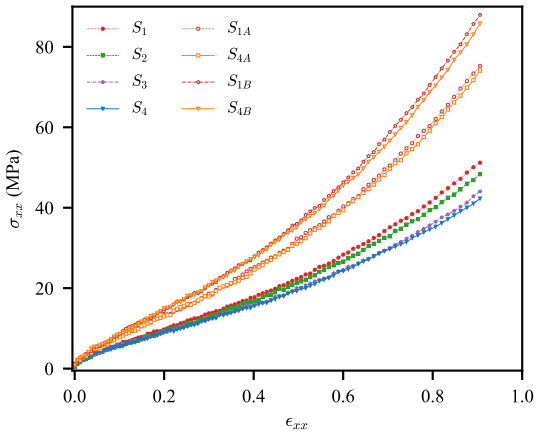

Figure 3.15: True stress–true strain behavior of the model systems under uniaxial compressive stress loading.

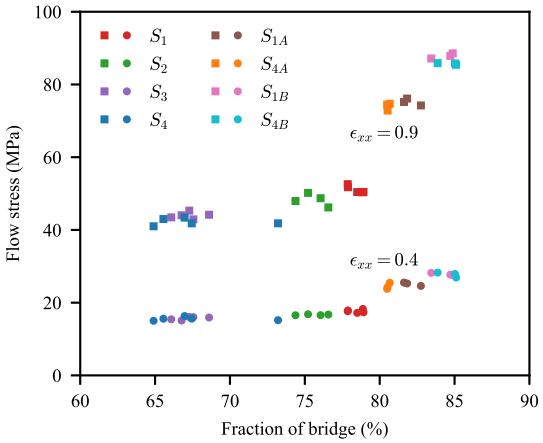

Figure 3.16: Fraction of bridges versus flow stress.

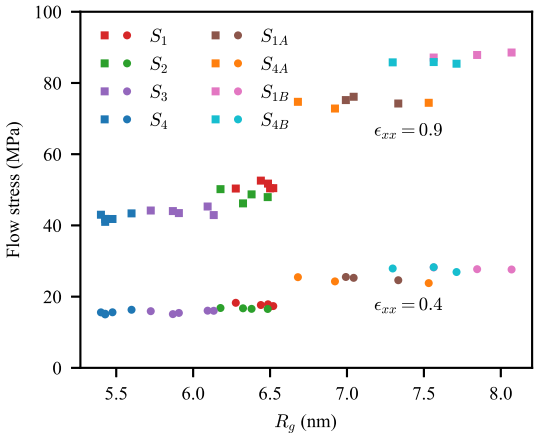

Figure 3.17: Mean radius of gyration versus flow stress.

3.3.3 Mechanical Behavior

During the uniaxial compression of the cured and sampled model systems, the six independent components of atomic virial stresses were calculated. Under the uniaxial stress conditions, the shear stresses oscillate about zero and the normal stresses in the transverse directions, i.e., σ_{yy} and σ_{zz}, oscillate about 1 atm. The compressive stress response in the loading direction, i.e., σ_{xx}, is shown in Figure 3.15 for all the sets of model systems. The stress behavior can be broken down into three strain regimes, which qualitatively agree well with experimental observations [26, 33]. At low strains ($0 < \epsilon_{xx} < 0.04$), stresses behave as linear elastic regime until a yielding point appears at about true strain $\epsilon_{xx} = 0.04$ with a yielding stress of around $\sigma_{xx} = 4$ MPa. At intermediate strains ($0.04 < \epsilon_{xx} < 0.3$), the response softens, and at strains larger than 0.3, the responses deviate within different bonding configurations at large strains: the ultimate compressive strength at true strain $\epsilon_{xx} = 0.9$ increases as faster reaction speed in bonding simulations. In addition, the strengths of sampled configurations are much higher than the one of model polyurea polymerized from small prepolymers, even though the molecular weights and polydispersity of the sampled polyurea network are similar to the corresponding polymerization results. With similar results of microphase separation and polymerization degree in polymerized and sampled systems, the difference in stress response is potentially induced from chain and segmental conformation, represented as substantial difference in radius of gyration and fraction of bridge/loop.

Figure 3.16 and Figure 3.17 display the flow stress measured at true strain of $\epsilon_{xx} = 0.4$ and 0.9 as a function of fraction of bridges and radius of gyration, respectively. From figure 3.16, clearly positive trend between amount of bridges and stress response

is observed especially under large strain, suggesting a nonlinear relationship between strength and fraction of bridge. With small amount of bridge–type soft segments ($< 70\%$), flow stress at $\epsilon_{xx} = 0.4$ are not substantially affected by bridge fraction, whereas the flow stress slightly increase with larger amount of bridges at $\epsilon_{xx} = 0.9$. With large amount of bridge–type soft segments, the flow stress increases faster with increasing bridge amount representing the similar behavior as shown in [43] by tensile testing and the behavior of bridge–type soft segments supporting hard domains are more obvious at large deformation due to fully stretching state of soft segments at large strain. Additionally, figure 3.17 represents the flow stress of model polyurea is also highly correlated with the radius of gyration: high radius of gyration leads to higher flow stress. Because larger dimension of molecular chains provides higher probability to be involved in inter–domain interactions between hard domains in polyurea or crystalline phases in semicrystalline polymers. And these chains linking many hard domains are under more constraints from intermolecular and inter–domain entanglements in phase–segregated copolymers, which reinforces the behaviors of bridge–type soft segments during deformation as shown in [43], i.e., a polyurea chain connecting many hard domains by some amount of bridge–type soft segments tends to make more contribution to strength than a chain connecting two hard domains by same amount of bridges.

To represent the rate–dependent behavior of polyurea by current coarse–grained model, the flow stresses of S_1 and S_4 at true strain of $\epsilon_{xx} = 0.4$ and 0.9 as a function of several strain rates are in shown Figure 3.18 on a logarithmic scale. The experimental values from [22] measured by compression test with strain rates up to 10^4 s^{-1} are also shown in the figure. For polymerized polyurea networks from curing simulations, the stress values show qualitatively similar rate–dependent behaviors within strain

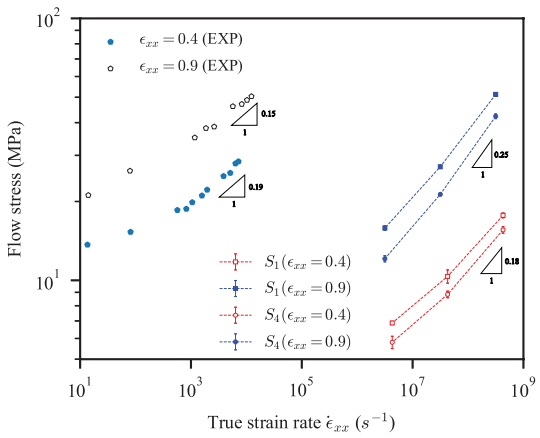

Figure 3.18: Flow stresses at selected true strain from uniaxial compression on S_1 and S_4 cases versus true strain rate shown in log–log scale.

rates ranging from 10^6 to 10^9 s^{-1}. The stresses at strain of 0.9 behave slightly higher linear rate–dependency in log–log scale than the stresses at strain of 0.4 as shown by higher stress value increase between 10^8 and 10^9 s^{-1} than the one between 10^7 and 10^8 s^{-1}. The rate–dependent stress behavior of current model polyurea network agrees well with experimental result. However, it is evident that the relative lower stress magnitudes from coarse–grained simulations are not obviously inferred from low strain–rate experiments due to the fast diffusion and smooth energy surface of coarse–grained model.

Figure 3.19 shows the distributions of soft–segment end–to–end distance after uniaxial compression within all configurations. For bonding cases in Figure 3.19a, the locations of peak values representing loop–type soft segments stay as the same as the one before deformation. However, comparing with the initial distributions, the locations of the second peak increase by 34% and the bell shapes are broaden by deformation, which suggests the bridge–type soft segments are stretched in the

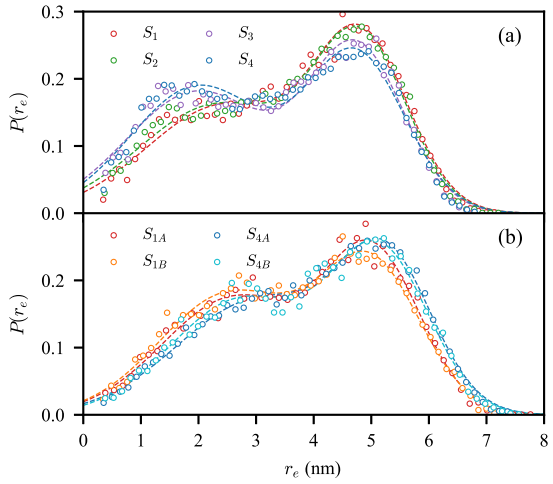

Figure 3.19: Distributions of soft segment end–to–end distance at $\epsilon_{xx} = 0.9$: (a) bonding configurations and (b) sampled configurations. Fits to the data are represented as dashed lines.

transverse plane. The stretched segments constrain the movement of the hard domains in the transverse plane contributing to the material strength. As shown in Figure 3.19b, sampled systems behave differently with polymerized polyurea systems, both types of soft segments as characterized by loop and bridge–type segments are under strongly tensile loading and the average end–to–end distance substantially moves to larger values. According to the change of soft–segment end–to–end distributions, polymerized systems and sampled systems of coarse–grained polyurea in this work are showing substantially different mechanical mechanisms under uniaxial compressive deformation. For polymerized polyurea, the conformation of loop–type soft segments has not been changed by deformation, whereas the bridge–type soft segments are obviously stretched. For sampled polyurea, both loop–type and bridge–type soft segments behave with tensile phenomenon. The difference of conformational change within polymerized

and sampled systems indicates that, in addition to segmental topology, chain or segmental conformation plays a greatly important role in deformation mechanisms under compressive loading especially in co-continuous structures, which is hardly observed in lamellar stack model of self–assembled copolymers [43].

3.4 Summary

In this section, we developed a reactive coarse–grained model for polyurea elastomers, the force fields of which were calibrated through matching structural features sampled from atomistic partially–polymerized polyurea systems. With the coarse–grained model, we are able to perform polymerization simulations to generate polyurea systems close to real polyurea network with a consideration of prepolymer diffusion and study the effect of polymerization on microstructures and mechanical properties. The polymerization conditions were varied by different chemical reaction speeds over four decades of time scales which leads to polyurea systems with various morphologies, polymerization degrees, segmental and chain conformations. Additional polyurea systems were generated by sampling the molecular weight distributions of polymerized polyurea and random walk equilibrium instead of polymerzation simulations.

As a result, the microphase separation of polyurea was quantitatively studied via RDFs of super–atoms within hard segments indicating that slower reaction speed provides hard domains with larger domain thickness and inter–domain spacing. And faster reaction leads to higher polymerization degree, i.e., larger mass–average molecular weight, and higher degree of polydispersity in molecular weight. For chain conformation, the chains that polymerized at a faster rate tended to have a larger radius of gyration, and therefore, on average, form bridges across a larger number of

hard domains. During uniaxial compression, the strain–stress curve of coarse–grained model shows power–law relationship within strain rates over three decades under compression. And with probabilistic characterization of segmental behaviors, the compressive strength of polyurea network is substantially affected by segmental topologies, i.e., relative fraction of bridge–type and loop–type soft segments. Higher fraction of bridge–type soft segments leads to higher compressive strength especially at large deformation when bridges are fully stretched between hard domains. In addition, compressive strength also shows positive dependence on chain conformation as revealed by radius of gyration and flow stress at different strains. The behavior of end–to–end distance within hard segments during deformation indicates the compressive strength is mainly contributed by deformation of hard domains which shows highly correlation with chain and segmental conformations.

The coarse–grained model is able to perform wide range of chain conformations compared with segmental length. The result in our work indicates that the compressive strength is highly dependent on spatial arrangement of polyurea chains in addition to topology of soft segments. The positive dependence of compressive strength on radius of gyration suggests that a polyurea chain comprised of similar amount of bridge connections may have different effects on deformation mechanism, i.e., a chain connecting many hard domains attempt to make more contribution to strength than connecting same two hard domains in a back and forth regime. However, the co–continuous structure of hard domains and the way of generating polyurea networks in this work place much difficulty to quantatively control the fraction of bridges or chain conformation. Even though, the current study provides essential insights of deformation mechanism affected by both segmental and chain behaviors in polyurea networks.

Chapter 4

MULTIRESOLUTION COARSE–GRAINED MODELING FOR STRUCTURE–PROPERTY RELATIONSHIP OF POLYUREA

4.1 Introduction

The dynamic properties of polymer depend on a wide range of temporal and spatial scales, thus modeling the dynamics of polymer at atomistic scale is inherently challenging [35]. Since the classical atomistic simulation is overwhelmed to probe the diffusive and segmental dynamics in entangled polymer, coarse–grained molecular models, which reduce the computational cost by pruning the degrees of freedom, have been developed to unearth the relationship between microscopic structures and macroscopic properties in mesoscale. Due to the simplified geometric information, the effectiveness of coarse–graining process is essentially dependent on capturing critical target properties derived from atomistic scale. Therefore, researchers have been focusing on the procedure of developing coarse–grained models, including training effective force fields [90, 91], choosing appropriate mapping scheme [92–94] and scaling the dynamics accelerated by smoothed free energy [95, 96], to retain as much atomistic characteristics as possible.

On the other hand, the insight at atomistic scale is also required in many cases. For instance, to investigate a strain–stress relationship that is comparative to experimental measurement, we usually have to scale the computational result to make the accelerated dynamics match experimental values. However, the heterogeneous microstructure of polyurea or other block copolymers poses difficulties to linearly handle the dynamic

relationship between atomistic and coarse–grained scales. In addition, the mechanical behaviors of polyurea, such as viscoelastisity and shear strength, are highly dependent on the hydrogen bonding which is usually omitted in low–resolution models. Therefore, it would be beneficial to transform the CG representation back to atomistic scale.

In this section, we proposed a hierarchical backmapping framework starting from the reactive coarse–grained model to the atomistic scale, which is able to retain the microstructural features, including phase–segregated morphology and crosslinking, constructed from polymerization simulations. We firstly developed an intermediate coarse–grained model for polyurea to fill the gap between the high–resolution united–atom–like model in Chapter 2 and the bead–spring polymerization model as described in Chapter 3. Then three cycles of fragments insertion and energy minimization can be performed to effectively and efficiently transform a model system constructed via polymerization simulation into a full–scale system. Taking advantage of the multiresolution coarse–grained models developed in this work, we are also able to investigate the segmental dynamics and relaxation times in different time scales and study the dependence of coarse–graining degree and temperatures.

4.2 Model and Methodology

4.2.1 Multiresolution Coarse–Grained Modeling

The coarse–grained models at various resolutions are denoted as CG_0, CG_1 and CG_2 with increasing degree of coarse–graining, among which CG_0 is the united–atom–like model as described in Chapter 2, CG_2 is the bead–spring model as described in Chapter 3 and CG_1 is an intermediate model bridging the former two coarse–graning

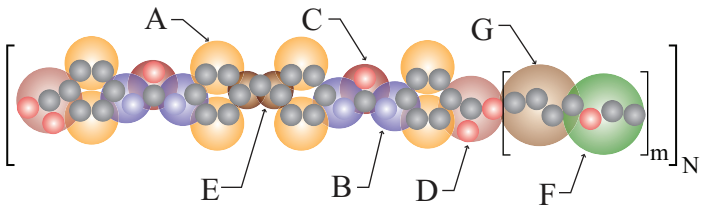

Molecular Weight (g/mol): A: 26, B: 27, C:28, D: 56
E: 19, F: 28, G: 42

Figure 4.1: Coarse–grained mapping scheme of the intermediate CG model.

scales. The mapping scheme of the intermediate coarse–grained model introduced in this work is shown in Figure 4.1. The number of degree of freedom within CG_0, CG_1 and CG_2 was reduced by an approximate factor of two from a high–resolution model to the next low–resolution one.

The effective force field of each coarse–grained model was calibrated by the iterative Boltzmann inversion (IBI) method:

$$V_{i+1} = V_i + \alpha k_B T \ln\left(\frac{P_i}{P^*}\right), \tag{4.1}$$

where P_i are the structural distributions sampled from coarse–grained MD simulations using potentials V_i at iteration i, P^* are the corresponding target structural distributions computed from atomistic systems using the corresponding CG sites, k_B and T are Boltzmann coefficient and temperature. Parameter α is a scaling factor to dampen the potential update and improve the stability of optimization. The initial guess of effective potentials to start the IBI algorithm are estimated by Boltzmann

inversion:

$$V_0(l) = -k_B T \ln\left(\frac{P^*(l)}{l^2}\right) \tag{4.2}$$

$$V_0(\theta) = -k_B T \ln\left(\frac{P^*(\theta)}{\sin(\theta)}\right) \tag{4.3}$$

$$V_0(\phi) = -k_B T \ln\left(P^*(\phi)\right) \tag{4.4}$$

$$V_0(\chi) = -k_B T \ln\left(P^*(\chi)\right) \tag{4.5}$$

$$V_0(r) = -k_B T \ln\left(g^*(r)\right), \tag{4.6}$$

where $P^*(l)$, $P^*(\theta)$, $P^*(\phi)$, $P^*(\chi)$ and $g^*(r)$ are the target bond, angle, dihedral angle, improper angle and RDF distributions sampled from atomistic simulations. As the divergence between target distributions and coarse–grained distributions approaches a negligible value, the coarse–grained force field becomes representative of local structures in the atomistic scale. The evaluation of optimization performance is described in [41].

The coarse–grained models are implemented by the most representative effective potentials for describing the structural features in corresponding resolution. As the resolution decreases, dihedral and improper angles are not able to represent the segment stiffness which is usually implicitly performed in bond angle potentials. More specifically, the bond stretching, angle bending and non–bonded pair potentials are implemented in all coarse–grained models, while dihedral and improper angle potentials are omitted in CG_1 and CG_2 models. The bond potentials in all coarse–grained models and angle potentials in CG_0 and CG_1 are performed by harmonic functions, whereas the rest effective potentials, including non–bonded pair potentials, dihedral angles in CG_0, and angle potentials in CG_2, are represented as numerical tables. The implementation of effective potentials in each coarse–grained model are summarized in Table 4.1.

CG_λ	bond	angle	dihedral	improper	pair
CG_0	harmonic	harmonic	table	table	table
CG_1	harmonic	harmonic	–	–	table
CG_2	harmonic	table	–	–	table

Table 4.1: Summary of effective potentials implemented in each coarse–grained model.

To sample the target structural distributions according to corresponding CG sites of each coarse–grained model, fifteen atomistic systems were generated and the atoms of each are randomly placed in a periodic simulation cell. Each simulation cell contains twenty single–block oligomeric polyurea molecules. To equilibrate the simulation cells, the atomistic systems were first relaxed in the isothermal–isobaric (NPT) ensemble over a duration of 8 ns with $T = 500$ K and $p = 1$ atm. Following the equilibrium at elevated temperature, the temperature decreases to $T = 300$ K over a duration of 8 ns, and then the systems were further equilibrated for 16 ns at $T = 300$ K and $p = 1$ atm. Following above equilibration, a 1 ns duration canonical (NVT) ensemble simulation was performed to sample the atomistic trajectories. Then, the atomistic coordinates are mapped to corresponding CG sites, from which RDF, bond length, bond angle, dihedral angle, and improper angle distributions are computed. The first– and second–bonded neighbors of each super–atom are excluded for CG_0 and CG_1 while only the first–bonded neighbors are omitted for CG_2 while computing the target RDFs. The timestep of running atomistic simulations was 1 fs. In this work, the molecular dynamics simulations are performed using the Condensed–phase Optimized Molecular Potentials for Atomistic Simulations Studies (COMPASS) force fields [60, 61], where long–range Coulombic interactions are calculated using the

particle–particle/particle–mesh (PPPM) method in the LAMMPS kspace package [83]. The cut–off distances of Lennard–Jones interactions and short–range Coulombic term are set to be 9.5 Å.

4.2.2 Hierarchical Reverse Mapping

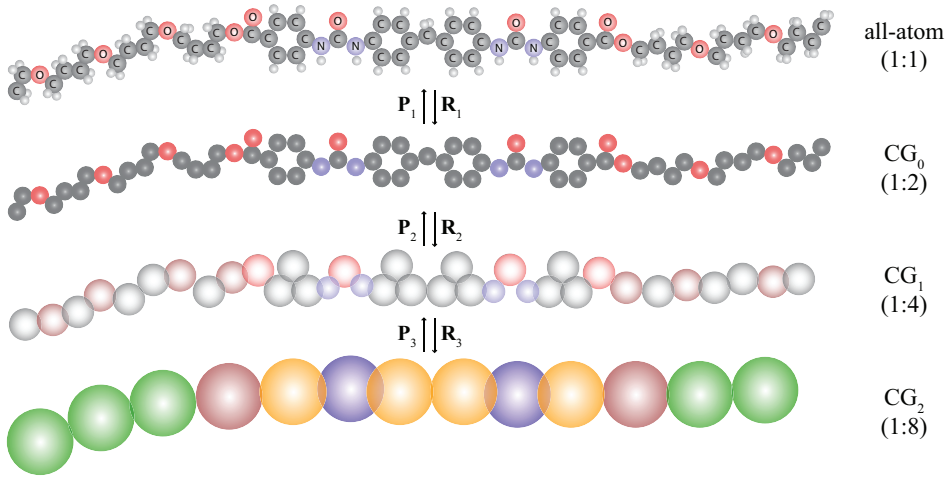

Figure 4.2: Multiresolution coarse–graining and hierarchical backmapping workflow of polyurea.

To construct atomistic molecular systems with microstructural morphology and molecular conformation that are close to real polyurea network, we incrementally transformed the coarse–grained models back to atomistic scale in a top–down regime retaining the microstructural features calibrated in long time scale: $CG_2 \rightarrow CG_1 \rightarrow CG_0 \rightarrow$ atomistic. Figure 4.2 shows a schematic configuration of the workflow.

We firstly generated a prepolymer system with isocyanate and amine molecules in CG_2 scale and performed a polymerization simulation to develop a polydisperse and phase–segregated polyurea network. To validate the workflow, we firstly picked one

CG_λ	timestep (fs)	number of super–atom types
AA	1	11
CG_0	2	9
CG_1	4	7
CG_2	5	5 (7)

Table 4.2: Summary of polyurea model systems.

of the model systems constructed with the fastest bonding speed in Chapter 3 and characterized the system via some typical static properties. Then, to compensate the computational effort required by high–resolution models, the second model system for the rest simulations and analysis in this chapter was initialized with 1/4 composition of the one in Chapter 3 and polymerized by the same bonding condition. The CG_2 polyurea model systems constructed by polymerization simulations were then transformed back to the intermediate model CG_1 followed by a short–time equilibrium. After the equilibrium, the CG_1 systems were mapped back to the CG_0 scale. Finally, following an equilibrium and backmapping operation from CG_0 to atomistic scale, the polyurea model systems in full scale were generated. After each backmapping, a two–stage equilibrium of 0.5 ps NVT/limit at $T = 300$ K followed by 10 ps NPT ensemble at $T = 300$ K and $p = 1$ atm is performed to relax the local potential energy. With the equilibrium, the total potential energy goes down and reaches a plateau when the relaxation is done. Table 4.2 shows a summary of timesteps and number of super–atom types within multiresolution models. The CG_2 system for analyzing dynamics was generated with 20k super-atoms and the atomistic system was constructed with 231k atoms and box length is approximately 134 Å after backmapping.

4.2.3 Multiresolution Simulations

Once we have the multiresolution coarse–grained model systems generated by the step–wise backmapping procedure, we performed several molecular dynamics simulations to evaluate the dynamics of polyurea. We firstly performed equilibrium simulations through constant volume and temperature $T = 300$ K, by which to characterize the acceleration of coarse–grained diffusion comparing with the one of atomistic model. Then, an extra set of simulations are relaxation process after a step–wise strain deformation. The step–wise strain deformation was performed by NPT ensemble, in which the model systems were stretched to $\lambda = 1.5$ along x–axis in 10 ps with a constant engineering strain rate. The deformation was followed by a relaxation scheme, in which the two ends of the simulation box along the loading direction were fixed. Both the tensile deformation and relaxation simulations were established as uniaxial stress state, in which the lateral pressures, i.e., σ_{yy} and σ_{zz}, were maintained as $p = 1$ atm by using anisotropic barostat in NPT ensemble. For different coarse–grained and atomistic models, the relaxation simulations were performed at $T = 300$ K. And two extra simulations were set up on the atomistic model with elevated temperatures of $T = 345$ and 380 K. The damping parameters for temperature and pressure during relaxation were $100\times\Delta t$ and $1000\times\Delta t$, respectively, for different models.

4.2.4 Characterization

In this chapter, we probe the dynamics of multiresolution models by calculating mean squared displacement (MSD), correlation of soft–segment end–to–end vector and slip vector under various conditions. To characterize the diffusion in different

models, we calculated the MSD during equilibrium simulations by:

$$MSD(t) = \langle |\mathbf{x}(t) - \mathbf{x}(0)|^2 \rangle, \tag{4.7}$$

where $\mathbf{x}(t)$ is the center of mass of each segment at time t.

For the relaxation simulation, the correlation of end–to–end vector of soft segments was monitored to characterize the segmental dynamics during relaxation:

$$C_{ee}(t) = \langle r_e(t) \cdot r_e(0) \rangle, \tag{4.8}$$

where $r_e(t)$ is the end–to–end unit vector of soft segments at time t.

We assume the resulting correlation functions of relaxation can be represented by exponential decay. Therefore, we characterize the time scales via fitting the correlation functions by exponential functions:

$$f(t) = A \exp\left[-\left(\frac{t}{\tau} \right) \right], \tag{4.9}$$

where A is amplitude, τ is the relaxation time. Since the conformational relaxation can be broken into several relaxation processes and time scales, a correlation function can be represented by a biexponential function as:

$$F(t) = \sum_{i}^{k=2} A_i \exp\left[-\left(\frac{t}{\tau_i} \right) \right], \tag{4.10}$$

where A_i and τ_i are the corresponding parameters tending to describe each relaxation process.

In addition to segmental dynamics, we probe the local dynamics using slip vector ($\mathbf{s}_i$) to represent the maximum relative displacement of (super–)atom i with respect to its neighbor j [36]:

$$\mathbf{s}_i = \max\left(\mathbf{x}_{ij} - \mathbf{X}_{ij} \right), \tag{4.11}$$

where $\mathbf{x}_{ij}$ and $\mathbf{X}_{ij}$ are the distance vector between super–atom i and j at current and reference configurations, respectively. The slip vector is originally a measurement to evaluate the relative sliding in crystal lattice structure [97–99]. In this work, we apply the slip vector with distance–based neighbor list to estimate the local dynamics which is a key metric of local relaxation. To compute the slip vector, we consistently collect the neighbors for each (super–)atom within a cut–off distance of 5.0 Å which is approximately the leading zero distance of RDFs sampled from CG_2 systems.

4.3 Results and Discussion

4.3.1 Model Validation

The force fields of the intermediate coarse–grained model, i.e., CG_1, were calibrated by 10 steps of IBI optimization, at which iteration the representation error satisfied the statistics–based convergence criterion as mentioned in Chapter 2 and Chapter 3. The potential coefficients for bond stretching and bond bending interactions are shown in Table 4.3. The target (atomistic) and resulting (coarse–grained) structural distributions corresponding to CG_1 mapping scheme at the final iteration of optimization are shown in Figure 4.3, Figure 4.4 and Figure 4.5. For RDFs, the representation error measuring the difference between coarse–grained and atomistic distributions is less than 6% at the final step of iteration. However, since the bond stretching and bond bending potentials are implemented by harmonic functions while some target distributions do not follow a perfectly bell–shape distribution, minor deviation appears in some of the structural distributions between target and coarse–grained model.

bond type	l_0 **(Å)**	K **(kcal/mol/Å^2)**
$F-G$	2.613	11.38
$D-G$	3.611	5.377
$A-D$	3.139	118.1
$A-B$	3.055	105.4
$B-C$	1.371	394.8
$A-E$	1.859	290.5
$E-E$	2.528	57.28
angle type	θ_0 **(deg)**	K **(kcal/mol/rad^2)**
$G-F-G$	142.0	3.567
$F-G-F$	163.0	2.136
$D-G-F$	148.9	1.167
$A-D-G$	131.2	3.303
$B-A-D$	137.1	119.3
$A-B-C$	131.8	8.071
$B-C-B$	117.2	113.4
$B-A-E$	120.1	145.1
$A-E-E$	148.9	5.115
$A-D-A$	45.81	653.0
$A-B-A$	46.26	563.9
$A-E-A$	83.34	186.5

Table 4.3: Harmonic bond and angle coefficients for the CG_1 model of polyurea in the format consistent with the harmonic bond and angle styles in LAMMPS.

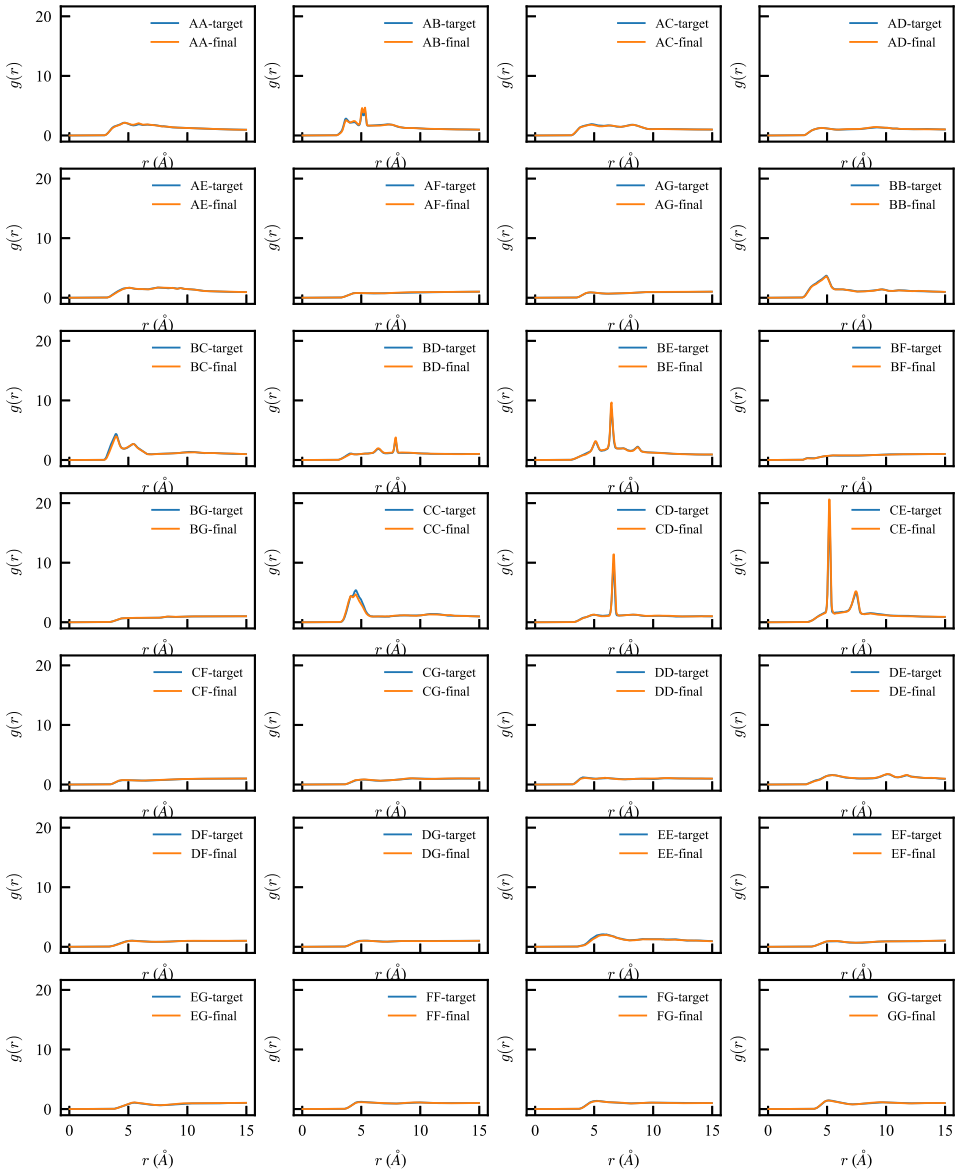

Figure 4.3: The target and CG_1 RDFs of all pairwise interactions at the final iteration of IBI optimization.

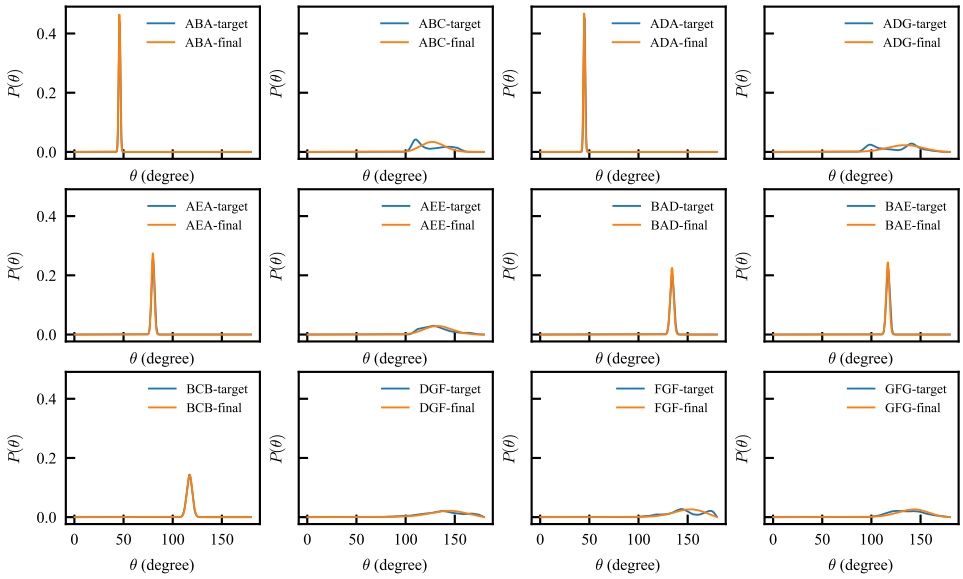

Figure 4.4: The target and CG_1 ADFs of all bond bending interactions at the final iteration of IBI optimization.

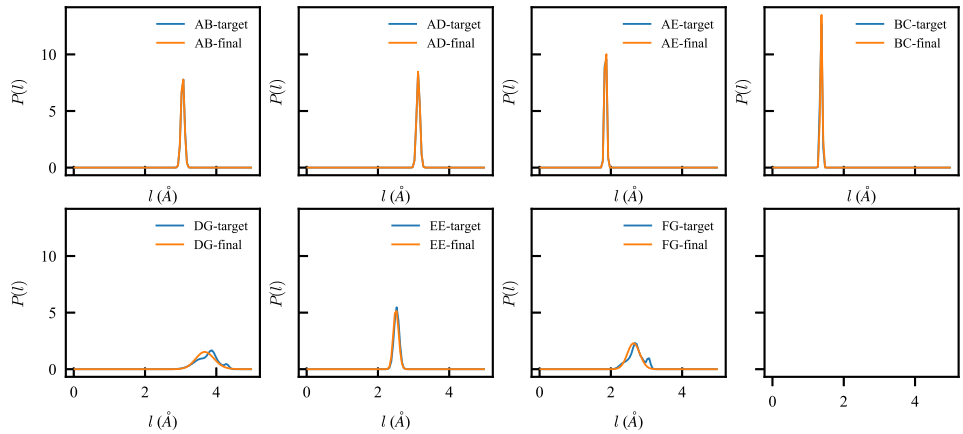

Figure 4.5: The target and CG_1 BDFs of all bond stretching interactions at the final iteration of IBI optimization.

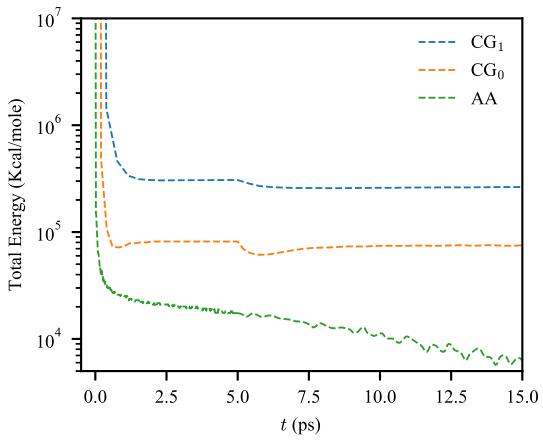

Figure 4.6: Energy histories of equilibrating CG models.

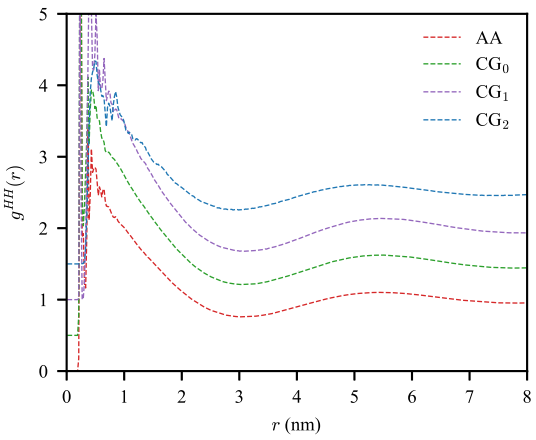

Figure 4.7: RDFs of hard super–atoms within CG models.

The polymerization simulation performed by CG_2 model was running for 200 ns, by when the chemical conversion is 100%. The polymerized polyurea CG_2 system is composed by approximately 80k super–atoms in a cubic cell with a box length of 20.4 nm. By backmapping this CG_2 system through the regime described in Section 4.2.2, we obtained an atomistic polyurea system and the intermediate CG model systems with statistically equivalent network. Figure 4.6 shows the total energy, i.e., kinetic energy and potential energy, histories during the equilibrium after backmapping operations corresponding to multiresolution coarse–grained models. Every step of backmapping generates locally high energy regions, however, the energies rapidly decrease several decades in 1 ps and reach plateau values within an equilibrium of 15 ps, suggesting the capacity of the hierarchical reverse–mapping scheme introduced in this chapter.

Figure 4.8 shows a snapshot of model systems corresponding to different resolutions. The color schemes of super–atoms in different models are designed to be similar coloring

CG_λ	$\langle R_g \rangle$ (nm)	$\langle R_{ee} \rangle$ (nm)	$\langle R_e^s \rangle$ (nm)	f_{bridge} (%)
CG_2	6.49	14.4	2.68	78.94
CG_1	6.63	14.7	2.99	80.91
CG_0	6.53	14.4	3.09	79.07
AA	6.53	14.5	3.05	80.71

Table 4.4: Summary of static properties from multiresolution coarse–grained model systems.

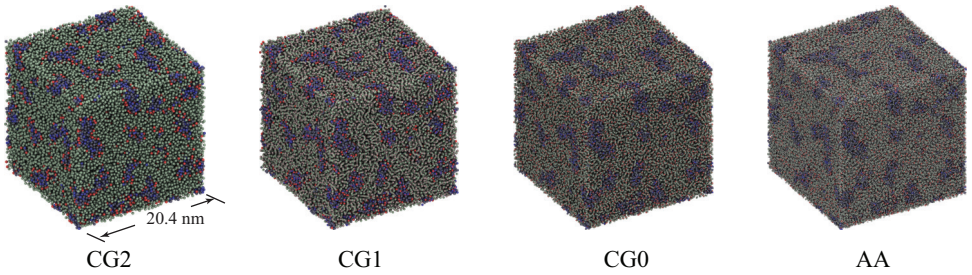

Figure 4.8: VMD plot of multiresolution CG models.

styles. The morphology of various model systems are consistently representing the microphase separation of hard domains embedded in soft domains. And according to the RDFs of hard–type super–atoms displayed in Figure 4.7, the hard–domain thickness and inter–domain spacing in CG_2 are approximately 3.0 nm and 5.2 nm which are both slightly smaller than the other CG model systems with 3.1 nm and 5.5 nm. The deviation of the characteristic lengths of hard domains between CG_2 with other models is due to the replacement of the functional A^+ and U^- by A and U super–atoms, respectively, when transforming CG_2 to CG_1 for convenience.

To validate that the multiresolution model systems are containing equivalent network characteristics, some static properties of each model system are calculated, shown in Table 4.4. The chain conformation characterized by radius of gyration, mean end–to–end distance, mean end–to–end distance of soft segments and corresponding

fraction of bridge–type soft segments is consistent within coarse–grained systems at different resolutions. Slight discrepancy can also be seen between CG_2 with other models due to the simplification of super–atom types. However, this discrepancy does not lead to significant variation in fraction of bridge–type soft segments among different models.

4.3.2 Mean Squared Displacement

During the NVT equilibrium simulations using the multiresolution models, we calculated the mean squared displacement (MSD) of the center of mass within each segment based on Equation (4.7) to probe the segmental diffusion of each model system. Figure 4.9 shows the MSD of each model ensemble–averaged over the whole system or hard and soft segments separately. In Figure 4.9a, the diffusion of each coarse–grained model is consistently faster than the one of atomistic model and the diffusive rate increases with increasing coarse–graining degree. However, the increment

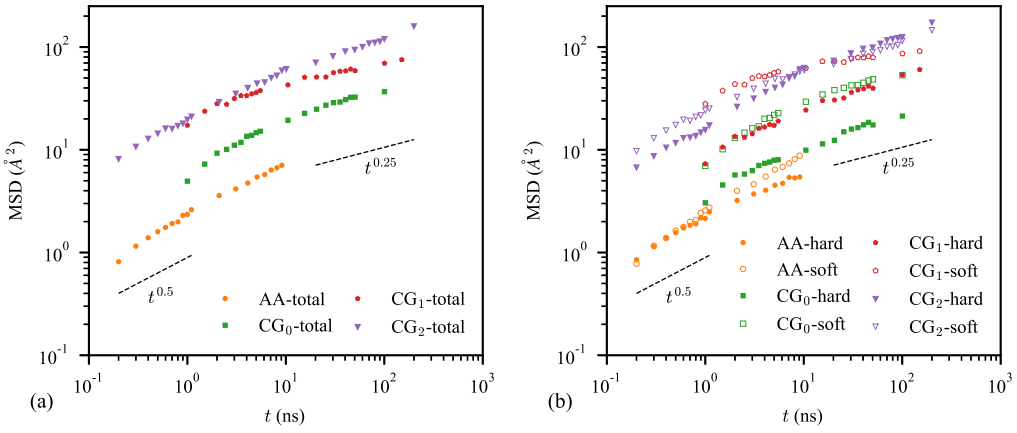

Figure 4.9: MSD of multiresolution models during NVT simulations.

between each pair of coarse–grained models is not homogeneous. In the first 2 ns, the MSD of CG_1 is close to that of CG_2 and after which the slope of CG_1 MSD decreases with time. According to [44], this heterogeneous behavior within multiresolution models suggests the critical degree of coarse–graining. In addition, the initial slope of MSD does not follow the one derived from Rouse model, i.e., $\sim t^1$ [100], suggesting that the segments are under constraint and not moving to segmental dimension. And Figure 4.9b shows the MSD averaged over hard and soft segments, respectively, representing the difference of segmental mobility between hard and soft phases. It is clearly to see the MSD of each model system is dominated by the behavior of soft segments and the MSD of center of mass of hard segments mostly linearly increase in log–log space within the time scale of multiresolution simulations. In atomistic model, the MSD of soft segments and hard segments overlap in the first 1 ns of simulation indicating the glassy behavior of soft phase in short time scale, after which the soft segments display higher mobility compared with hard segments suggesting rubbery behavior. And this gap between the MSD of hard and soft segments is more significant in CG_0 and CG_1, but being broken in CG_2, in which model the hard segments become even more mobile than soft segments after 10 ns.

4.3.3 Relaxation Process

In order to evaluate the temperature–dependence of segmental dynamics and the relationship with coarse–graining degree, we simulate the relaxation process by atomistic and coarse–grained models and monitor various metrics, including correlation of end–to–end vectors among soft segments and slip vector, in different time ranges. The correlations of soft–segment end–to–end vectors are calculated by Equation (4.8)

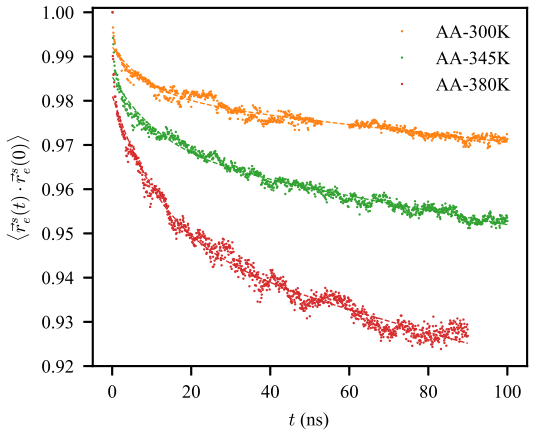

Figure 4.10: End–to–end correlation of soft segments in atomistic systems.

and illustrated in Figure 4.10 and Figure 4.11. The data points are fitted by a bi–exponential function as shown by Equation (4.10) and the fitting parameters representing the two characteristic time scales of segmental dynamics are displayed in Table 4.5.

The correlations of soft end–to–end vectors obtained by atomistic simulations within 100 ns in terms of different temperatures are shown in Figure 4.10. The empty circles are data points queried from simulations with a time interval of 10 ps and the dashed curves are the best fitting on each group of data points by Equation (4.10). The correlation of $\boldsymbol{r}_e$ of soft segments rapidly decays in the first 10 ns followed by a relatively slower relaxation process. At different temperatures, the long–term relaxation times are shortened by higher temperature of simulations suggesting that higher kinetic energy accelerates the segmental dynamics of soft segments. The long–term characteristic time at 300 K is approximately 2.58 times of the characteristic time at 380 K. This long–term relaxation time is on the same order of the one that was previously observed in the dielectric spectrum of PTMO–based polyurea [101] and

T (K)	τ_1 (ns)	A_1	τ_2 (ns)	A_2
300	9824.5	0.981	9.78	0.0117
345	5998.0	0.968	12.39	0.0174
380	3806.4	0.947	13.01	0.0340
CG_λ	τ_1 (ns)	A_1	τ_2 (ns)	A_2
CG_0	13763.7	0.955	17.59	0.0303
CG_1	8113.9	0.894	9.89	0.0578
CG_2	2938.5	0.636	84.69	0.2160

Table 4.5: Fitting parameters of soft–segment end–to–end correlation in different model systems and temperatures.

has been attributed to the α relaxation process representing the segmental motion in soft phase. In contrast to the long–term relaxation, the temperature dependence of short–term relaxation behaves in a way opposing to long–term relaxation, i.e., higher temperature provides longer characteristic time scales. However during our simulations, the relaxation process is dominated by the slow process of relaxation.

A (ns)	T_0 (K)	B (K)
1.66×10^6	812.8	2630.3

Table 4.6: Fitting parameters of Vogel–Tammann–Fulcher equation.

The temperature dependence of the characteristic time was fitted by Vogel–Tammann–Fulcher (VTF) equation which is a widely used function to describe the temperature–dependent characteristic time of dynamics in glass–forming liquid [102–

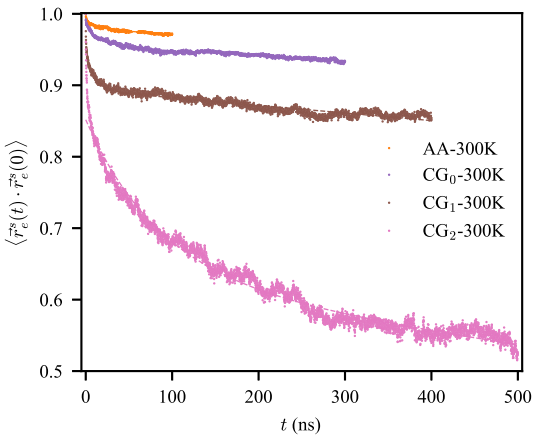

Figure 4.11: End–to–end correlation of soft segments in CG systems.

104]:

$$\tau = \tau_0 \exp\left(\frac{B}{T - T_0}\right), \tag{4.12}$$

where τ_0, B and T_0 (Vogel temperature) are fitting parameters which are shown in Table 4.6. It is worth noting that the long–term relaxation times at the order of $\sim 10^{-6}$ s agree well with the α relaxation in soft domain as shown in [101]. However, the segmental motion of the soft segments is also constrained by the mobility of hard domains suggesting that the relaxation time obtained from this calculation is also partially attributed to the hard phase. This intermediate phase chemically belong to soft segments while its relaxation dynamics distinctly differ from soft domains as previously observed from dielectric spectroscopy [11, 13, 105] and DMA [106] on polyurea systems.

To bridge the dynamic time scales in different coarse–grained models, the relaxation simulations were also performed by CG systems with different coarse–graining degrees. The relaxation simulations by different coarse–grained models were performed for simulation time ranging from 100 ns to 500 ns. Even though much longer simulation

time, such as up to $\sim \mu s$, for coarse–grained models, especially for CG_1 and CG_2, is able to be achieved readily, the dynamics in above models can be easily differed and, therefore, current simulation time is long enough to study the relationship between different models. As shown in Figure 4.11, the relaxations in different coarse–grained models can also be represented by bi–exponential functions suggesting two characteristic times. The soft segments in the CG_2 model move significantly faster than the other models. By contrast, compared to the atomistic model, CG_0 and CG_1 decay with similar speed in long–term time range, whereas the short–term relaxation is faster in terms of higher degree of coarse–graining.

According to [11, 13, 105], two relaxation processes of soft segments were observed in PTMO–based polyurea by dielectric spectroscopy which are referred as α and α' relaxations. The α' relaxation with relatively low relaxation frequency is associated with the local dynamics of the soft region attached to hard domains and, therefore, under constraint from hard domains. And the α relaxation represents the relatively high–frequency relaxation process without direct limitation from hard phase. The thickness of this intermediate region surrounding glassy hard domain was estimated as 0.4 to 0.5 nm [105]. In this work, we define the marginally soft region constrained by hard domain as core–shell region and characterize this region as soft atoms within N nearest neighbors to hard segments, where $N = 5$ for the characterization in atomistic model.

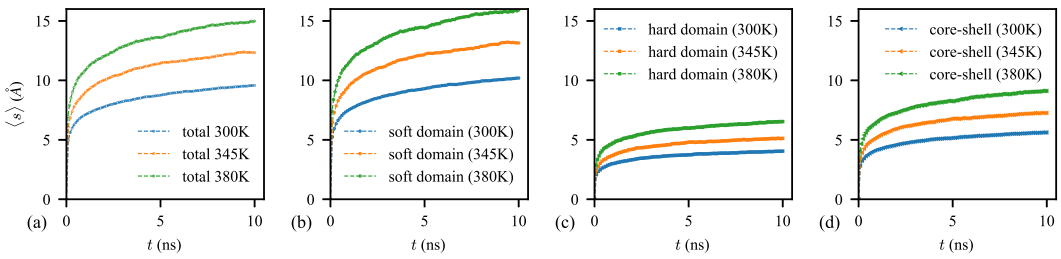

Figure 4.12: Average magnitude of slip vectors from atomistic relaxation.

Figure 4.12 shows the magnitude of slip vectors $\langle s_i \rangle = \langle |\mathbf{s}_i| \rangle$ averaged over the total system, soft domain, hard domain and core–shell domain, respectively, during atomistic relaxation simulations at various temperatures. Since the trending change of the slip vector after 10 ns during relaxation simulation can be extrapolated, we only show the first 10 ns here. For all three temperature conditions, the three phases are displaying distinct behaviors regarding relative slipping. The atoms in soft domains slip with highest speed, whereas the atoms in hard domain move significantly slower in the first 2 ns of relaxation simulation. And the total average slip among all atoms is dominated by soft atoms due to large population of atoms in soft domains. As expected, the mobility of atoms in core–shell layer stands in the intermediate level between hard and soft atoms. And after that, the soft atoms continue moving further from their original locations with fairly amount of speed. By contrast, the increments of relative sliding distance within hard atoms and core–shell atoms are consistently negligible. The speed of local slipping of three phases starts with large values and gradually decrease. Within the time range of relaxation simulation, soft atoms maintains the highest speed among all phase definitions. At the beginning of simulation, the atoms in the core–shell layer slide faster than the atoms in the hard phase, whereas the slipping speed of core–shell region decreases to the slowest case after approximately 2 ns. And with increased temperatures, the average magnitudes

of slip vectors of all sub–domains increase with faster speed indicating higher mobility, i.e., faster local dynamics, due to higher kinetic energy. It is worth noting that the magnitude of slip vector magnitude almost equally increases as increased temperature from 300 to 345 K and from 345 to 380 K, while the increment between 345 and 380 K is larger than the one between 300 and 345 K.

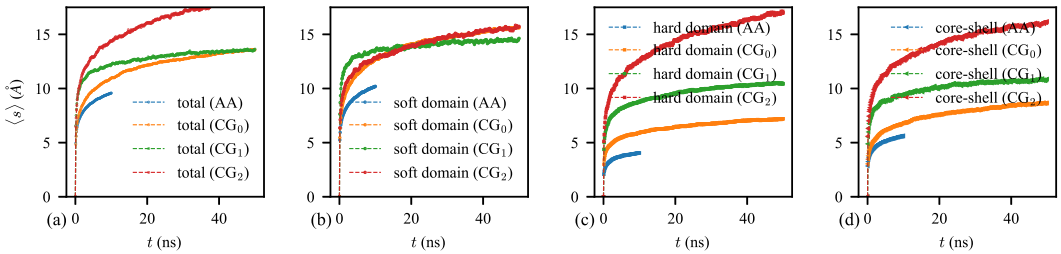

Figure 4.13: Average magnitude of slip vectors in hard, soft and core–shell domain from multiresolution simulations.

The slip vector is also calculated for coarse–grained models, which is shown in Figure 4.13. The atoms in core–shell layer are defined as 4, 3 and 2 nearest neighbors to hard segments for CG_0, CG_1 and CG_2, respectively, to follow the layer dimension as seen by experimental measurements in [105]. It is clear to observe that the slipping magnitudes among coarse–grained models are significantly higher than the one of atomistic model. However, the increment between coarse–grained models does not follow the degree of coarse–graining. For CG_0 and CG_1, the behaviors of relative slipping within each sub–domain is qualitatively similar to atomistic model. However, in CG_2 model, the average slipping of super–atoms in soft domains is greatly less than the one of hard domains suggesting higher mobility of hard super–atoms.

4.4 Summary

In this chapter, we firstly developed an intermediate coarse–grained model to bridge the scales between the united–atom–like model and the reactive model of polyurea described in Chapter 2 and Chapter 3. With the coarse–grained models in various resolutions, we are able to investigate the dynamic characteristics of polyurea in different time scales. In addition, an incremental reverse–mapping framework has been proposed to reconstruct the morphology and crosslinking of amorphous polymeric system established from polymerization simulations in atomistic resolution.

The MSD of the center of mass of segment reveals the acceleration of coarse–graining dynamics compared with atomistic model and the difference of dynamic behaviors between hard and soft phases. The relaxation times at different temperatures derived from correlation of soft–segment end–to–end vectors agree well with experimental result. And slip vector was calculated to investigate the local dynamics in relaxation simulations, which indicates the existence of the intermediate layer in soft phase but under constraint from hard phase. Contrast to the obviously faster dynamics of soft domains than the one of hard domains in atomistic, CG_0 and CG_1, both MSD and slip vector indicate coincident dynamic behaviors of soft and hard domains in CG_2.

Chapter 5

SUMMARY AND CONCLUSION

In this work, we have developed multi–scale coarse–grained (CG) molecular models of polyurea to investigate the connection between its heterogeneous microstructure and its mechanical properties under extreme conditions. The coarse–grained models are calibrated systematically via a structure–matching method called iterative Boltzmann inversion (IBI) to reproduce the target structural distributions sampled from atomistic molecular dynamics (MD) simulations. To accomplish these goals, we have introduced several improvements to the coarse–graining methodology to deal with the chemical complexity of polyurea compared to the relatively simple polymer systems the IBI method has previously been applied to. Taking advantage of the multiresolution coarse–grained models, we are able to study structure–property relationships across a wider range of time and length scales, than is possible with conventional MD simulations. And we also proposed a top–down backmapping workflow to efficiently and effectively reconstruct the specific morphology and crosslinking developed by long–term coarse–grained simulations at atomistic resolution.

Firstly, we have developed a high–resolution coarse–grained model of polyurea with the same coarse–graining degree of united atom models. Due to the high complexity of chemical formulation and high resolution of this model, we developed an adaptive scaling function based on pair distance to determine the optimal potential correction in IBI and simultaneously handle the heterogeneous interactions among 98 pontential functions. After comparing with the conventional approach, i.e., using a constant scaling parameter, the adaptive scaling function accelerates the speed of optimization

convergence by 3 times and effectively improves the accuracy of reproducing each individual distribution function. Additionally, we proposed a statistical convergence criterion to provide a more robust understanding of the degree to which the CG models represent the target structure.

The high–resolution model developed here accelerates the computational speed by nearly sixteenfold on a single processor, allowing simulations of polyurea to be performed at representative length scales and at time scales exceeding 50 ns. The enlarged model system and prolonged equilibrium time resconstruct the phase–segregated morphology with characteristic lengths, i.e., hard domain thickness and inter–domain spacing, that are consistent with those observed by x–ray scattering experiments. And the hard domains represent interconnected or percolated structure due to long–range connectivity among hard segments, which has also been observed by AFM measurements of polyurea. However, this long–range connectivity among hard segments displays significant interruption in a diblock polyurea system compared with a multiblock system. The distribution of end–to–end lengths of the soft segments suggests that the population of the end–to–end lengths follows a sum of two normal distributions representing the existence of loop–like and bridge–like soft segments. Characterization by p_2 order parameters among benzene rings indicates the absence of ordered hard–domain which is consistent with the amorphous hard phase in x–ray scattering measurements. Lastly, this coarse–grained model is able to quantitively provides insight to the hydrogen bonds within the hard phase regarding functional monomers.

In addition to the united–atom–like model, we have also developed a reactive coarse–grained model for polyurea elastomers, the force field of which was trained by matching the structural distributions sampled from atomistic partially–polymerized polyurea

systems. The coarse–grained polymerization simulations were performed by distance–based bonding criterion and topological change, by which we are able to construct polyurea networks with a consideration of prepolymer diffusion. To investigate the effect of polymerization rate on the microstructure of polyurea, the polymerization simulations were varied by different chemical reaction speeds leading to various morphologies, polymerization degrees, segmental and chain conformations. In addition, extra polyurea systems were generated by sampling the molecular weight distributions of polymerized polyurea and random walk equilibrium instead of polymerzation simulations. After that, to link the bonding–rate–induced structural difference with mechanical properties, we performed uniaxial compression on the different sets of model systems and probed the strain–stress relationship.

As a result, the microphase separation of polyurea was characterized by hard domain thickness and inter–domain spacing, indicating that slower reaction speed provides hard domains with larger domain thickness and inter–domain spacing. And faster reaction leads to higher polymerization degree, i.e., larger mass–average molecular weight, and higher degree of polydispersity in molecular weight. For chain conformation, the chains that polymerized at a faster rate tended to have a larger radius of gyration, and therefore, on average, form bridges across a larger number of hard domains. And with probabilistic characterization of segmental behaviors, the compressive strength of polyurea network is substantially affected by segmental connection between hard domains, i.e., relative fraction of bridge–type and loop–type soft segments. Higher fraction of bridge–type soft segments leads to higher compressive strength especially at large deformation when bridges are fully stretched between hard domains. In addition, compressive strength also shows positive dependence on chain conformation as revealed by radius of gyration and flow stress at different strains.

The positive dependence suggests that a polyurea chain comprised of similar amount of bridge connections may provide different effects on deformation mechanism, i.e., a chain connecting many hard domains attempt to make more contribution to strength than connecting same two hard domains in a back and forth regime.

Finally, we proposed a hierarchical backmapping workflow to transform the microstructure of polyurea from polymerization simulation to atomistic scale by introducing an intermediate coarse–grained model. The backmapping scheme is able to effectively and efficiently reconstruct the phase–segregated morphology and chain characteristics of polyurea in atomistic representation. In addition, with the multiresolution coarse–grained models, we are able to investigate the effect of coarse–graining degree on dynamics of molecular modeling. The acceleration of diffusion by coarse–graining was characterized by mean squared displacement of the center of mass of segment representing the heterogeneous behavior within the hard–soft phases of polyurea. The calculation of slip vector within each sub–phase suggests that the existence of a intermediate phase in soft domains but under constraint from hard domains.

REFERENCES

[1] Johannes Brandrup, Edmund H Immergut, Eric A Grulke, Akihiro Abe, and Daniel R Bloch. *Polymer handbook*, volume 7. Wiley New York etc, 1989.

[2] IM Ward and PR Pinnock. The mechanical properties of solid polymers. *British Journal of Applied Physics*, 17(1):3, 1966.

[3] Rodney J Andrews and Eric A Grulke. Glass transition temperatures of polymers. *Wiley Database of Polymer Properties*, 2003.

[4] F Bovey. *Macromolecules: an introduction to polymer science*. Elsevier, 2012.

[5] Liang Xue, Willis Mock Jr, and Ted Belytschko. Penetration of DH-36 steel plates with and without polyurea coating. *Mech. Mater.*, 42(11):981–1003, 2010.

[6] Jae-Hwang Lee, David Veysset, Jonathan P Singer, Markus Retsch, Gagan Saini, Thomas Pezeril, Keith A Nelson, and Edwin L Thomas. High strain rate deformation of layered nanocomposites. *Nat. Commun.*, 3:1164, 2012.

[7] Hansohl Cho, Susan Bartyczak, Willis Mock Jr, and Mary C Boyce. Dissipation and resilience of elastomeric segmented copolymers under extreme strain rates. *Polymer*, 54(21):5952–5964, 2013.

[8] Pauline Marlin and Georges L Chahine. Erosion and heating of polyurea under cavitating jets. *Wear*, 414:262–274, 2018.

[9] BJ Ramirez and V Gupta. Evaluation of novel temperature-stable viscoelastic polyurea foams as helmet liner materials. *Materials & Design*, 137:298–304, 2018.

[10] CM Roland, D Fragiadakis, and RM Gamache. Elastomer–steel laminate armor. *Composite Structures*, 92(5):1059–1064, 2010.

[11] Alicia M Castagna, Autchara Pangon, Taeyi Choi, Gregory P Dillon, and James Runt. The role of soft segment molecular weight on microphase separation and dynamics of bulk polymerized polyureas. *Macromolecules*, 45(20):8438–8444, 2012.

[12] Alicia M Castagna, Autchara Pangon, Gregory P Dillon, and James Runt. Effect of thermal history on the microstructure of a poly (tetramethylene oxide)-based polyurea. *Macromolecules*, 46(16):6520–6527, 2013.

[13] D Fragiadakis, R Gamache, RB Bogoslovov, and CM Roland. Segmental dynamics of polyurea: effect of stoichiometry. *Polymer*, 51(1):178–184, 2010.

[14] Autchara Pangon, Gregory P Dillon, and James Runt. Influence of mixed soft segments on microphase separation of polyurea elastomers. *Polymer*, 55(7):1837–1844, 2014.

[15] Yong He, Xinya Zhang, and James Runt. The role of diisocyanate structure on microphase separation of solution polymerized polyureas. *Polymer*, 55(3):906–913, 2014.

[16] Sudipto Das, Iskender Yilgor, Emel Yilgor, and Garth L Wilkes. Probing the urea hard domain connectivity in segmented, non-chain extended polyureas using hydrogen-bond screening agents. *Polymer*, 49(1):174–179, 2008.

[17] R Bonart and EH Müller. Phase separation in urethane elastomers as judged by low-angle x-ray scattering. i. fundamentals. *Journal of Macromolecular Science, Part B: Physics*, 10(1):177–189, 1974.

[18] JT Garrett, JS Lin, and J Runt. Influence of preparation conditions on microdomain formation in poly (urethane urea) block copolymers. *Macromolecules*, 35(1):161–168, 2002.

[19] Yong He, Delong Xie, and Xinya Zhang. The structure, microphase-separated morphology, and property of polyurethanes and polyureas. *J. Mater. Sci.*, 49(21):7339–7352, 2014.

[20] Sudipto Das, David F Cox, Garth L Wilkes, Derek B Klinedinst, Iskender Yilgor, Emel Yilgor, and Frederick L Beyer. Effect of symmetry and H-bond strength of hard segments on the structure-property relationships of segmented, nonchain extended polyurethanes and polyureas. *J. Macromol. Sci. Part B Phys.*, 46(5):853–875, 2007.

[21] CM Roland, JN Twigg, Y Vu, and PH Mott. High strain rate mechanical behavior of polyurea. *Polymer*, 48(2):574–578, 2007.

[22] Sai S Sarva, Stephanie Deschanel, Mary C Boyce, and Weinong Chen. Stress–strain behavior of a polyurea and a polyurethane from low to high strain rates. *Polymer*, 48(8):2208–2213, 2007.

[23] J Yi, MC Boyce, GF Lee, and E Balizer. Large deformation rate-dependent stress–strain behavior of polyurea and polyurethanes. *Polymer*, 47(1):319–329, 2006.

[24] CM Roland and R Casalini. Effect of hydrostatic pressure on the viscoelastic response of polyurea. *Polymer*, 48(19):5747–5752, 2007.

[25] SN Raman, T Ngo, J Lu, and P Mendis. Experimental investigation on the tensile behavior of polyurea at high strain rates. *Materials & Design*, 50:124–129, 2013.

[26] JA Pathak, JN Twigg, KE Nugent, DL Ho, EK Lin, PH Mott, CG Robertson, MK Vukmir, TH Epps Iii, and CM Roland. Structure evolution in a polyurea segmented block copolymer because of mechanical deformation. *Macromolecules*, 41(20):7543–7548, 2008.

[27] RG Rinaldi, MC Boyce, SJ Weigand, DJ Londono, and MW Guise. Microstructure evolution during tensile loading histories of a polyurea. *J. Polym. Sci. Part B Polym. Phys.*, 49(23):1660–1671, 2011.

[28] FR Svingala, MJ Hargather, and GS Settles. Optical techniques for measuring the shock hugoniot using ballistic projectile and high-explosive shock initiation. *International journal of impact engineering*, 50:76–82, 2012.

[29] George Youssef and Vijay Gupta. Dynamic tensile strength of polyurea. *Journal of Materials Research*, 27(2):494, 2012.

[30] George Youssef and Vijay Gupta. Dynamic response of polyurea subjected to nanosecond rise-time stress waves. *Mechanics of Time-Dependent Materials*, 16(3):317–328, 2012.

[31] Tong Jiao and Rodney Clifton. Measurement of the response of an elastomer at pressures up to 9 gpa and strain rates of 105-106s-1. In *APS Shock Compression of Condensed Matter Meeting Abstracts*, 2013.

[32] T Jiao and Rodney J Clifton. Experimental and computational investigation of the response of an elastomer at pressures up to 18 gpa and strain rates of 105- 106 s- 1. In *AIP Conference Proceedings*, volume 1793, page 140008. AIP Publishing, 2017.

[33] Hui Guo, Weiguo Guo, Alireza V Amirkhizi, Ruilu Zou, and Kangbo Yuan. Experimental investigation and modeling of mechanical behaviors of polyurea over wide ranges of strain rates and temperatures. *Polymer Testing*, 53:234–244, 2016.

[34] Florian Müller-Plathe. Coarse-graining in polymer simulation: from the atomistic to the mesoscopic scale and back. *ChemPhysChem*, 3(9):754–769, 2002.

[35] Ali Gooneie, Stephan Schuschnigg, and Clemens Holzer. A review of multiscale computational methods in polymeric materials. *Polymer*, 9(1):16, 2017.

[36] Bedri Arman, A Srinivas Reddy, and Gaurav Arya. Viscoelastic properties and shock response of coarse-grained models of multiblock versus diblock copolymers: insights into dissipative properties of polyurea. *Macromolecules*, 45(7):3247–3255, 2012.

[37] Zhiwei Cui and L Catherine Brinson. Thermomechanical properties and deformation of coarse-grained models of hard-soft block copolymers. *Phys. Rev. E*, 88(2):022602, 2013.

[38] Min Zhang, Zhiwei Cui, and Lynda Catherine Brinson. Mechanical properties of hard–soft block copolymers calculated from coarse-grained molecular dynamics models. *Journal of Polymer Science Part B: Polymer Physics*, 56(23):1552–1566, 2018.

[39] Vipin Agrawal, Gaurav Arya, and Jay Oswald. Simultaneous iterative Boltzmann inversion for coarse-graining of polyurea. *Macromolecules*, 47(10):3378–3389, 2014.

[40] Vipin Agrawal, Kristin Holzworth, Wiroj Nantasetphong, Alireza V Amirkhizi, Jay Oswald, and Sia Nemat-Nasser. Prediction of viscoelastic properties with coarse-grained molecular dynamics and experimental validation for a benchmark polyurea system. *J. Polym. Sci. Part B Polym. Phys.*, 54(8):797–810, 2016.

[41] Minghao Liu and Jay Oswald. Coarse–grained molecular modeling of the microphase structure of polyurea elastomer. *Polymer*, 176:1–10, 2019.

[42] Ali Makke, Olivier Lame, Michel Perez, and Jean-Louis Barrat. Influence of tie and loop molecules on the mechanical properties of lamellar block copolymers. *Macromolecules*, 45(20):8445–8452, 2012.

[43] Shuze Zhu, Nikolaos Lempesis, Pieter J in 't Veld, and Gregory C Rutledge. Molecular simulation of thermoplastic polyurethanes under large tensile deformation. *Macromolecules*, 51(5):1850–1864, 2018.

[44] K Michael Salerno, Anupriya Agrawal, Dvora Perahia, and Gary S Grest. Resolving dynamic properties of polymers through coarse-grained computational studies. *Phys. Rev. Lett.*, 116(5):058302, 2016.

[45] Brandon L Peters, K Michael Salerno, Anupriya Agrawal, Dvora Perahia, and Gary S Grest. Coarse-grained modeling of polyethylene melts: Effect on dynamics. *J. Chem. Theory Comput.*, 13(6):2890–2896, 2017.

[46] W Tschöp, Kurt Kremer, J Batoulis, Ta Bürger, and O Hahn. Simulation of polymer melts. i. coarse-graining procedure for polycarbonates. *Acta Polym.*, 49(2-3):61–74, 1998.

[47] S Heyden, M Ortiz, and A Fortunelli. All-atom molecular dynamics simulations of multiphase segregated polyurea under quasistatic, adiabatic, uniaxial compression. *Polymer*, 106:100–108, 2016.

[48] Ting Li, Cheng Zhang, Zhining Xie, Jun Xu, and Bao-Hua Guo. A multi-scale investigation on effects of hydrogen bonding on micro-structure and macro-properties in a polyurea. *Polymer*, 145:261–271, 2018.

[49] Selim Sami, Erol Yildirim, Mine Yurtsever, Ersin Yurtsever, Emel Yilgor, Iskender Yilgor, and Garth L Wilkes. Understanding the influence of hydrogen bonding and diisocyanate symmetry on the morphology and properties of segmented polyurethanes and polyureas: computational and experimental study. *Polymer*, 55(18):4563–4576, 2014.

[50] You-Chi Mason Wu, Weiguo Hu, Yuchen Sun, David Veysset, Steven E Kooi, Keith A Nelson, Timothy M Swager, and Alex J Hsieh. Unraveling the high strain-rate dynamic stiffening in select model polyurethanes–the role of intermolecular hydrogen bonding. *Polymer*, 168:218–227, 2019.

[51] Roland Faller and Dirk Reith. Properties of poly (isoprene): model building in the melt and in solution. *Macromolecules*, 36(14):5406–5414, 2003.

[52] Dirk Reith, Mathias Pütz, and Florian Müller-Plathe. Deriving effective mesoscale potentials from atomistic simulations. *J. Comput. Chem.*, 24(13):1624–1636, 2003.

[53] Qi Sun and Roland Faller. Systematic coarse-graining of a polymer blend: Polyisoprene and polystyrene. *J. Chem. Theory Comput.*, 2(3):607–615, 2006.

[54] Qi Sun and Roland Faller. Phase separation in polyisoprene/polystyrene blends by a systematically coarse-grained model. *J. Compu. Phys.*, 126(14):144908, 2007.

[55] Beste Bayramoglu and Roland Faller. Coarse-grained modeling of polystyrene in various environments by iterative Boltzmann inversion. *Macromolecules*, 45(22):9205–9219, 2012.

[56] Beste Bayramoglu and Roland Faller. Modeling of polystyrene under confinement: Exploring the limits of iterative Boltzmann inversion. *Macromolecules*, 46(19):7957–7976, 2013.

[57] Erol Yildirim and Mine Yurtsever. The role of diisocyanate and soft segment on the intersegmental interactions in urethane and urea based segmented copolymers: a DFT study. *Comput. Theor. Chem.*, 1035:28–38, 2014.

[58] Qing Zhou, Li Cao, Qing Li, Yalin Yao, Zhaofei Ouyang, Zhiqiang Su, and Xiaonong Chen. Investigation of the curing process of spray polyurea elastomer by FTIR, DSC, and DMA. *J. Appl. Polym. Sci.*, 125(5):3695–3701, 2012.

[59] Steve Plimpton. Fast parallel algorithms for short-range molecular dynamics. *J. Compu. Phys.*, 117(1):1–19, 1995.

[60] Michael J McQuaid, Huai Sun, and David Rigby. Development and validation of COMPASS force field parameters for molecules with aliphatic azide chains. *jcc*, 25(1):61–71, 2004.

[61] Huai Sun. COMPASS: an ab initio force-field optimized for condensed-phase applications overview with details on alkane and benzene compounds. *J. Phys. Chem. B*, 102(38):7338–7364, 1998.

[62] Mica Grujicic, B Pandurangan, AE King, J Runt, J Tarter, and G Dillon. Multi-length scale modeling and analysis of microstructure evolution and mechanical properties in polyurea. *J. Mater. Sci.*, 46(6):1767–1779, 2011.

[63] Roland Faller. Automatic coarse graining of polymers. *Polymer*, 45(11):3869–3876, 2004.

[64] Han Wang, Christoph Junghans, and Kurt Kremer. Comparative atomistic and coarse-grained study of water: What do we lose by coarse-graining? *Eur. Phys. Chem. J. E*, 28(2):221–229, 2009.

[65] Minghao Liu and Jay Oswald. cg-polyurea-uam: v1.0, March 2019.

[66] D Carolan, HM Chong, A Ivankovic, AJ Kinloch, and AC Taylor. Co-continuous polymer systems: A numerical investigation. *Comp. Mater. Sci.*, 98:24–33, 2015.

[67] D Tyagi, JL Hedrick, DC Webster, JE McGrath, and GL Wilkes. Structure–property relationships in perfectly alternating segmented polysulphone/poly (dimethylsiloxane) copolymers. *Polymer*, 29(5):833–844, 1988.

[68] Timothy C Moore, Christopher R Iacovella, and Clare McCabe. Derivation of coarse-grained potentials via multistate iterative Boltzmann inversion. *J. Chem. Phys.*, 140(22):06B606_1, 2014.

[69] Yiyong Mai and Adi Eisenberg. Self-assembly of block copolymers. *Chem. Soc. Rev.*, 41(18):5969–5985, 2012.

[70] Sudipto Das, Iskender Yilgor, Emel Yilgor, Bora Inci, Ozgul Tezgel, Frederick L Beyer, and Garth L Wilkes. Structure–property relationships and melt rheology of segmented, non-chain extended polyureas: effect of soft segment molecular weight. *Polymer*, 48(1):290–301, 2007.

[71] Peng Yi, C Rebecca Locker, and Gregory C Rutledge. Molecular dynamics simulation of homogeneous crystal nucleation in polyethylene. *Macromolecules*, 46(11):4723–4733, 2013.

[72] Yiyang Li, Vipin Agrawal, and Jay Oswald. Systematic coarse-graining of semicrystalline polyethylene. *J. Polym. Sci. Part B Polym. Phys.*, 57(6):331–342, 2019.

[73] E Yildirim, M Yurtsever, GL Wilkes, and I Yilgör. Effect of intersegmental interactions on the morphology of segmented polyurethanes with mixed soft segments: A coarse-grained simulation study. *Polymer*, 90:204–214, 2016.

[74] HN Ng, AE Allegrezza, RW Seymour, and Stuart L Cooper. Effect of segment size and polydispersity on the properties of polyurethane block polymers. *Polymer*, 14(6):255–261, 1973.

[75] Nathaniel A Lynd and Marc A Hillmyer. Influence of polydispersity on the self-assembly of diblock copolymers. *Macromolecules*, 38(21):8803–8810, 2005.

[76] Joan M Widin, Adam K Schmitt, Andrew L Schmitt, Kyuhyun Im, and Mahesh K Mahanthappa. Unexpected consequences of block polydispersity on the self-assembly of aba triblock copolymers. *Journal of the American Chemical Society*, 134(8):3834–3844, 2012.

[77] Michael Langeloth, Taisuke Sugii, Michael C Böhm, and Florian Müller-Plathe. The glass transition in cured epoxy thermosets: A comparative molecular dynamics study in coarse-grained and atomistic resolution. *J. Chem. Phys.*, 143(24):243158, 2015.

[78] Karim Farah, Michael Langeloth, Michael C Böhm, and Florian Müller-Plathe. Surface-induced interphases during curing processes between bi-and pentafunctional components: reactive coarse-grained molecular dynamics simulations. *The Journal of Adhesion*, 88(11-12):903–923, 2012.

[79] Hong Liu, Min Li, Zhong-Yuan Lu, Zuo-Guang Zhang, Chia-Chung Sun, and Tian Cui. Multiscale simulation study on the curing reaction and the network structure in a typical epoxy system. *Macromolecules*, 44(21):8650–8660, 2011.

[80] Amin Aramoon, Timothy D Breitzman, Christopher Woodward, and Jaafar A El-Awady. Coarse-grained molecular dynamics study of the curing and properties of highly cross-linked epoxy polymers. *J. Phys. Chem. B*, 120(35):9495–9505, 2016.

[81] Lauren J Abbott, Kyle E Hart, and Coray M Colina. Polymatic: a generalized simulated polymerization algorithm for amorphous polymers. *Theoretical Chemistry Accounts*, 132(3):1334, 2013.

[82] Jacob R Gissinger, Benjamin D Jensen, and Kristopher E Wise. Modeling chemical reactions in classical molecular dynamics simulations. *Polymer*, 128:211–217, 2017.

[83] S. Plimpton, P. Crozier, and A. Thompson. Lammps-large-scale atomic/molecular massively parallel simulator. *Sandia National Laboratories*, 01 2007.

[84] Y Chen, JYH Chia, ZC Su, TE Tay, and VBC Tan. Molecular modeling of epoxide-amine systems: Topological cure conversion limit and its influence on material properties. *Polymer*, 55(23):6124–6131, 2014.

[85] Ananyo Bandyopadhyay, Pavan K Valavala, Thomas C Clancy, Kristopher E Wise, and Gregory M Odegard. Molecular modeling of crosslinked epoxy polymers: The effect of crosslink density on thermomechanical properties. *Polymer*, 52(11):2445–2452, 2011.

[86] Nipun J Soni, Po-Han Lin, and Rajesh Khare. Effect of cross-linker length on the thermal and volumetric properties of cross-linked epoxy networks: A molecular simulation study. *Polymer*, 53(4):1015–1019, 2012.

[87] WG Noid, Jhih-Wei Chu, Gary S Ayton, Vinod Krishna, Sergei Izvekov, Gregory A Voth, Avisek Das, and Hans C Andersen. The multiscale coarse-graining method. i. a rigorous bridge between atomistic and coarse-grained models. *J. Chem. Phys.*, 128(24):244114, 2008.

[88] Aidan P Thompson, Steven J Plimpton, and William Mattson. General formulation of pressure and stress tensor for arbitrary many-body interaction potentials under periodic boundary conditions. *J. Chem. Phys.*, 131(15):154107, 2009.

[89] H. E. Yong, Xinya Zhang, and James. The role of diisocyanate structure on microphase separation of solution polymerized polyureas. *Polymer*, 55(3):906–913, 2014.

[90] David D Hsu, Wenjie Xia, Steven G Arturo, and Sinan Keten. Thermomechanically consistent and temperature transferable coarse-graining of atactic polystyrene. *Macromolecules*, 48(9):3057–3068, 2015.

[91] Chaofu Wu. A combined scheme for systematically coarse-graining of stereoregular polymer blends. *Macromolecules*, 46(14):5751–5761, 2013.

[92] Wujie Wang and Rafael Gómez-Bombarelli. Coarse-graining auto-encoders for molecular dynamics. *npj Computational Materials*, 5(1):1–9, 2019.

[93] Kévin Kempfer, Julien Devemy, Alain Dequidt, Marc Couty, and Patrice Malfreyt. Development of coarse-grained models for polymers by trajectory matching. *ACS omega*, 4(3):5955–5967, 2019.

[94] Zhiheng Li, Geemi P Wellawatte, Maghesree Chakraborty, Heta A Gandhi, Chenliang Xu, and Andrew D White. Graph neural network based coarse-grained mapping prediction. *Chemical Science*, 2020.

[95] Wenjie Xia, Nitin K Hansoge, Wen-Sheng Xu, Frederick R Phelan, Sinan Keten, and Jack F Douglas. Energy renormalization for coarse-graining polymers having different segmental structures. *Science advances*, 5(4):eaav4683, 2019.

[96] Melissa K Meinel and Florian üller Plathe. Loss of molecular roughness upon coarse-graining predicts the artificially accelerated mobility of coarse-grained molecular simulation models. *Journal of Chemical Theory and Computation*, 16(3):1411–1419, 2020.

[97] JA Zimmerman, CL Kelchner, PA Klein, JC Hamilton, and SM Foiles. Surface step effects on nanoindentation. *Physical Review Letters*, 87(16):165507, 2001.

[98] B Arman, Q An, SN Luo, TG Desai, DL Tonks, T Çağın, and WA Goddard Iii. Dynamic response of phenolic resin and its carbon-nanotube composites to shock wave loading. *Journal of Applied Physics*, 109(1):013503, 2011.

[99] B Arman, C Brandl, SN Luo, TC Germann, A Misra, and T Çağin. Plasticity in cu (111)/cu46zr54 glass nanolaminates under uniaxial compression. *Journal of Applied Physics*, 110(4):043539, 2011.

[100] Kurt Kremer and Gary S Grest. Dynamics of entangled linear polymer melts: A molecular-dynamics simulation. *The Journal of Chemical Physics*, 92(8):5057–5086, 1990.

[101] Daniel Fragiadakis and James Runt. Molecular dynamics of segmented polyurethane copolymers: influence of soft segment composition. *Macromolecules*, 46(10):4184–4190, 2013.

[102] Gordon S Fulcher. Analysis of recent measurements of the viscosity of glasses. *Journal of the American Ceramic Society*, 8(6):339–355, 1925.

[103] M Cyrot. A possible origin for the vogel-fulcher law. *Physics Letters A*, 83(6):275–278, 1981.

[104] João F Mano and Eduardo Pereira. Data analysis with the vogel- fulcher-tammann- hesse equation. *The Journal of Physical Chemistry A*, 108(49):10824–10833, 2004.

[105] Nerea Sebastián, Christophe Contal, Antoni Sánchez-Ferrer, and Marco Pieruccini. Interplay between structure and relaxation in polyurea networks: the point of view from a novel method of cooperativity analysis of dielectric response. *Soft matter*, 14(38):7839–7849, 2018.

[106] Marius Reinecker, Armin Fuith, Viktor Soprunyuk, Antoni Sánchez-Ferrer, Aleš Mrzel, Renato Torre, and Wilfried Schranz. Influence of inorganic nanoparticles on the glass transitions of polyurea elastomers. *physica status solidi (a)*, 210(11):2320–2327, 2013.